UNIVERSIDADE FEDERAL DE UBERLÂNDIA

ALEXANDRE FELIPE MEDINA CORRÊA

High-speed train aerodynamics under crosswinds: from standard wind tunnel testing to the effect of the train cooling systems

Uberlândia – MG – Brasil

10 de Novembro de 2017

ALEXANDRE FELIPE MEDINA CORRÊA

High-speed train aerodynamics under crosswinds: from standard wind tunnel testing to the effect of the train cooling systems

Dissertação apresentada ao Programa de Pós-Graduação em Engenharia Mecânica da Universidade Federal de Uberlândia, como parte dos requisitos para a obtenção do título de **MESTRE EM ENGENHARIA MECÂNICA**.

Área de concentração: Transferência de Calor e Mecânica dos Fluidos

Universidade Federal de Uberlândia – UFU

Faculdade de Engenharia Mecânica

Programa de Pós-Graduação em Engenharia Mecânica

Supervisor: Prof. Dr. Francisco José de Souza

Co-supervisor: Dr. Steve Cochard

Uberlândia – MG – Brasil

10 de Novembro de 2017

Dados Internacionais de Catalogação na Publicação (CIP)
Sistema de Bibliotecas da UFU, MG, Brasil.

C823h
2017

Corrêa, Alexandre Felipe Medina, 1992-
High-speed train aerodynamics under crosswinds: from standard wind tunnel testing to the effect of the train cooling systems / Alexandre Felipe Medina Corrêa. - 2017.
76 f. : il.

Orientador: Francisco José de Souza.
Dissertação (mestrado) - Universidade Federal de Uberlândia, Programa de Pós-Graduação em Engenharia Mecânica.
Disponível em: http://dx.doi.org/10.14393/ufu.di.2018.22
Inclui bibliografia.

1. Engenharia mecânica - Teses. 2. Aerodinâmica - Teses. 3. Fluidodinâmica computacional - Teses. I. Souza, Francisco José de. II. Universidade Federal de Uberlândia. Programa de Pós-Graduação em Engenharia Mecânica. III. Título.

CDU: 621

SERVIÇO PÚBLICO FEDERAL
MINISTÉRIO DA EDUCAÇÃO
UNIVERSIDADE FEDERAL DE UBERLÂNDIA
FACULDADE DE ENGENHARIA MECÂNICA
PROGRAMA DE PÓS-GRADUAÇÃO EM ENGENHARIA MECÂNICA

ALUNO: Alexandre Felipe Medina Corrêa

NÚMERO DE MATRÍCULA: 11622EMC003

ÁREA DE CONCENTRAÇÃO: Transferência de Calor e Mecânica dos Fluidos

LINHA DE PESQUISA: Dinâmica dos Fluidos e Transferência de Calor

PÓS-GRADUAÇÃO EM ENGENHARIA MECÂNICA: NÍVEL MESTRADO

TÍTULO DA DISSERTAÇÃO:

"High-speed Trains Aerodynamics under Crosswind Conditions: The Effect of the Train Cooling Systems"

ORIENTADOR: Prof. Dr. Francisco José de Souza

A Dissertação foi **APROVADA** em reunião pública, realizada no Anfiteatro do MFLab do Bloco 5P, Campus Santa Mônica, em 10 de novembro de 2017, às 13:00 horas, com a seguinte Banca Examinadora:

NOME	**ASSINATURA**
Prof. Dr. Francisco José de Souza	UFU ____________
Prof. Dr. Leonardo Sanches	UFU ____________
Prof. Dr. André Valdetaro Gomes Cavalieri	ITA ____________

Uberlândia, 10 de novembro de 2017

Universidade Federal de Uberlândia – Av. João Naves de Ávila, n° 2121, Bloco 1M, Bairro Santa Mônica - 38.408-144 - Uberlândia – MG +55 – 34 – 3239-4282 secposmec@mecanica.ufu.br http://www.posgrad.mecanica.ufu.br

To my family for their unconditional love and support.

Acknowledgements

I would like to express my gratitude to Dr. Francisco José de Souza and Dr. Steve Cochard, without their motivation and encouragement I would not have considered to endeavor myself in studying fluid mechanics and aerodynamics. It was under their tutelage that I developed focus and became interested in Computational Fluid Dynamics.

Special thanks go to Dr. Alois Starlinger for receiving me at Stadler Altenrhein AG (STADLER[1]). To CD-adapco (CD-ADAPCO[2]), thanks to Ms. Lisa Graichen for providing me with the academic license for STAR-CCM+ and to Henric Barthelme for all the support. My research would not have been possible without the support from Stadler and CD-adapco.

I would like to thank my parents, Yolanda and Eduardo for all the support and encouragement to pursue my dreams and to learn more. Last, but not least, I thank my fiancée and best friend, Aline, for her love, encouragement and patience.

---

[1] STADLER <http://www.stadlerrail.com/>

[2] CD-ADAPCO <http://www.cd-adapco.com/>

STADLER

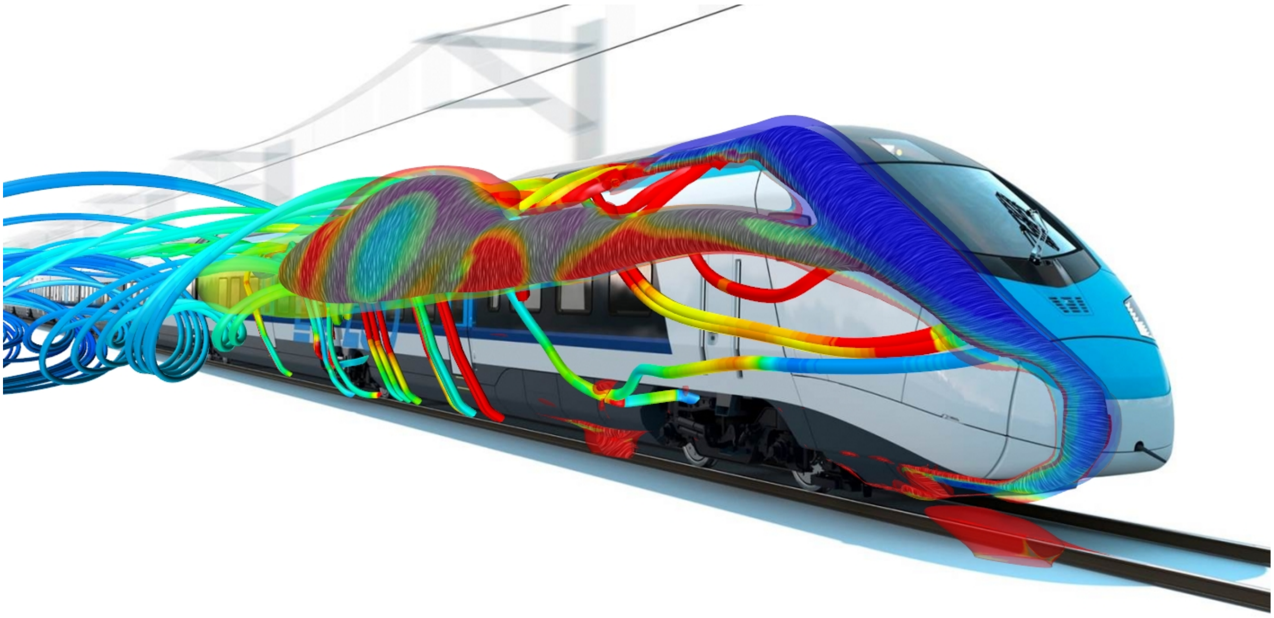

”The most exciting phrase to hear in science,
the one that heralds new discoveries,
is not "Eureka" but "That’s funny..."”

Isaac Asimov - (1920 - 1992)

Abstract

Crosswind occurs as a train travels in windy conditions. The wind, combined with the train velocity, generates a relative wind that loads the train. This aerodynamic load can be strong enough to flip the train on its side.

Standard wind tunnel testing does not represent the flow conditions observed at high-speed as the Reynolds number ($\sim 10^5$) are smaller compared to full-scale ($\sim 10^7$) and the static-models do not reproduce the relative ground motion or account for the air flow of the train cooling equipments. Computational Fluid Dynamics (CFD) simulations were performed to address these issues and the results are compared to the experimental data for Stadler EC250 high-speed train.

It was found that the wind tunnel walls affect the far wake, curving it. Enlarging the wind tunnel avoids this issue but without affecting the near wake, producing the same forces and moments. The standard Single Track Ballast and Rail (STBR) generates a tip vortex that affects the lee-side wake, increasing the lift coefficient by 5% compared to an infinite STBR (at $\beta = 45°$) for reduced-scale static models. The modeling of the vehicle motion with a moving reference frame produced a large difference in side force and lift coefficients (+5% and +7%) compared to the static model with infinite STBR, but the lee-rail moment only increased by 3%. To evaluate the effects of the Reynolds number the moving model was simulated in full-scale. It was found that the lift coefficient increased by 15% and the side force coefficient decreased by 10%, producing a lee-rail moment 5% lower than observed for the reduced-scale moving model. Finally, the effects of the air intakes and exhausts for the full-scale train were analyzed. Compared to the reduced-scale static model the lift and side force coefficients were different, where the first had an average of −25% and the second +4%, resulting in a lee-rail moment coefficient ∼ 3% lower.

The analysis of crosswind stability presented similar lee-rail moment coefficient $C^*_{M_x,\mathrm{lee}}$ between the reduced-scale static model and full-scale train with its ventilation systems. This shows that the static wind tunnel tests are reliable on the assessment of high-speed trains crosswind stability.

Key-words: Crosswind stability, Overturning, Train aerodynamics, Wind tunnel, Cooling systems, Computational fluids dynamics.

Resumo

Ventos laterais, ou cruzados, ocorrem à medida que um trem viaja em campos abertos. O vento, combinado com a velocidade do trem, provoca um vento relativo causador de esforços o trem. Esse carregamento aerodinâmico pode ser forte o suficiente para tomar o veículo.

Testes em túneis-de-vento não representam as condições do escoamento observadas em altas velocidades em sua totalidade, já que seu número de Reynolds ($\sim 10^5$) é pequeno comparado à escala real ($\sim 10^7$). Além disso, modelos estáticos não modelam o movimento relativo entre o trem e o solo assim como não contabilizam o ar proveniente do equipamento de controle térmico e conforto do trem. A Dinâmica dos Fluidos Computacional (CFD, sigla em inglês) foi aplicada para abordar estas questões e os resultados obtidos são comparados com dados experimentos do trem-de-alta-velocidade Stadler EC250.

Foi observado que as paredes do túnel-de-vento afetam a escoamento, curvando a esteira gerada pelo trem. Esse problema foi resolvido aumentando a largura do túnel-de-vento, porém observa-se que o escoamento próximo ao trem não é afetado, produzindo os mesmos carregamentos aerodinâmicos. A configuração de solo padrão STBR gera um vórtice em sua extremidade que afeta a esteira a sotavento do trem, aumenta o coeficiente de sustentação em 5% comparado a um STBR infinitamente longo (para $\beta = 45°$) em modelos estáticos em escala reduzida. A modelagem do movimento do veículo em escala reduzida afeta os coeficientes de força lateral e sustentação (+5% e +7%) comparados ao STBR infinitamente longo, afetando o coeficiente de momento sobre o trilho a sotavento em 3%. Para avaliar a influência do número de Reynolds, o trem foi simulada em escala real. Com isso a sustentação aumenta em 15% e a força lateral reduz em 10%, o que leva a um coeficiente de momento sobre o trilho a sotavento 5% menor. Finalmente, os efeitos do o ar proveniente do equipamento de controle térmico e conforto do trem foi avaliado. Comparados aos resultados do modelo estático em escala reduzida a sustentação foi reduzida em 25% e a força lateral aumentada em 4%, resultando em um coeficiente de momento sobre o trilho a sotavento 3% menor.

A análise da estabilidade em ventos cruzados mostrou semelhanças entre o modelo estático em escala reduzida e o trem em escala real com os sistemas térmicos. Isso mostra que experimentos em escala reduzida são confiáveis para análise da estabilidade de trens-de-alta-velocidade em situações de vento cruzado.

Palavras-chaves: Estabilidade em ventos laterais, Capotamento, Aerodinâmica de trens, Túnel-de-vento, Sistemas de Arrefecimento, Dinâmica dos fluidos computacional.

List of Figures

List of Tables

List of abbreviations and acronyms

ABL	Atmospheric Boundary Layer
BART	Bay Area Rapid Transit
CD-adapco	Computational Dynamic-Analysis & Design Application Company
CFD	Computational Fluid Dynamics
CPU	Central Processing Unit
CWC	Characteristic Wind Curve
DDES	Delayed Detached Eddy Simulation
DLR	Deutsches Zentrum für Luft- und Raumfahrt e.V.
KKK	Cryogenic Wind tunnel Cologne
EN	European Norm
FVM	Finite Volume Method
HSL	High-speed Lines
HST	High-speed Trains
MBS	Multi-Body Simulation
MRF	Moving Reference Frame
NS	Navier-Stokes equations
RANS	Reynolds-averaged Navier–Stokes equations
Re	Reynolds Number
RSM	Reynolds Stress Transport model
SA	Spalart-Allmaras model
SST	Shear Stress Transport model
STBR	Single Track Ballast and Rail
TFG	True Flat Ground

TOR	Top-of-rail
TSI	Technical Specifications for Interoperability
UIC	Union Internationale des Chemins de fer
VC	Volume Control

List of symbols

β	Yaw angle
φ	Wind angle
V_{tr}	Train velocity
V_w	Wind velocity
V_a	Relative wind velocity
f_x	Axial force
f_y	Side force
f_z	Lift force
$C^*_{f_x}$	Axial force coefficient
$C^*_{f_y}$	Side force coefficient
$C^*_{f_z}$	Lift coefficient
M_x	Rolling moment
M_y	Pitching moment
M_z	Yawing moment
$M_{x,\mathrm{lee}}$	Leeward rail rolling moment
$C^*_{M_x}$	Rolling moment coefficient
$C^*_{M_y}$	Pitching moment coefficient
$C^*_{M_z}$	Yawing moment coefficient
$C^*_{M_{x,\mathrm{lee}}}$	Lee-rail moment coefficient
q	Dynamic pressure
A_{tr}	Train's reference cross-sectional area
l_{tr}	Train's reference length
ρ	Fluid density

μ	Fluid dynamic viscosity
x_i	Position
u_i	Velocity
$\overline{u_i}$	Average velocity
$u_i^{'}$	Fluctuating velocity
$\overline{p}$	Average pressure
H	Train height
h	Prism layer thickness
d	Cell width

Contents

1 Introduction

In the last decades the world has witnessed a significant increase on the number of high-speed lines (HSL). In 2015 there was approximately $29,792$ km of HSL in the world, with $3,602$ high-speed train (HST) sets in operation in 20 countries (UIC, 2015). Not only the range and number of lines have increased, the high-speed trains are faster. The first high-speed train in operation, the Japanese bullet train Shinkansen 0 Series, had a maximum operational speed of 200 km/h in 1964, while in 2015 the maximum speed in revenue operation was 350 km/h. The HSL are a transportation market which accommodates close to $1,600$ million passenger per year (UIC, 2015). This expressive number of passenger combined with higher operating velocities achieved by modern trains has increased the concern of rail vehicles safety facing different issues during its operation, such as its stability under crosswind conditions.

The aim of this thesis is to improve the safety of high speed trains under crosswind conditions. Computational Fluid Dynamics (CFD) simulations were used to understand the forces and moments that act on a train traveling in windy conditions. The analysis is made for the Stadler EC250 (Smile) high-speed train. This research study first validates the simulation results before looking at different parameters that influence the train safety.

This work is divided into four chapters. The first one introduces crosswind and presents some key research. The second chapter focuses on the numerical simulation setup with emphasis on the turbulence models and the computational meshes used. Chapter 3 first presents the results of the validation test, and then the influence of key parameters. Chapter 4 concludes this thesis by highlighting the findings of this research work.

1.1 History

The first train overturning caused by crosswind happened in St. Louis, United States of America, in April 1892, when a passenger train was blown from a narrow gauge track during a strong storm. In total, 29 crosswind-induced accidents have occurred since then, most of them in Japan due to the country's narrow gauge lines (Proppe & Wetzel, 2007). To enhance trains stability for crosswinds and earthquakes, the BART line (Bay Area Rapid Transit, San Francisco, USA) selected broad gauges, 17% wider than the standard ones. Wind-induced accidents have been recorded on standard gauge tracks on endangered locations, as bridges and embankments for both passenger and freight trains. The Lanzhou-Xinjiang High-Speed Railway, as example, crosses a plain desert region constantly blown by strong winds, in China. In 2007, a 11-car train was overturned by fierce gusts during a sand storm (see Figure 1 d). Figure 1 shows other recent examples of train overturning due to strong crosswinds: two light trains in Europe (Austria, 2002 and Switzerland, 2007) and a locomotive in Japan (2006).

Figure 1 – Railcar derailment due to strong side winds respectively at Uttendorf, Austria, 2002 (Peters, 2004); Miyazaki Prefecture, Japan, 2006 (The Japan Times, 2006); Wasserauen, Switzerland, 2007 (Sturmarchiv Schweiz, 2007) and Lanzhou-Xinjiang Railway, China, 2007 (Xinhua News Agency, 2007).

1.2 Crosswind

Crosswind occurs as soon as a train travels in windy conditions. The wind, combined with the train velocity, generates a relative wind that loads the train. This aerodynamic load can be strong enough to flip the train on its side. During the last decades, crosswind stability of high-speed trains has gained more attention as the number of high-speed lines has drastically increased in Europe. Overturning a high-speed train at 300 km/h would have deadly consequences. As the relative velocity between the side wind and train increases, so does the strength of aerodynamic loads, increasing the risk of an accident. In Figure 2, the definition of a train traveling under a crosswind condition is presented. The relative wind velocity V_a is the velocity between the train traveling speed V_{tr} and the wind velocity V_w. The yaw angle β is defined as the angle between the relative velocity and the train velocity and the wind angle φ between the train and wind velocities.

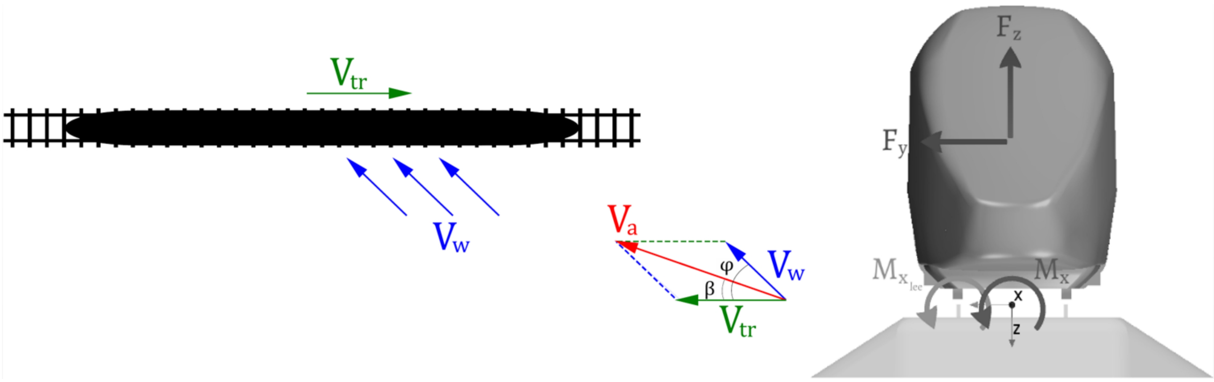

Figure 2 – Definition of the crosswind condition for traveling trains and the aerodynamics forces and moments acting uopn the train surface.

The aerodynamic load on the train is best summarized by the rolling moment on the leeward rail ($M_{x,\mathrm{lee}}$). The weight of the train counterbalances this aerodynamic moment, up to a critical wind speed. Light weight construction techniques and materials, as aluminum alloys and plastics, combined with higher velocities of modern high-speed trains increased the concern of rail vehicle stability under crosswind conditions. Also, recent changes in train propulsion affect the weight distribution of trains. Modern designs have changed from a locomotive engine to multiple engine units, with the engines located in the bogies. The multiple engine concept distributes the traction and the weight between cars improving acceleration. The leading car weight is reduced compared to previous locomotives, increasing the risk of derailment as the two leading vehicles are the most sensitive to crosswind conditions (Carrarini, 2007; Diedrichs, 2008).

1.3 The European Technical Specifications for Interoperability (TSI)

Crosswind is not the only aerodynamic related issue that high-speed trains face during operation. Rail vehicles face issues such as propagation of pressure waves inside tunnels, crossing vehicles, the induced flow during the passage of trains (known as slipstreams) and noise inside and outside vehicles. The design of modern trains must integrate different solutions to solve these issues. A general overview of studies and experiments made on these issues is given by Schetz (2001). To guaranty a safe operation on the European network all parties must follow the TSI (2008). The TSI provides requirements to ensure the interoperability of the European rail systems.

The TSI refers to the European Norms 14067 (2010) for aerodynamics, which contains the train certification specifications. The EN-14067 norm consists of six parts. The procedures necessary for trains crosswind stability certification are presented in the EN-14067 "Part 6: Requirements and test procedures for crosswind assessment". This norm applies to passenger vehicles operating up to 360 km/h and freight trains up to 160 km/h.

1.3.1 European Norm EN-14607-6

The EN-14607-6 defines that the crosswind stability of rolling stock is given by means of characteristic wind curves (CWC), where the CWC define the maximum wind speed that a train can withstand without exceeding a wheel unloading threshold. The assessment of the CWCs is done by evaluating the aerodynamic and vehicle dynamic characteristics.

The evaluation of the vehicle aerodynamic characteristics produces six aerodynamic coefficients. These coefficients serve as input to the dynamic simulations. From the dynamic behavior the windward wheel unloading is computed, and the maximum wind speed is defined. The maximum wind speed combined with the yaw angle give the CWC.

Depending on the train maximum speed, the assessment of the aerodynamic coefficients can be done by using predictive equations, Computational Fluid Dynamics (CFD) or reduced-scale static wind tunnel data. CFD and wind tunnel tests shall include test results of specified benchmark vehicles. The results of at least one of the three benchmark vehicles (ICE 3, TGV Duplex and ETR 500) have to be replicated. The determination of the vehicle dynamic behavior can be done using three different computational methods: a two-dimensional vehicle model (three-mass dynamic model), an advanced quasi-static method (five-mass dynamic model) and time-dependent Multi-Body Simulations (MBS). The norm recommends the last two dynamic methods.

The full proof for crosswind stability for passenger trains with velocities between 200 and 360 km/h shall be done by static wind tunnel tests and time-dependent multi-body simulations (MBS). Although both the characterization of the aerodynamic and dynamic behavior under side winds is important, only the aerodynamic behavior of the train was considered in this research.

1.3.2 Reduced-scale Wind tunnel Measurements

Wind tunnel tests provide the vehicle aerodynamic forces and moments coefficients, including the lee-rail moment coefficient $C^*_{M_{x,\mathrm{lee}}}$, as it is mainly this moment that unload the windward wheels and could lead to vehicle overturning. The aerodynamic forces and moments coefficients are calculated as presented in equations (1.1) and (1.2), respectively.

$$C^*_{f_i} = \frac{f_i}{q \cdot A_{tr}} \tag{1.1}$$

$$C^*_{M_i} = \frac{M_i}{q \cdot A_{tr} \cdot l_{tr}} \tag{1.2}$$

The reference cross-sectional area and length are given as $A_{tr} = 10\ m^2$ and $l_{tr} = 3$ m, respectively, in full-scale (EN-14607-6, 2010). The dynamic pressure q is given by equation (1.3), where ρ is the fluid specific mass and V_a the relative wind velocity.

$$q = \frac{\rho \cdot {V_a}^2}{2} \tag{1.3}$$

These coefficients are measured relative to a specific coordinate system according to the $EN-14607-6$. The origin of the coordinate system is located at the top-of-rail mid track position and half distance between the two first-car bogies. The x direction points to the train direction of motion, y points to the lee-ward side of the train and z vertically towards the ground, as shown in Figure 2.

The norm requires static models with low turbulence uniform inlet profile ensuring reliability and repeatability. Although static tests are a simplification of the full-scale condition, moving model tests require further research before being considered standard. The blockage ratio of the total modeled configuration (train and ground configuration) with respect to wind tunnel cross-sectional area shall be less than 15% at a yaw angle of 30°.

The full proof for crosswind stability for the Stadler EC250 was performed in the DLR Cryogenic Wind tunnel Cologne (KKK) following the EN-14607-6. The KKK is a cryogenic closed-loop subsonic wind tunnel with a test-section area of 32.34 m^2. The model and its ground configuration are mounted on a splitter plate. The splitter plate is mounted on the wind tunnel turn table and rotates with it. Once the wind tunnel has reached the desired flow velocity, the turn table is rotated from 0° to 90° to simulate different yaw angles. The following sections describe the test characteristics.

1.3.2.1 1:25 Model

The wind tunnel measurements were performed on a 1:25 scale 2 and 3-car model. The model was manufactured in aluminum alloy, achieving a modeling tolerance of 0.05%. The experimental results of the leading car of the 2-car model served as reference values in this study.

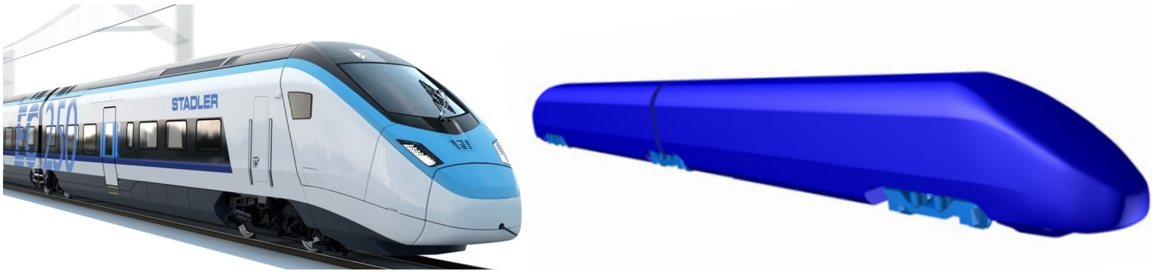

Figure 3 – The Stadler EC250 high-speed train and the geometry of the 1:25 wind tunnel 2-car model of Stadler EC250.

1.3.2.2 Wind tunnel Dimensions

Concerning the wind tunnel dimensions, the norm states that the blockage ratio of the total modeled configuration (train and ground configuration) shall be less than 15% at a yaw angle of 30°. There is no record of the influence of the wind tunnel size on the aerodynamic coefficients even if the blockage ratio is kept below 15%. This study will address the effect of increasing the wind tunnel width, which reduces the blockage ratio.

1.3.2.3 Ground Configuration

The tests were carried out on a Standard Single Track Ballast and Rail (STBR) ground simulation (see Figure 4). The distance between the model wheels and the Top-Of-Rail (TOR) is defined to 60 mm in full-scale.

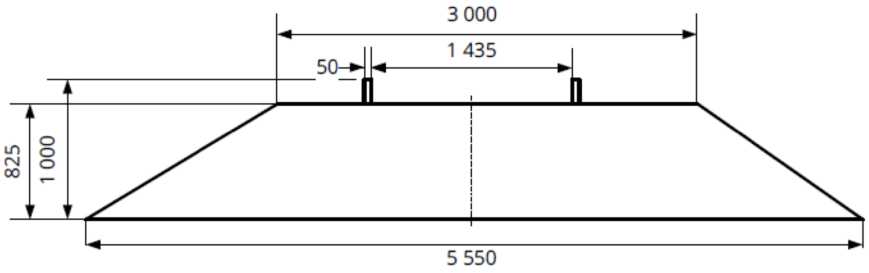

Figure 4 – Single track ballast and rail ground configuration (dimensions in full-scale).

In the KKK tests, the model and STBR were installed on a splitter plate to avoid the influence of the wind tunnel ground boundary layer, as shown in Figure 5. 20 stands support the splitter plate.

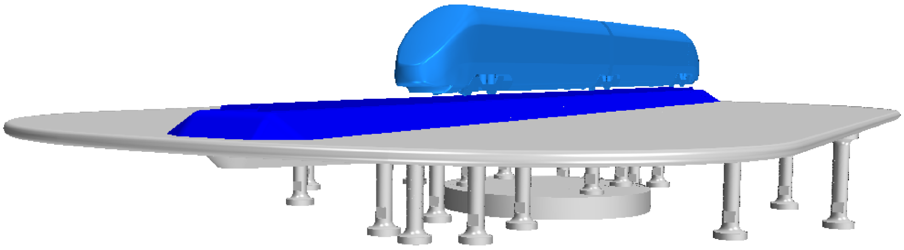

Figure 5 – Geometry of the 1:25 EC250 2-car model (light blue) mounted in the STBR (blue) and the splitter plate (gray).

1.3.2.4 Instrumentation Requirements

The measurement of the aerodynamic coefficients were performed with a force and moment balance. The tests in the KKK used a piezo-resistive force transducer type 796-6C from RUAG.

1.3.2.5 Reynolds Number

The Reynolds number shall be greater than $2.5 \cdot 10^5$, to achieve a supercritical condition. The norms require tests with three different flow velocities to demonstrate that the results are Reynolds independent. The recommended range is from $[0.6{\cdot}\mathrm{Re}_{\mathrm{max}}, \mathrm{Re}_{\mathrm{max}}]$. The experiments were conducted at Reynolds number $3.5 \cdot 10^5$, $5.2 \cdot 10^5$ and $7.0 \cdot 10^5$ and were proven to be Reynolds independent (see Figure 6). In this work, the analysis is made with respect to the wind tunnel results for Reynolds number $7.0 \cdot 10^5$.

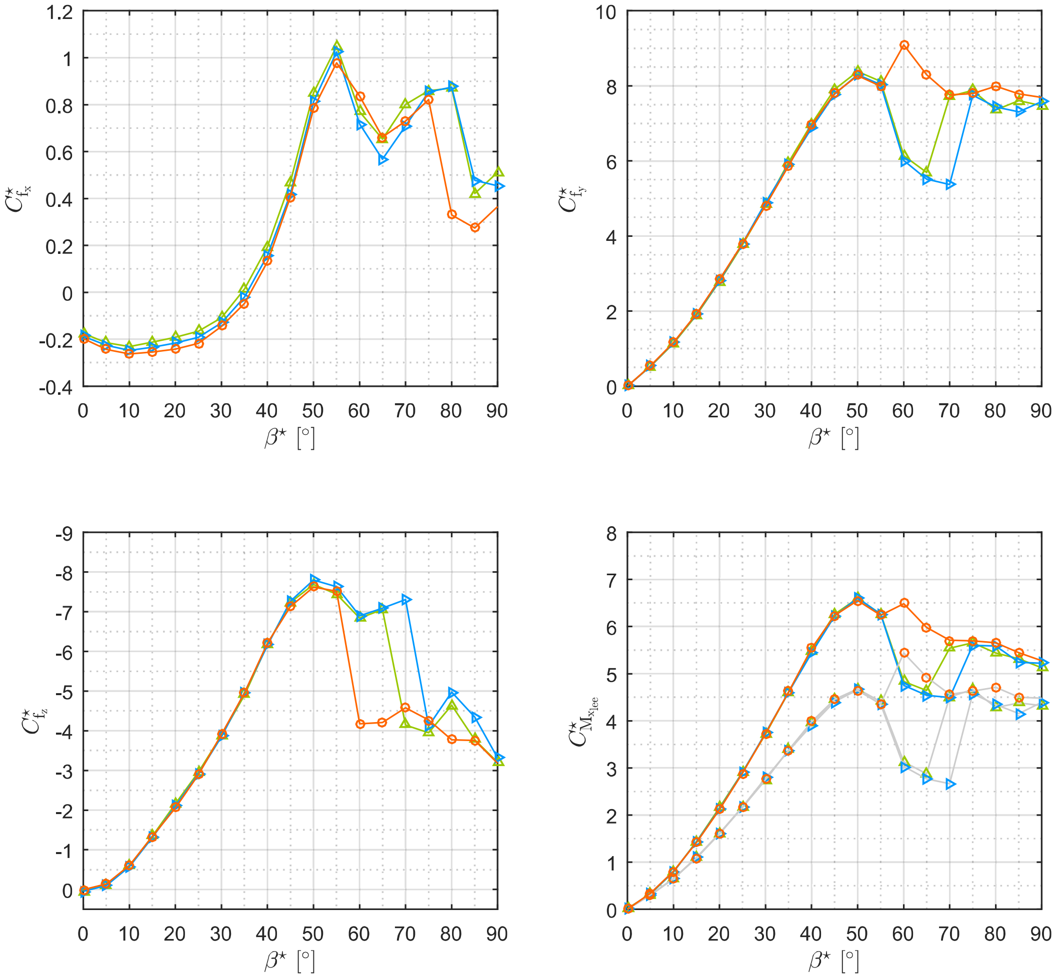

Figure 6 – KKK measurements of aerodynamic coefficients as function of the yaw angle for Reynolds number $3.5 \cdot 10^5$ (red ○), $5.2 \cdot 10^5$ (blue ▷) and $7.0 \cdot 10^5$ (green △). Analysis for C_{f_x}, C_{f_y}, C_{f_z} and $C^*_{M_{x,\mathrm{lee}}}$, $C^*_{M_x}$ in gray.

1.3.2.6 Symmetry

The tests are always performed in both positive and negative directions, from 0° to 90° and 0° to −90°. This provides a way to judge the quality of the wind tunnel results by comparing the left and right side coefficients, respectively. The symmetry of the results from the KKK tests are given in Figure 7 for Reynolds number $7.0 \cdot 10^5$ and show similar values.

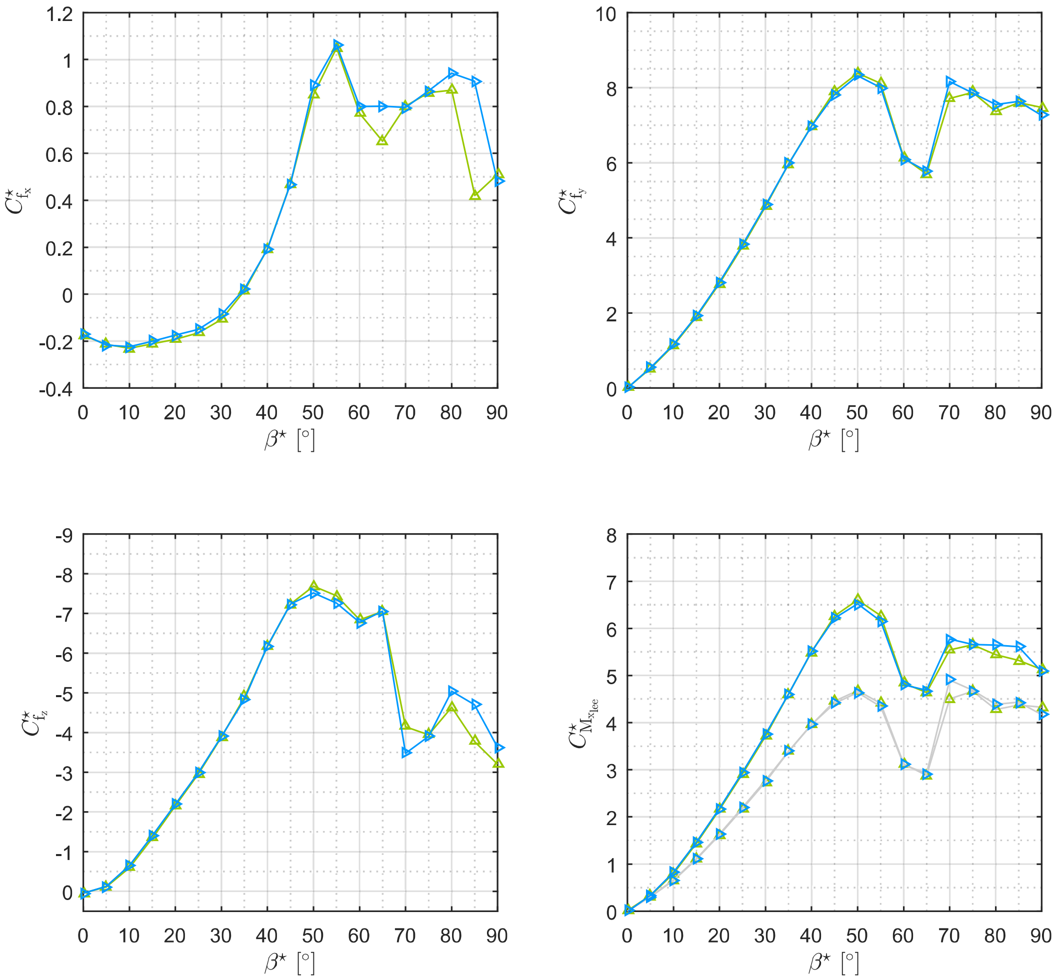

Figure 7 – KKK measurements of aerodynamic coefficients from 0° to 90° (green △) and 0° to −90° (blue ▷). Analysis for C_{f_x}, C_{f_y}, C_{f_z} and $C^*_{M_{x,\mathrm{lee}}}$, $C^*_{M_x}$ in gray.

1.4 Literature Review

The following sections describe the different studies performed in wind tunnels for crosswind analysis and the different factors that can affect the measured aerodynamic coefficients. Such factors include the Reynolds number, the moving model, atmospheric boundary layer, the model geometry details and ground topography.

1.4.1 Flow Nature

The flow around high-speed trains under crosswind conditions can be characterized into two regimens: a steady slender body flow behavior and unsteady vortex shedding behavior. For yaw angles up to 40° the flow condition is similar to the steady slender body flow, as investigated in the wind tunnel experiments on an idealized train model from Mair & Stewart (1985) and three-dimensional simulations from Copley (1987). The wake of the train consists of fixed vortex structures in space and time. After the boundary layer on the train roof leeward side separate, the separated shear layers roll up forming the steady vortex structures (Robinson; Baker, 1990; Baker, 2010). This behavior is illustrated in Figure 8.

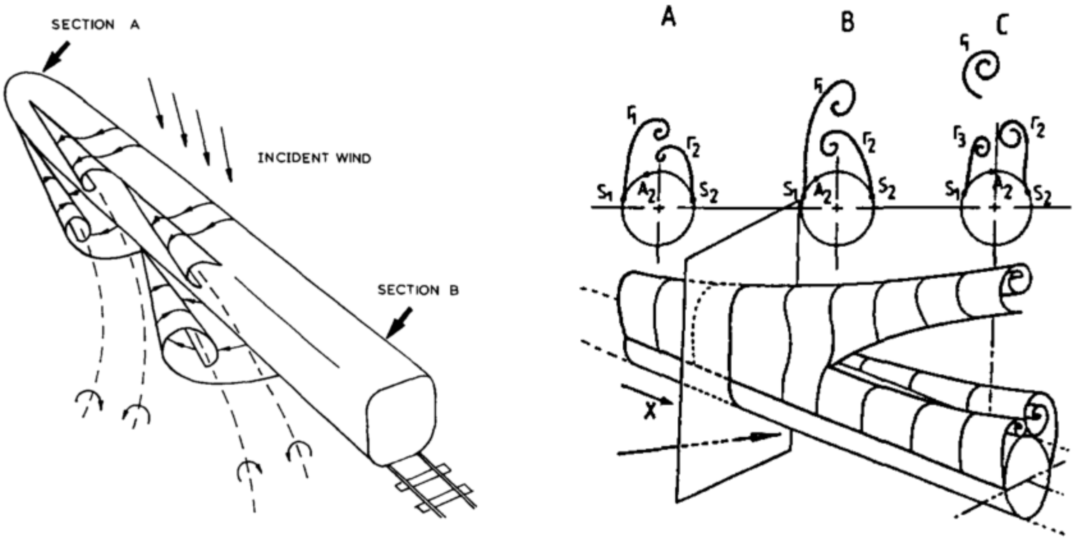

Figure 8 – Illustration of the wake formed in the lee-side of a train under crosswind condition (left) and the formation of the unsteady vortex structures (right), adapted from Copley (1987).

Copley (1987) observed that from 50°, the wake far from the nose becomes similar to a two-dimensional flow, with the cores of the vortices becoming parallel to the train axis. Chiu & Squire (1992) confirmed this behavior in their experiments, observing that vortex shedding already occurs at low yaw angles, however, farther from the nose.

At higher yaw angles ($\sim 70° - 80°$) the distance from the nose where vortex shedding begins becomes smaller. These vortices are shed along the entire length of the train. This behavior is similar to the flow behind a circular cylinder normal to the stream (Robinson; Baker, 1990), in a cross-flow conditions. The two-dimensional behavior is also identified by analyzing the pressure distribution away from the nose, as it remains unchanged at higher yaw angles from $x/D > 4.5$ (Chiu, 1995), being x the position evaluated and D the train height (see Figure 9).

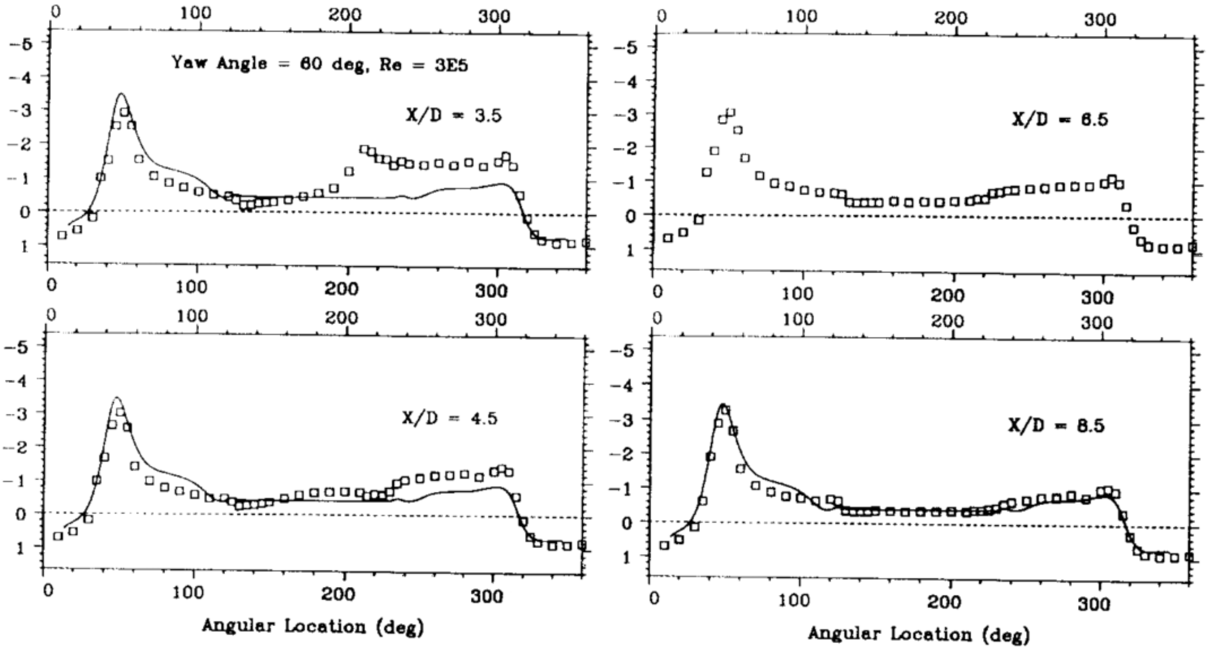

Figure 9 – Pressure coefficient distribution over different locations on the model surface, experimental and numerical analysis, adapted from Chiu (1995).

Between 50° to 70° the flow presents both the steady slender body flow and unsteady vortex shedding flow nature. The flow can characterized as unstable, switching between both regimens intermittently, producing widely varying forces upon the train (Robinson; Baker, 1990). This dual nature of the flow can be summarized schematically in Figure 10, where the variation of the flow nature with respect to the yaw angle and nose distance is presented.

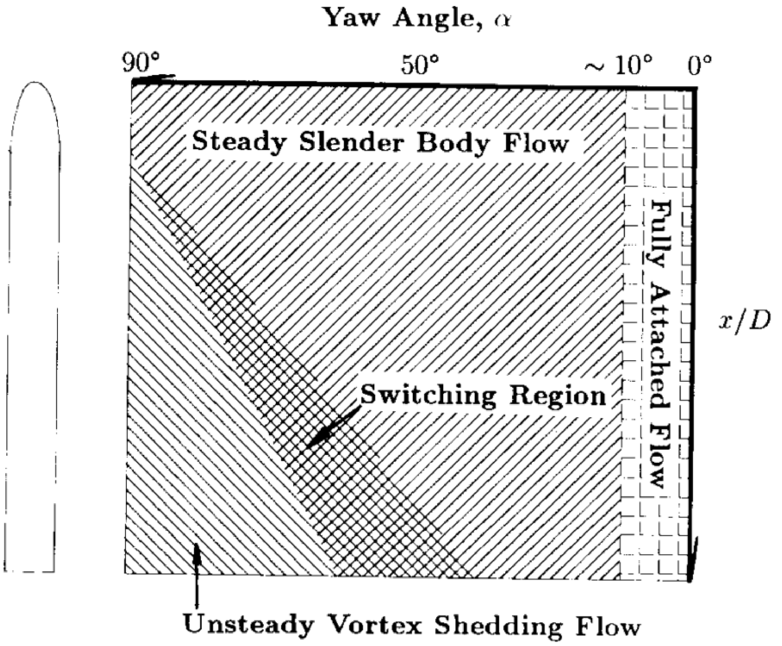

Figure 10 – Variation of the flow naure with respect to the yaw angle, from Chiu & Squire (1992).

As stated by Robinson & Baker (1990), the region of greatest practical interest with high-speed trains is for yaw angles between 10° and 50°, which is very similar to isolated steady slender bodies flow (Thompson & Morrison, 1971). As this range can be defined as steady, it is possible to use steady CFD simulations to analyze the flow, such as Reynolds averaged Navier-Stokes (RANS) simulations.

1.4.2 Reynolds Number

High-speed trains can reach Reynolds numbers from the order of 10^7 in full-scale. However, most wind tunnels testing achieve Reynolds numbers up to $\sim 10^5$. Since a scaled model is used, it is necessary to prove Reynolds number independence for the wind tunnel tests. Bocciolone et al. (2008) demonstrated the effect of the Reynolds number for different yaw angles (see Figure 11). The results show that no significant effects occurs for Reynolds number of same order of magnitude, as the aerodynamic coefficients are similar for the three Reynolds numbers analyzed. This is also observed for the Stadler EC250 high-speed train DLR-KKK results, as previously presented in Figure 6.

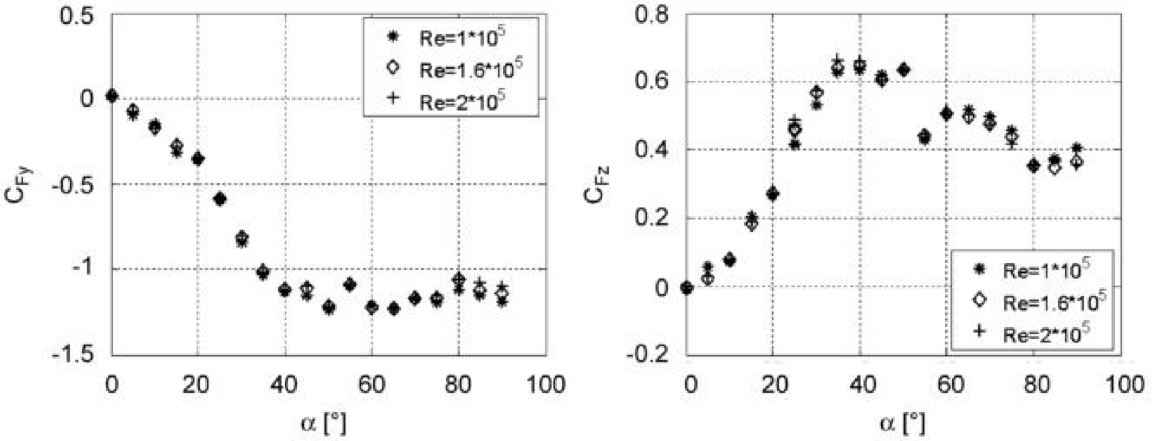

Figure 11 – Wind tunnel measurements of lift and side force coefficients as function of the yaw angle for different Reynolds number (Bocciolone et al., 2008).

The analysis of the Reynolds number is important as it can affect the behavior of flow separation and reattachment. Copley (1987) described that at low Reynolds numbers and moderate yaw angles the flow separates in the roof windward corner and does not reattach. Increasing the Reynolds number, up to critical condition, leads to the reattachment of the flow and forming a separation bubble at the roof windward corner, depending on the model roof angle (see Figure 12).

At higher Reynolds numbers the bubble is suppressed and the flow becomes fully attached, regarded as super-critical condition. As it is not possible to achieve realistic Reynolds numbers inside wind tunnels, the chosen experimental Reynolds number must render an attached flow over the windward corner of the roof to ensure similarity with realistic full-scale flow.

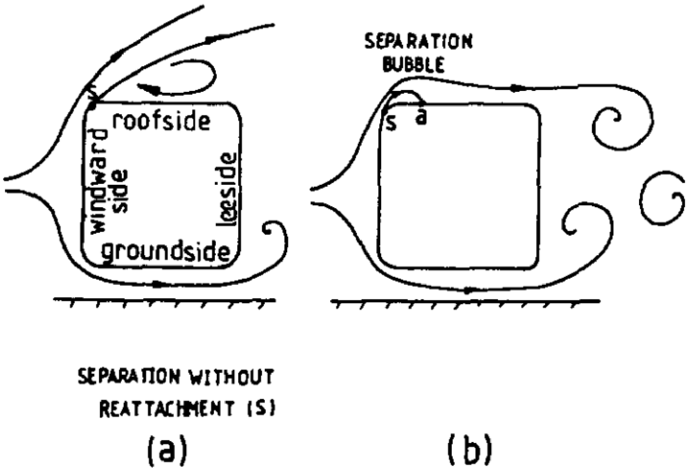

Figure 12 – Reynolds number effects on flow separation and reattachment. (a) At low Reynolds number the flow does not reattach, (b) at critical values the flow there is the formation of separation bubble followed by flow reattachment (Copley, 1987).

1.4.3 Moving Model

Standard wind tunnel tests do not account for the relative motion between the vehicle and the ground as the models are static. When a train is running on rails, the crosswind is defined as the relative wind between the train motion and the gust, while in static tests, the relative wind corresponds to the wind velocity blown.

The use of moving models was first presented by Baker (1986), Robinson & Baker (1990) and Baker (1991), laying the base for later analysis. Baker (1986) describes the difficulties of setting a moving model test as it requires a dedicated facility. In their experiments a launching rig catapulted the model and reproduced the train motion. To simulate a smooth train motion the tracks construction has to be precise, this is necessary as external forces on the wheels affect the measurements of the aerodynamic coefficients. The measurement system is also difficult to set up as it must stay with the model throughout the tests. Baker (1991) found that for moving models the side force decreases and the lift coefficient increases, resulting in a similar lee-rail moment coefficient compared to static tests. Baker et al. (2004) remarks that the vertical force component is most affected by the nature of the under-body flow for a moving model.

Bocciolone et al. (2008) avoided the use of a complex catapult mechanism by using a launching ramp, where the train is accelerated as it goes down the ramp. Bocciolone et al. performed both static and moving model tests, demonstrating that the train motion has no significant influence on the lift and side force coefficients for low yaw angles, as shown in Figure 13. For yaw angles above 40° the lift coefficient is higher and presents a higher deviation than observed for smaller angles.

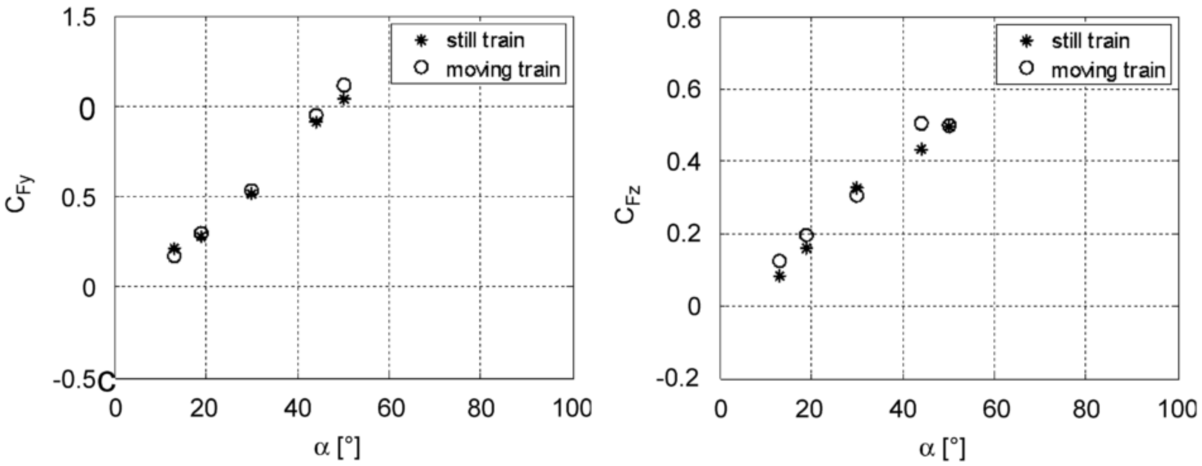

Figure 13 – Comparison of the aerodynamic coefficients for static and moving models from Bocciolone et al. (2008).

Dorigatti et al. (2012, 2015) presented similar findings, showing that pressure distribution is similar for both static and moving models. The analysis of the mean aerodynamic load coefficients also shows that the moving model has a lower side force and rolling moment coefficients while presenting a higher lift coefficient (see Figure 14). The authors remark that limited differences are found between the pressure distribution and aerodynamic loads for static and moving analysis.

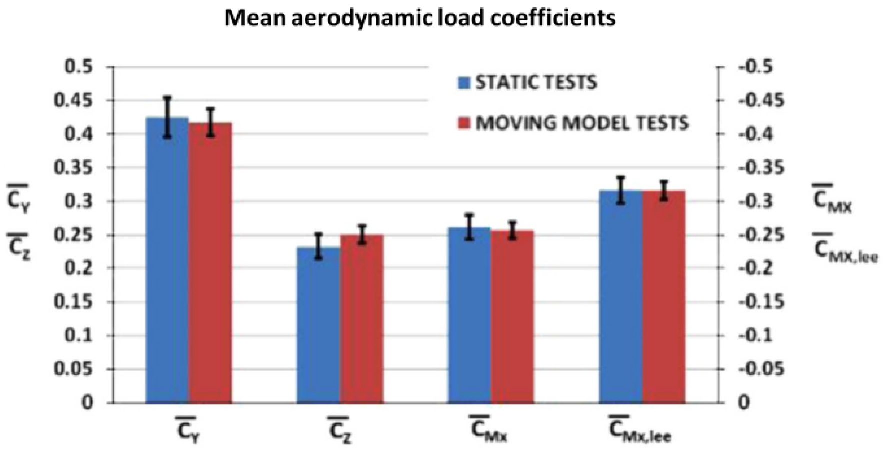

Figure 14 – Comparison of the aerodynamic coefficients for static and moving models, adapted from Dorigatti et al. (2015).

1.4.4 Atmospheric Boundary Layer

Standard wind tunnels have a low turbulence, constant velocity profile inlet and, therefore neglect the effect of an atmospheric boundary layer (ABL). Baker (1986) and Robinson & Baker (1990) not only discuss the importance of reproducing the ABL within wind tunnel tests, but also the difficulties involved in setting up such an experiment. The major difficulty lied in simulating an ABL length scale that matches the scale of the model.

The results from Robinson & Baker (1990) indicates that the aerodynamic forces and moment are strongly affected by the turbulence length scale and intensity. They achieved different levels of turbulence by using grids at the inlet of the test-section. The impact of the turbulence intensity and length scale on the side force coefficient is presented in Figure 15, where a large turbulent scale (Grid 1) increases the side force and small scales (Grid 2 to 4) reduce it. According to the authors, this occurs because the vortices associated to the wake gain or lose energy depending on the wake vortex size relative to the scale of the turbulence length. A gain of energy is associated with large structures, which increases the side force, and vice-versa.

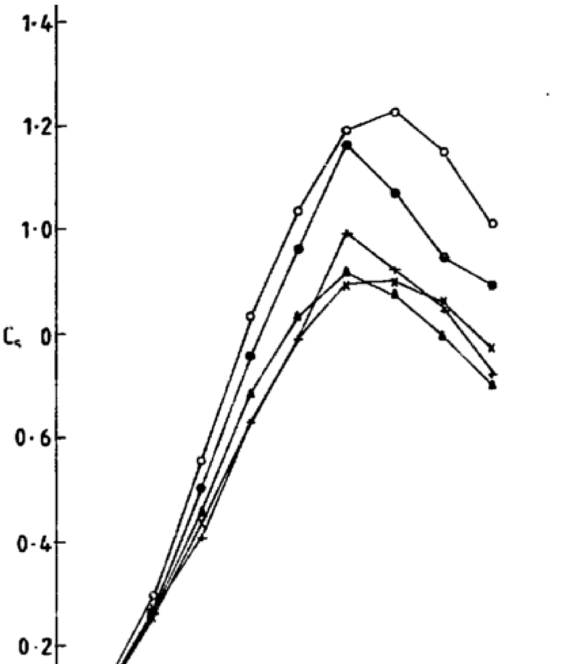

Figure 15 – Effect of the turbulence intensity on the side force coefficient. The turbulence intensity and length scale (m) are given: 0.007 and - for Grid 0, 0.106 and 0.130 for Grid 1, 0.065 and 0.067 for Grid 2, 0.050 and 0.060 for Grid 3 and 0.106 and 0.074 for Grid 4. (Robinson & Baker, 1990).

Bocciolone et al. (2008) also performed experimental analysis on the influence of the ABL. Accordingly to Robinson & Baker, Bocciolone found that high turbulence leads to an increase of the lift coefficient at higher angles, as shown in Figure 16.

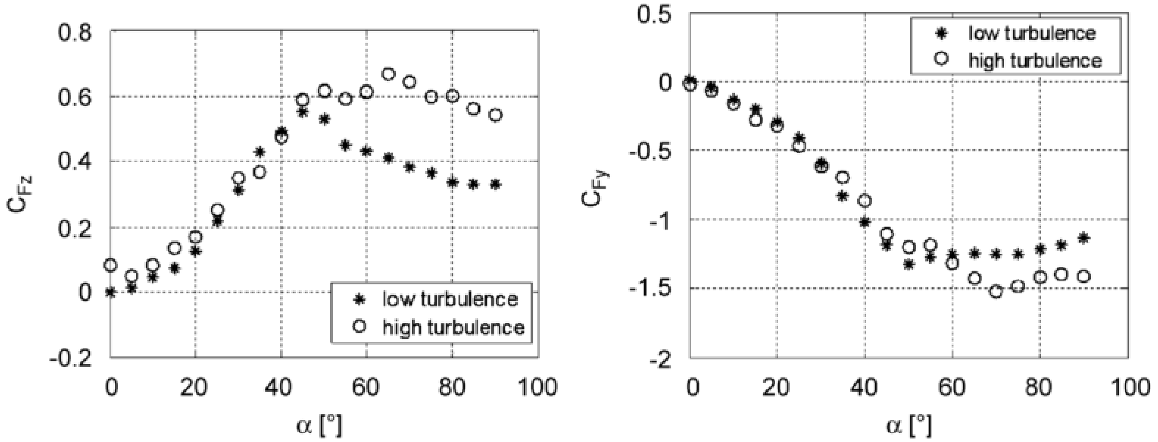

Figure 16 – The effect of turbulence on lift and side force coefficients, from Bocciolone et al. (2008).

Although the use of an ABL is important for crosswind analysis, the DLR-KKK uses a low turbulence block profile, as required by the EN-14607-6 norm, as it guarantees reproducibility of the results.

1.4.5 Model Details

The EN-14607-6 states that for reduced-scale wind tunnel testing the vehicles should be modeled with a sufficient accuracy not to result in unrealistic flows, as minor simplifications can change the position of flow separation and change the aerodynamic rolling moment. The norm requires that aerodynamically significant features on the train side and roof be modeled.

To assess the influence of model detailing, Deliancourt (2015) studied the impact of the scaling of roof lines on the aerodynamic performance of vehicles in the wind tunnel. The wind tunnel experiments and numerical simulations were performed on both the idealized train model proposed by Copley (1987) and an idealized regional model, based on a commercial train (Figure 17).

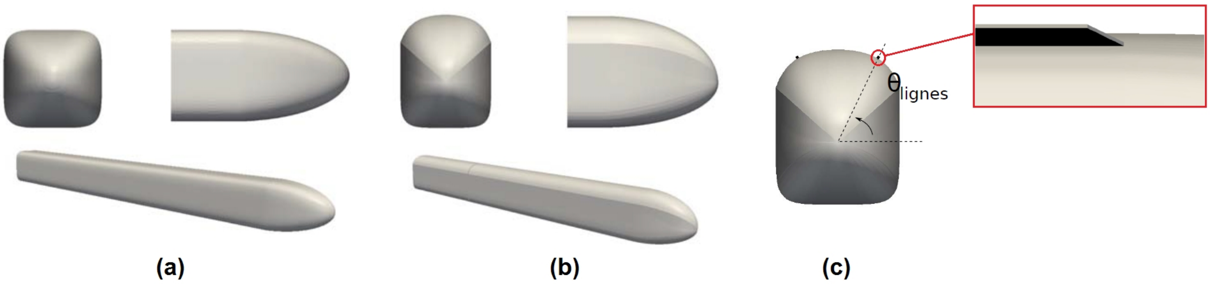

Figure 17 – Representation of: (a) the idealized train model; (b) the idealized regional model and (c) the model with roof lines, adapted from Deliancourt (2015).

The addition of roof lines changes the aerodynamic forces and consequently the overturning moment (see Figure 18). The side force coefficients increases along the lee-rail moment, while the lift coefficient reduces for a simplified train model. Thus, the risk of train overturning increases with the addition of roof lines.

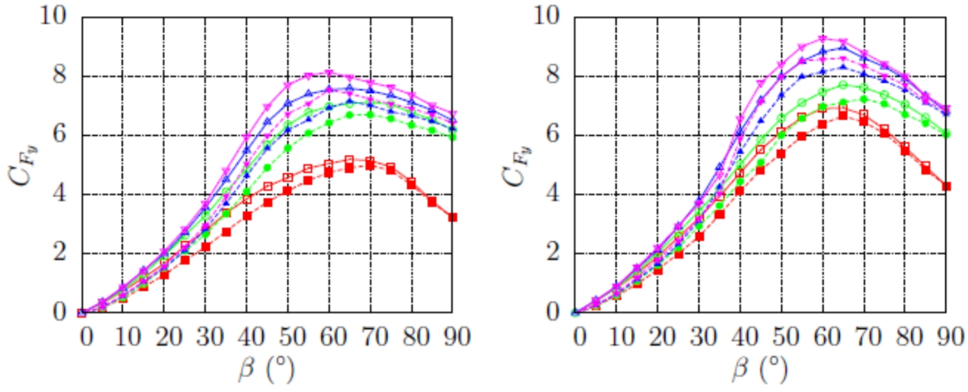

(a) Modèle idéalisé (b) Modèle régional

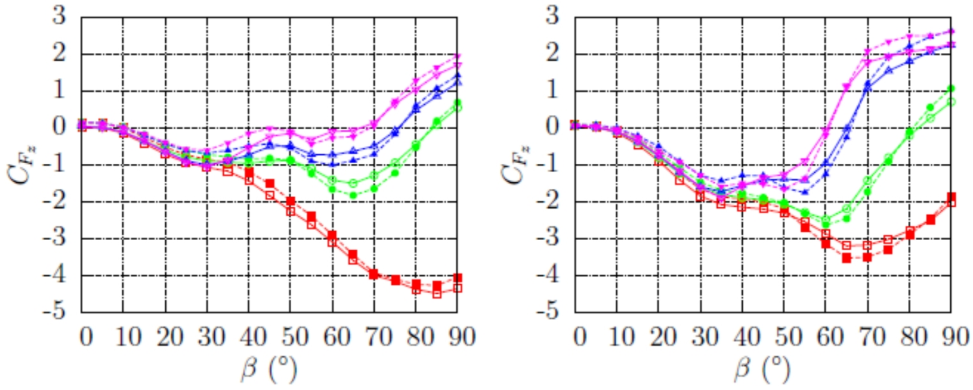

(c) Modèle idéalisé (d) Modèle régional

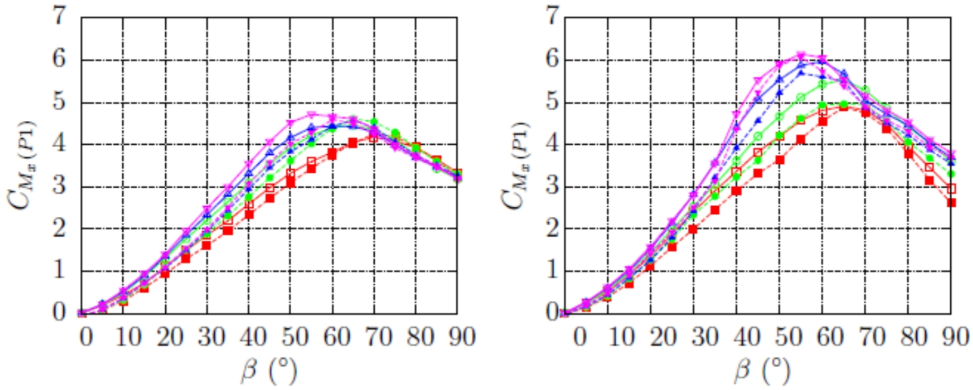

(e) Modèle idéalisé (f) Modèle régional

Figure 18 – The effect of model detailing in the aerodynamic coefficients, from Deliancourt (2015). The experimental results are presented for the smooth model without lines (red square) and the smooth model with lines with homothetic ratios: 2/3 (green circle), 1 (blue triangle) and 4/3 (pink triangle). The results are presented for both idealized train model (left) and idealized regional model (right).

The roof lines cause the formation of vortices in their wake, which interact with the surface and modify the pressure distribution around the vehicle, and then interact with the train wake (illustrated in Figure 19). The increase of the roof line homothetic ratio implies in increasing the lee-rail moment, as seen in Figure 18 for the ratios of 2/3 (green circle), 1 (blue triangle) and 4/3 (pink triangle) in comparison with the model without lines (red square), for both idealized models.

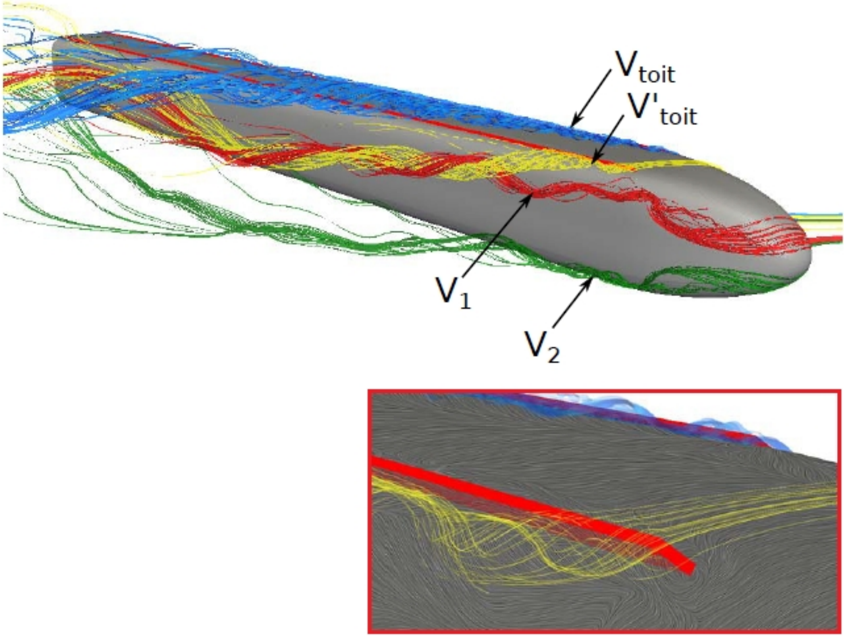

Figure 19 – Overall structure of the flow in the wake of the idealized train equipped with rows of roof lines of homothetic ratio 1. Numerical simulation results for $\beta = 45°$, adapted from Deliancourt (2015).

Deliancourt (2015) proved that the level of the details, as also mentioned by the EN-14607-6 standards, is crucial on determining the crosswind stability, as it contribute to an increase of the aerodynamic coefficients, mainly the $C^*_{M_x,\text{lee}}$.

1.4.6 Topography

Schober et al. (2010) investigated the influence of the different ground configurations in the aerodynamic coefficients. Their work addressed the influence of the True Flat Ground (TFG), the 6m embankment and the STBR. Schober showed that the analysis of train stability has strong dependency on the ground configuration. From the three configurations analyzed, the 6 m embankment presented the highest coefficients.

However, both the 6 m embankment and STBR configurations are finite, and the ground geometry can affect the flow. The tip of the track in wind tunnel generates a vortex that interacts with the train wake, affecting the measured coefficients. This tip vortex can be represented as shown in Figure 20.

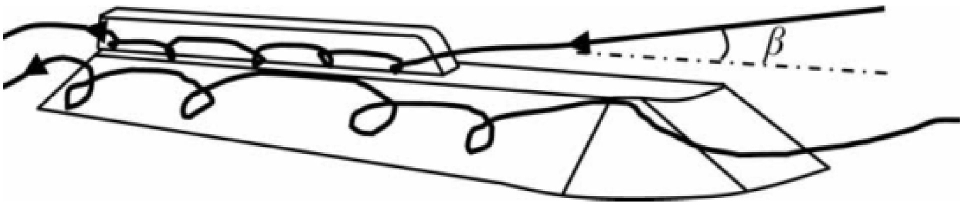

Figure 20 – Illustration of vortices produced by a finite embankment and train, from Diedrichs et al. (2007).

To avoid generating this tip vortex, Diedrichs et al. (2007) stretched the embankment across the entire test section of the wind tunnel. Although this effect is expected in finite ground configuration setup, there are no studies to quantify its influence on assessing crosswind stability.

As there is no report of the influence of the ground configuration in the flow, this study will address the results for both standard and infinite STBR.

1.4.7 Intake & Exhaust Systems

High-speed trains propulsion systems achieve high temperatures and it is necessary to maintain it in safe operational temperatures to avoid failures. Generally those systems are air- or water-cooled. The train also counts with acclimatization systems for passenger comfort. These systems take fresh air from outside and exhaust the hot air.

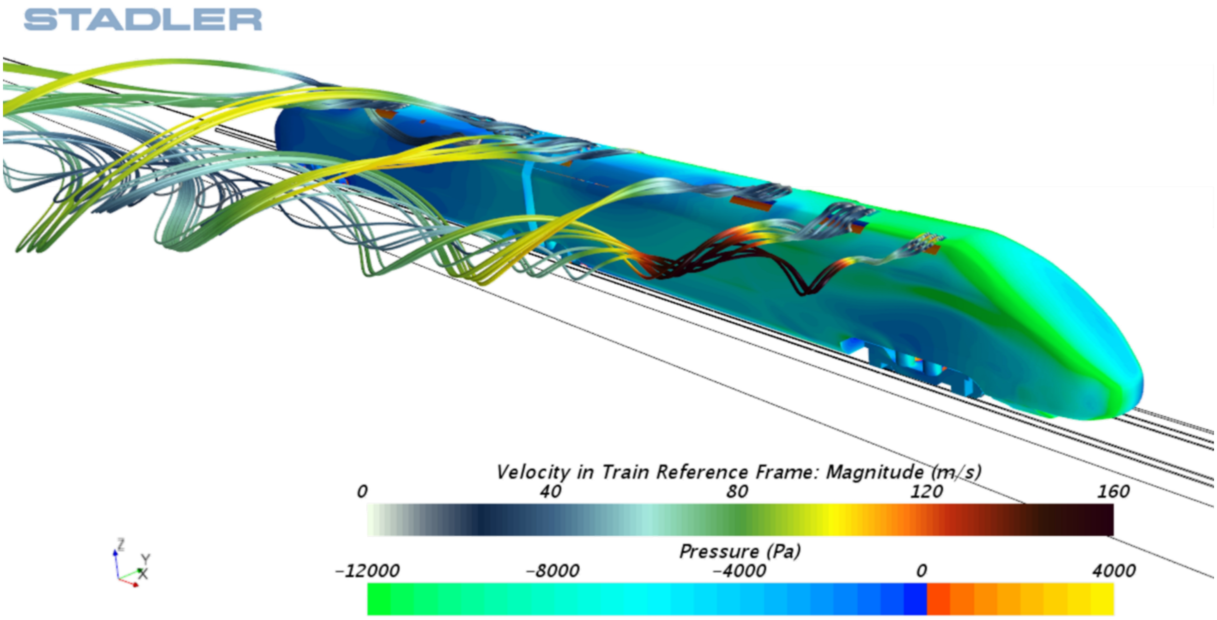

Figure 21 – Illustration of vortices produced by the train intake and exhaust system's inlets and outlets and the interaction with the train wake.

The inlets and outlets from the cooling systems alter the flow (see Figure 21) around the trains and are not taken into account in standard wind tunnel tests. As it is complex to model the intake and exhaust of the train within wind tunnel, CFD tools can analyze how these systems affect the flow. The aim of this thesis is to determine if the cooling equipment affect or not the crosswind stability of high speed trains, and hence, produce new information that improves the safety of high-speed trains under crosswind assessment.

1.5 Objectives

The standard wind tunnel tests present three major issues: the Reynolds number within the wind tunnel ($\sim 10^5$) is small compared to full-scale ($\sim 10^7$) and the static models do not reproduce the relative ground motion or account for the air flow of the train cooling equipment. To the author knowledge, no record of the influence of the last two aforementioned issues (Sections 1.3.2.2 and 1.4.7) have been reported. To analyze these factors Computational Fluids Dynamics (CFD) was used to simulate the flow.

To improve the safety of high-speed trains under crosswind conditions this thesis addresses those issues by fulfilling the following goals:

- Validate the CFD simulations with respect to wind tunnel results;
- Parametrize the influence of a moving model for the Single Track Ballast and Rail (STBR) configuration;
- Define if the train stability is affected, or not, by the flows of the air intake and exhaust systems.

The following objectives were set to fulfill these goals:

- Validate the turbulence model and mesh configuration from the experimental results;
- Study the influence of the wind tunnel size by increasing the DLR-KKK width;
- Analyze the effects of the ground topography by comparing the results from a standard and infinite STBR;
- Simulate the relative train/ground motion with a moving reference frame (MRF) and assess its influence;
- Compare the results from reduced-scale and full-scale moving models;
- Model the inlets and outlets of the full-scale Stadler EC250 and discuss the changes of the aerodynamic coefficients.

2 Methodology

Computational Fluid Dynamics (CFD) was used to understand the flow around a high-speed train in crosswind situations. The flow was simulated with the commercial solver STAR-CCM+ version 11.02 from CD-adapco. STAR-CCM+ solves the incompressible Navier-Stokes equations using a finite-volume method.

The study, as this chapter, is divided to two parts; validation and investigation. Section 2.1 describes the methodology used to validate the CFD results. The setup that produced the best results in the validation was then used to investigated the influence of some key parameters.

Section 2.2 presents the methodology used to analyze the influences of the wind tunnel size, the STBR, the moving model and last, but not least, the intake and exhausts systems.

2.1 Validation

This section reports the methodology used to validate the CFD results. As the CFD results were validated using the EC250 aerodynamic coefficients measured in the DLR-KKK wind tunnel for Reynolds number of $7 \cdot 10^5$, the first part of this section describes the numerical domain that reproduced, as closely as possible, the wind tunnel setup. The second and third parts present the different turbulence models that were tested as well as the different meshes on which they were tested.

2.1.1 Computational Domain

CFD simulations are performed on a computational domain. A detailed reproduction of the DLR-KKK wind tunnel was produced to validate the CFD simulations. The $1/25^{th}$ EC250 model, STBR and splitter plate with stands were modeled to ensure a complete similitude between the wind tunnel and simulated flow, as shown in Figure 22. This computational domain is referred as Domain A.

The domain dimensions are given in Section 1.3.2.2, and presented relative to the train model height h in Figure 22. The domain cross-section has an are of $15h$x$15h$ and a total length of $68h$, the splitter plate center is located at $17h$ from the inlet.

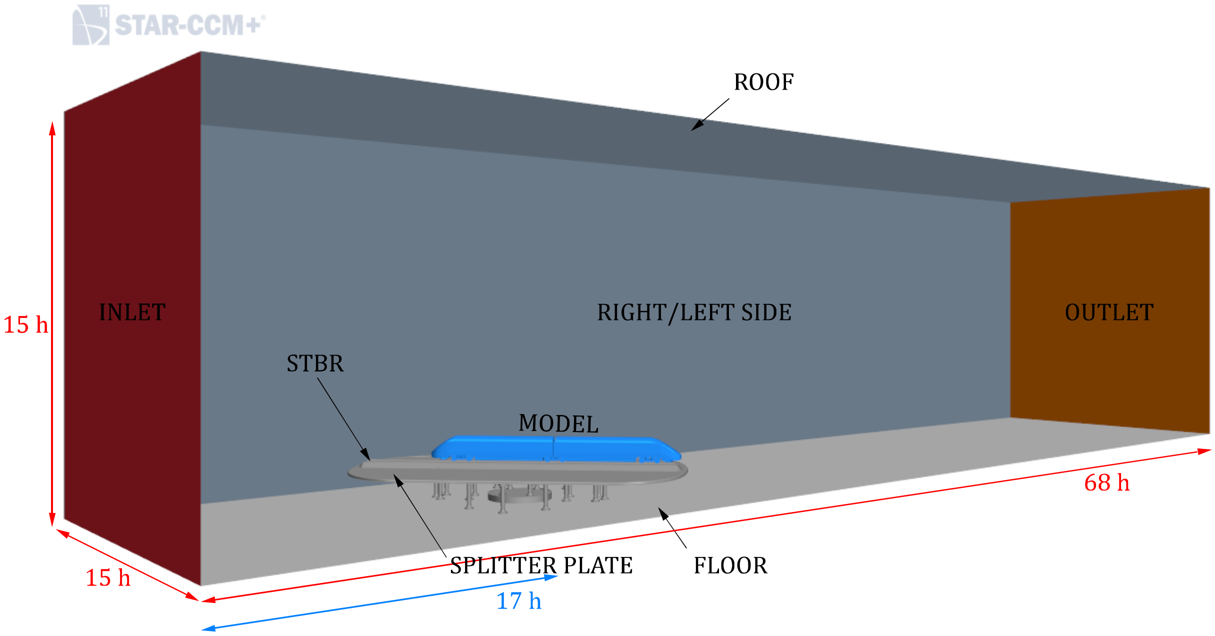

Figure 22 – Computational representation of the DLR-KKK wind tunnel (c.f. Domain A). The dimensions are given with respect to the train height h.

The boundary conditions are presented in Table 1. They reproduce the wind tunnel flow conditions with a Reynolds number of $7 \cdot 10^5$. The turbulence intensity at the inlet was set to 1%, which corresponds to the DLR-KKK data. In the simulation, the turbulence velocity scale was set to 1 m/s and the turbulent viscosity ratio set to 10.

Surface	**Boundary Condition**	**Value**
1/25th EC250	Wall	No-slip
STBR	Wall	No-slip
Splitter Plate	Wall	No-slip
Roof	Wall	No-slip
Floor	Wall	No-slip
Left Side	Wall	No-slip
Right Side	Wall	No-slip
Inlet	Velocity-inlet	90 m/s
Outlet	Pressure-outlet	0 Pa

Table 1 – Boundary conditions applied in Domain A for the validation of the simulation results.

2.1.2 Turbulence Models

Different turbulence models were analyzed during the validation phase (see Table 2). In this study, as the flow is considered steady, the Navier-Stokes (NS) equations are simplified by time-averaging resulting in the Reynolds-Averaged Navier-Stokes equations (RANS).

Turbulence Model		**Description**
Spalart-Allmaras*		The SA model is a one-equation model that has a good behavior for attached flows (Spalart & Allmaras, 1992). The model is economical and robust. However, it under-predicts separation.
$k-\varepsilon$	Standard*	The Standard $k-\varepsilon$ is a general purpose two-equation model (Jones & Launder, 1972). Although it is robust, it has low accuracy for separated flows and its results are affected by wall-functions implementation.
	Realizable	Introduced by Shih et al. (1995), the two-equation model presents good performance for separated flows, swirling and rotating flows, and flows with large streamline curvature.
	v^2f	A four-equation model, extension of the $k-\varepsilon$ (Davis, Rinehimer & Uddin, 2012). Differently from standard two-equation models, the v^2f model accounts for the effects of near-wall anisotropy and presents good prediction of flow separation.
	Elliptic Blending	The Elliptic Blending model was proposed by Billard & Laurence (2011) as a modification of the v^2f model. It accounts for the effects of near-wall anisotropy with similar benefits of the v^2f, but with the added advantage of being more robust.
$k-\omega$	Standard*	The $k-\omega$ is a two-equation model introduced by Wilcox in 1988, with revisions in 1998 and 2006. The model presents good behavior for near-wall and pipe flows, however it over-predicts separation.
	SST	A two-equation turbulence model presented by Menter (1993). The model is a blend of the $k-\omega$ and $k-\varepsilon$ models. The merit of the Shear Stress Transport (SST) model is its good behavior in adverse pressure gradients and separation flow. The model requires a fine near-wall mesh.
	SST γRe_θ	Introduced by Menter et al. (2004), the model is an extension of the SST model, with an extra two equations. It predicts the laminar-turbulent transitions better.
Reynolds Stress Transport Model (RSM)		The RSM turbulence model was developed to fully model anisotropy by modeling the six Reynolds-stress tensor components, introduced in the work from Launder, Reece & Rodi (1975). The RSM is a seven-equation model and extremely dependent on the mesh resolution, being less stable than the other RANS models.

Table 2 – The different RANS turbulence models applied in flow modeling, adapted from CD-adapco (2015). The described models are used to validate the simulation results, except the ones marked with *.

2.1.2.1 Reynolds-Averaged Navier-Stokes Equations

The RANS uses a statistical description of turbulence, as proposed by Reynolds (1895). The NS equations are decomposed into their average and fluctuation parts. The RANS equations are written as:

$$\frac{\partial(\rho\overline{u_i})}{\partial x_i} = 0 \tag{2.1}$$

$$\frac{\partial\rho\overline{u_i}\,\overline{u_j}}{\partial x_j} = -\frac{\partial\overline{p}}{\partial x_i} + \frac{\partial}{\partial x_j}\left[\mu\left(\frac{\partial\overline{u_i}}{\partial x_j}\right) - \rho\overline{u_i^{'}u_j^{'}}\right] \tag{2.2}$$

where $\overline{u_i}$ are the averaged velocity components and $u_i^{'}$ the fluctuation components, ρ the fluid density, μ the dynamic viscosity and $\overline{p}$ the averaged pressure. Time-averaging introduces the tensor $-\overline{u_i^{'}u_j^{'}}$ known as the Reynolds-stress tensor.

For three-dimensional flows the four equations involve ten unknowns, $\overline{p}$, $\overline{u_1}$, $\overline{u_2}$, $\overline{u_3}$ and the six Reynolds-stresses components. To close the system, the Reynolds-stress tensor is superseded by turbulence models. The turbulence models described in Table 2 were used during the validation process, except the Spalart-Allmaras (SA), Standard $k-\varepsilon$ and $k-\omega$ models. The EN-14607-6 norm requires to use at least two-equation models, which excludes the SA model. Both Realizable $k-\varepsilon$ and SST models were chosen over the Standard $k-\varepsilon$ and $k-\omega$ models, respectively, as they are known to perform better for aerodynamic analysis.

As shown in Table 2, each model has its pros and cons. Each model has been analyzed to determine the one that gives the best results. After this validation phase, only one turbulence model was kept.

2.1.3 Computational Mesh

To solve the RANS equations in CFD, the finite-volume method (FVM) is applied. In the FVM the numerical domain is discretized in cells, which form the computational mesh. The RANS equations are then computed over each cell to solve the flow.

This study used a trimmed mesh. The mesh was composed of hexahedral cells, that were trimmed to the desired size. Finer cells were applied in regions with strong velocity and pressure gradients. This process is illustrated in Figure 23a: (1) a uniform template mesh was generated, (2) the geometry profile (in red) was trimmed, (3) the mesh was trimmed to match the surface sizing and (4) a final trim was performed to obtain a homogeneous mesh. The process generated high quality mesh by having predominantly hexahedral cells with polyhedral cells close to the surface. Each cell level has a 1:2 size ratio with the finer next level. The refinement of the boundary layer region was achieved by applying a prism layer mesh around the model surface. The prism layers resolved the strong near-wall velocity gradient with more accuracy (CD-adapco, 2016), as shown in Figure 23b.

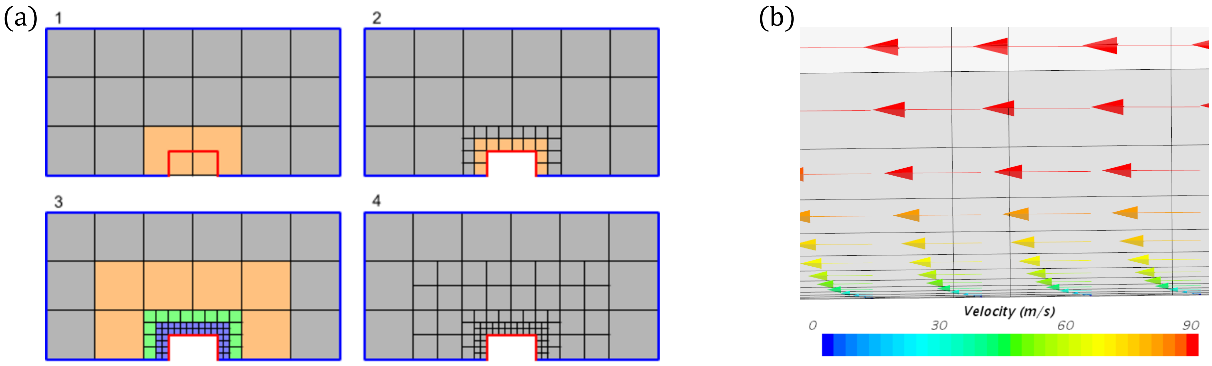

Figure 23 – (a) The trimmed mesh process: 1-uniform template mesh; 2-trimming the geometry profile; 3-trimming to match surface sizing; 4-final trim for homogeneous mesh. From CD-adapco (2016). (b) Representation of the prism layer mesh with velocity vectors at the boundary layer region.

The prism layers total thickness had to cover the boundary layer near the wall-surface (see Figure 23b). The number of layers had to be sufficient to resolve the gradients normal to the surface, and, depending on the turbulence model, to achieve the required dimensionless wall-distance y+. Models as the SST and RSM resolve the viscous sublayer directly, but requiring a fine prism layer mesh with a $y+ < 3$. Models as the $k - \varepsilon$ use a coarser prism layer mesh by using wall functions, hence a $y+ > 30$ can be applied. To fulfill this requirements, 12 prism layers were applied for the SST and RSM models and 6 prism layers for the $k - \varepsilon$ models, with a prism layer growth ratio of 1.5.

2.1.3.1 Mesh Refinement

The mesh resolution plays an important role in the accuracy of the results. The mesh refinement was done using surface and volume controls. Surface controls refine the mesh on the model walls (see Table 3) while volume controls refine specific volumetric regions of the domain. Four volume controls were used to refine the wake region (VC1 and VC2), the train vicinity (VC3) and the under-body and tracks region (VC4), as shown in Figure 24. The sizing of each volume control relative to the train surface size was respectively 8:1, 2:1, 1:1 and 1:2.

Five mesh configurations were used to validate the results. To avoid flat cells (or pancake cells), the mesh was refined with a cell width to prism layer thickness ratio $d/h < 2.5$. The mesh was refined from Mesh I to Mesh II and then to Mesh III. For these meshes, volume controls VC1 and VC3 were applied. The surface control refinement, prism layer parameters and volume controls are presented in Table 3.

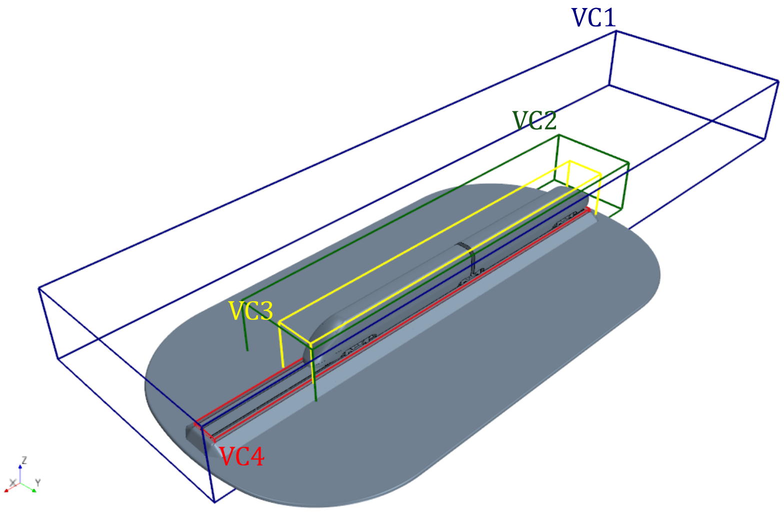

Figure 24 – Volume controls applied for mesh refinement. The refinement regions selected are the far (blue - VC1) and near wake (green - VC2) region ; the train vicinity (yellow - VC3); under-body and track region (red - VC4).

The refinement from Mesh I to Mesh III improved the results (see Section 3.1), however, the number of cells increased. With more cells, the CPU time to reach a converged solution also increases. Modeling the flow under the splitter plate requires a large number of cells as the flow between the stands has to be solved. To avoid spending resources on the flow under the splitter plate, a symmetry plane was applied in its horizontal half. This symmetry plane reduces by 20% the number of cells while keeping the aerodynamic coefficients within 1%. The domain with symmetry plane is referred as Domain B, and is shown in Figure 25.

Mesh	**Train Surface Control**	**Train Prism Layer Thickness**	d/h **Ratio**	**Volume Control**	**P.L. Number**	**Cells x10^6**
Mesh I	3 mm	1.2 mm	2.50	VC1	6	60
					12	100
Mesh II	2 mm	0.8 mm	2.50	VC1	12	150
Mesh III	1 mm	0.8 mm	1.25	VC1, VC3	6	100
					12	160

Table 3 – The different computational meshes applied for surface refinement during the validation phase for Domain A.

To improve the results, Mesh III was refined in regions of strong gradients. The mesh size in the volume of control VC2 was set to 2 mm and gave Mesh IV. Mesh V is equivalent to IV except for the cell size in VC4 which were set to 0.5 mm instead of 1 mm (as in VC3). Mesh V keeps the cell number bellow 160 million. Table 4 summarizes Mesh III, IV and V.

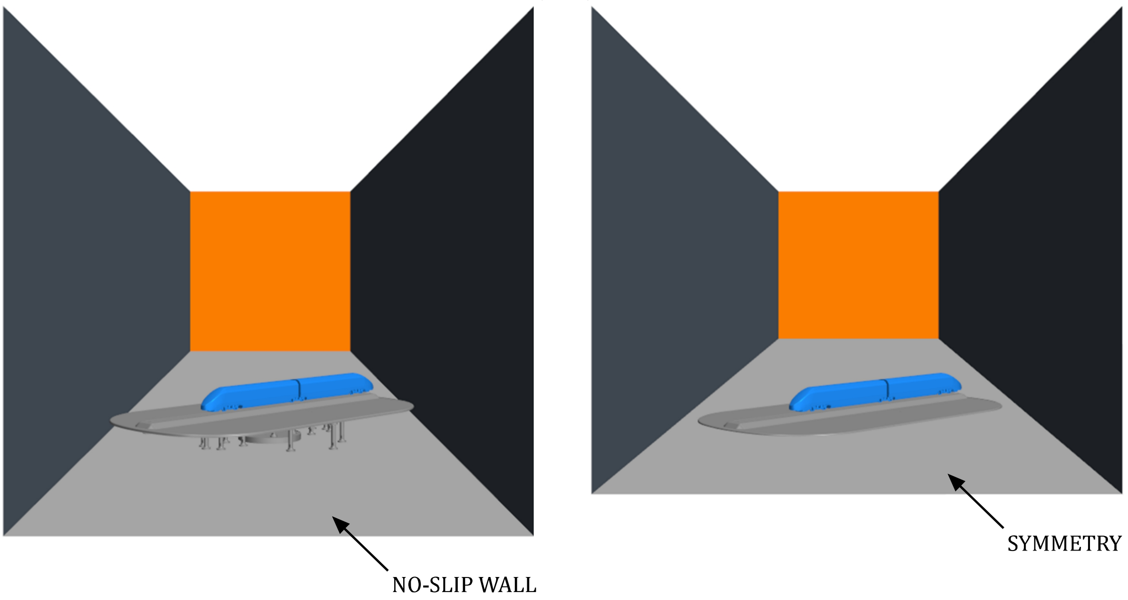

Figure 25 – Computational Domain A (left), with no-slip wall condition, and B (right), with symmetry plane condition.

Mesh	**Train Surface Size**	**Train Prism Layer Thickness**	**Volume Control**	**Cells x10^6**	**Domain**
Mesh III	1 mm	0.8 mm	VC1, VC3	160	Domain A
				130	Domain B
Mesh IV	1 mm	0.8 mm	VC1, VC2 VC3	140	Domain B
Mesh V	1 mm	0.8 mm	VC1, VC2 VC3, VC4	160	Domain B

Table 4 – Volume controls applied for mesh refinement.

Mesh V on Domain B (see Figure 26) gives the same number of elements as Mesh III on Domain A but gives better results. Mesh V was selected for the remaining of this study.

As can be seen in Figure 26 the resulting mesh is well refined. The use of the volume controls helps on refining the interest regions, resulting in a good representation of the model itself. In Figure 26, (a) represents the computational domain with a vertical plane crossing the train model longitudinally, (b) the mesh on this plane as well as on the train model, (c) & (d) show the refinement achieved with the volumes of control VC1 (blue), VC2 (green), VC3 (yellow) and VC4 (red), (e) & (f) show the mesh quality at the train nose and the prism layer mesh, (g) the refinement level at wake region and (h) the mesh and prism layers at the lee-ward roof corner of the train.

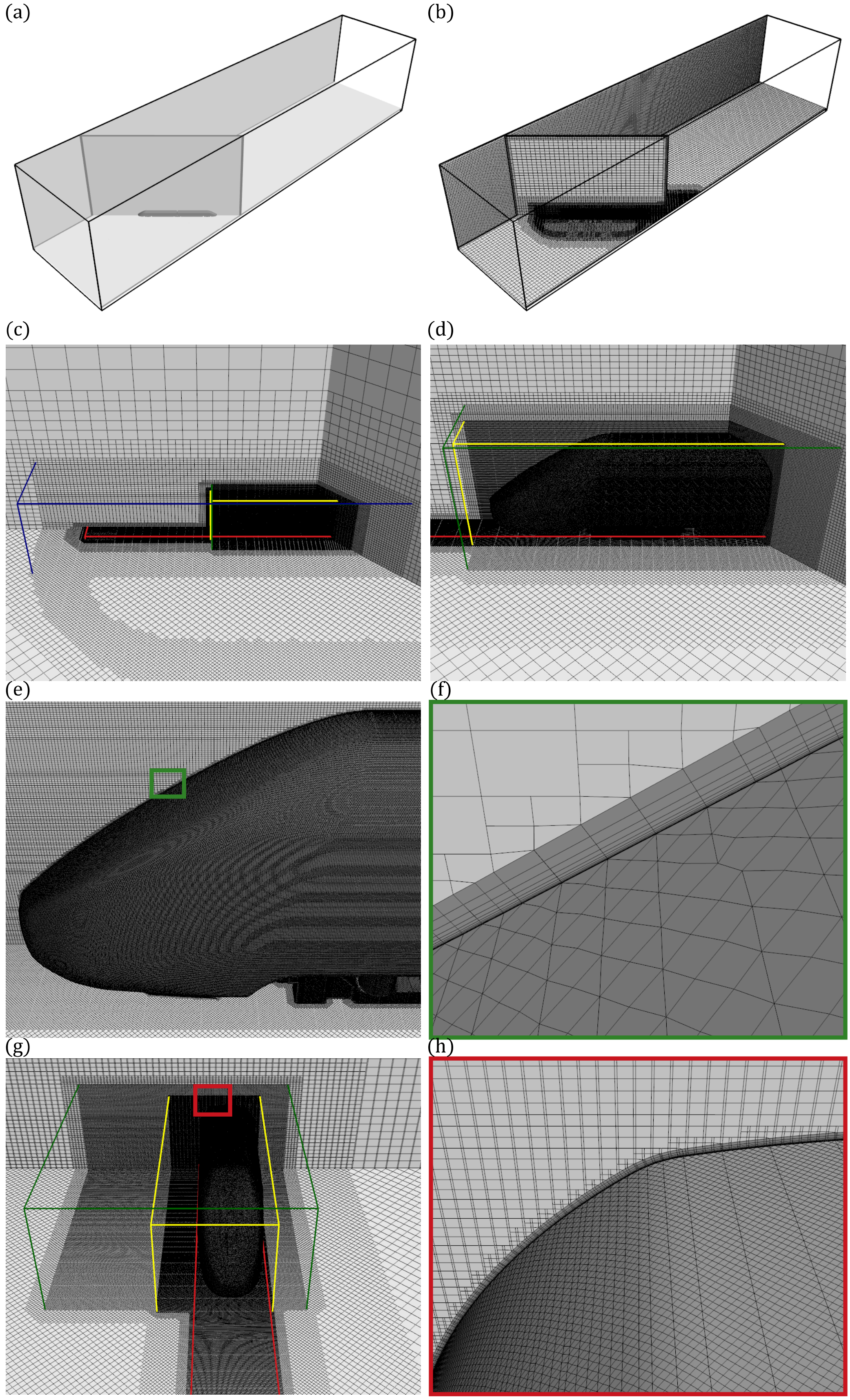

Figure 26 – Visualization of the mesh for the CFD calculations and the volume controls for Mesh V, Domain B.

2.2 Analysis

This section describes the computational domains and meshes used to study the effects of the wind tunnel size, the STBR geometry, the model motion and the effects of the air intake and exhaust systems of the train.

2.2.1 Wind tunnel Size Influence

The side walls of the wind tunnel affect the wake, bending it towards the outlet of the wind tunnel test section, and thus, changing the aerodynamic coefficients (see Figure 27). To study the influence of the wind tunnel size, the width of Domain B was increased by 3 and 5 times, resulting in Domain B' and B", respectively. Domain B' and B" retained the same boundary conditions as Domain B.

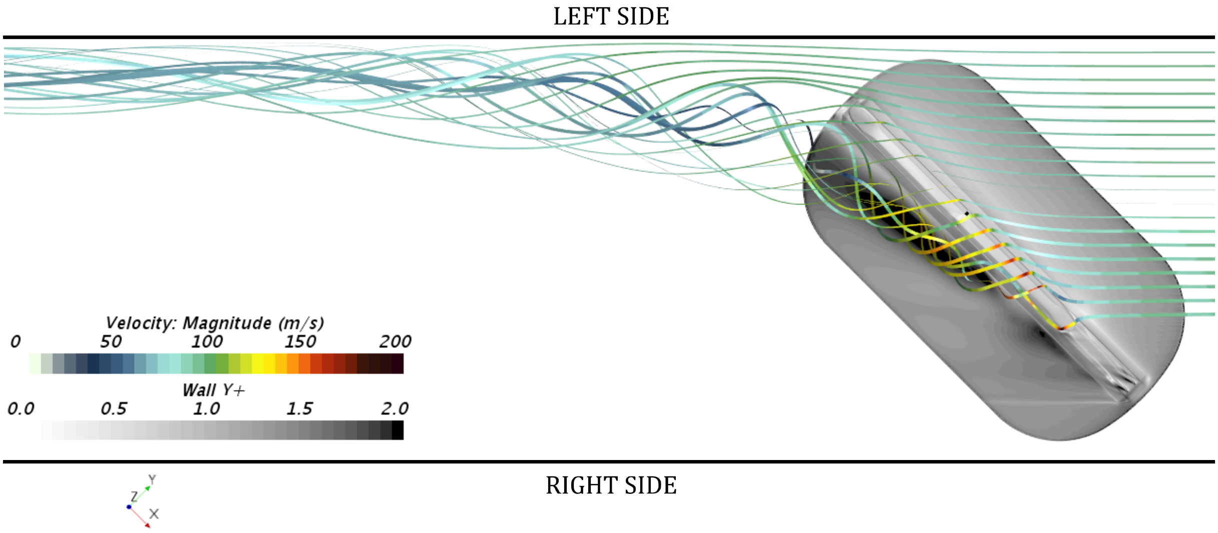

Figure 27 – Influence of the wind tunnel size on the wake behavior. The proximity of the left-wall affects the wake, thus the aerodynamic coefficients. The flow is from right to left.

Domain B' and B" were meshed using the same parameters as Mesh V, but with coarse cells added in the areas of extended width. The use of coarse cells in the extended regions minimize the increase in the cell number, in comparison with Domain B. The characteristics of each domain is presented in Table 5.

As the difference in the aerodynamic coefficients computed for Domain B' and B" is ±1% (see Section 3.2.1), the dimensions of Domain B' were selected to carry on the following studies.

Domain	**Dimensions (H x W x L)**	**Symmetry Plane**	**Cells x10^6**
Domain B	0.9 H x 1.0 W x 1.0 L	yes	160
Domain B'	0.9 H x 3.0 W x 1.0 L	yes	165
Domain B"	0.9 H x 5.0 W x 1.0 L	yes	170

Table 5 – Characteristics of the domains for the study of the wind tunnel size influence in crosswind analysis (H = 2.4 m, W = 2.4 m, L = 10.8 m).

2.2.2 STBR Influence

In the KKK wind tunnel, a finite splitter plate and STBR were used. The tip of the STBR generates a vortex that can affect the model wake, as illustrated by Figure 28. This effect does not happen in reality, as the length of the track and rail is much larger than the train length. As the track and rail to train length ratio is large, a virtually "infinite" track and rail is considered (see Figure 29).

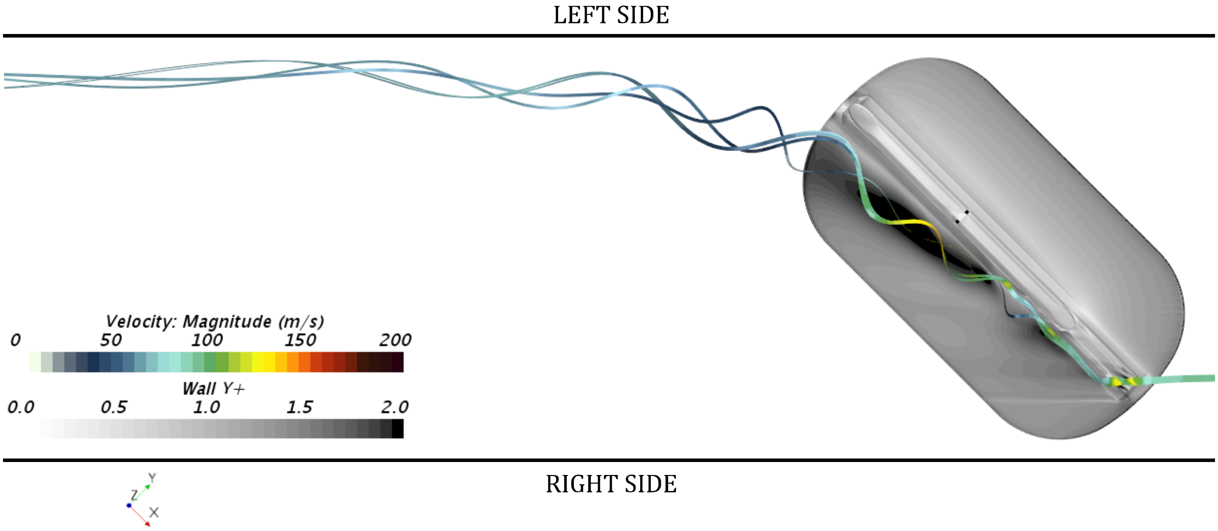

Figure 28 – Influence of the STBR tip on the wake behavior. The STBR generate a tip vortex that can affect the aerodynamic coefficients.

To study the influence of the STBR on the flow behavior both the splitter plate and the STBR had their length increased to cover the domain width. These "infinite" STBR and "infinite" splitter plate form Domain C. This domain kept the same dimensions and boundary conditions as Domain B'. The characteristics of the domains are presented in Table 6.

Domain	**Dimensions (H x W x L)**	**Symmetry Plane**	**Cells x10^6**
Domain B’	0.9 H x 3.0 W x 1.0 L	yes	165
Domain C	0.9 H x 3.0 W x 1.0 L	yes	180

Table 6 – Characteristics of the domains for the study of the STBR geometry influence in crosswind analysis (H = 2.4 m, W = 2.4 m, L = 10.8 m).

The mesh at the infinite STBR and Splitter Plate is shown in Figure 29. The parameters used in Mesh V were kept, except in the extended STBR where the prism layer number was reduced to four layers and its total thickness increased and the surface sizing by a factor of 2, resulting in a slight increase in the cell number for the total mesh (see Table 6). In Figure 29, the difference in the meshes for the original and extended STBR is shown.

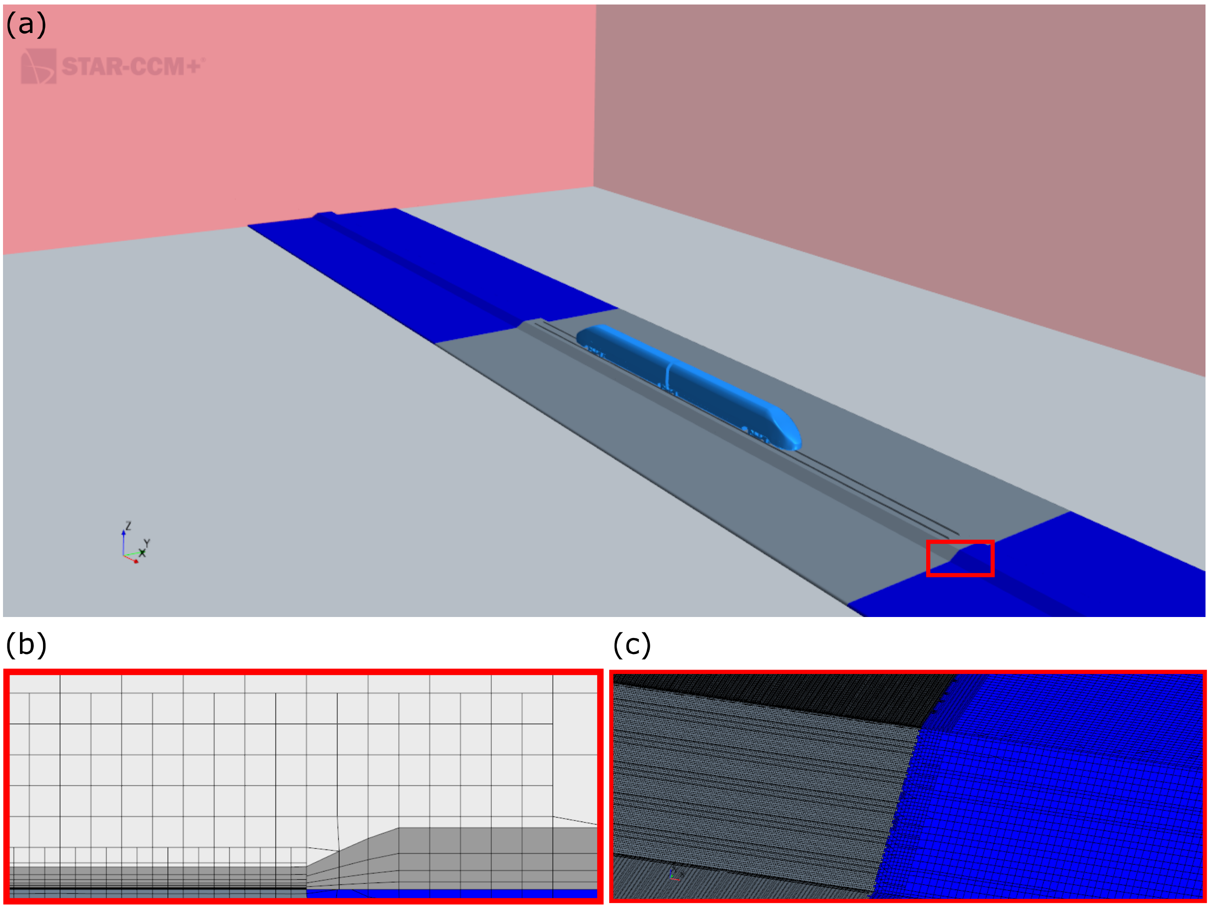

Figure 29 – Visualization of the mesh in the infinite STBR and Splitter Plate. (a) The infinite STBR with the original geometry (gray) and the extended geometry (blue). (b) The difference in both size and prism layer. The prism layer total thickness was increased by 2 times and the number of layers reduced to four. (c) The mesh in the original and extended STBR, showing the different in the sizing.

2.2.3 Moving Model Influence

To study the effects of a moving model, the side wind V_w was fixed perpendicular to the train axis, as shown in Figure 30. The relative wind velocity V_a is kept at 90 m/s, and the wind angle ψ kept at 90°, while both train and inlet velocities, V_{tr} and V_w, are calculated with respect to the desired yaw angle β.

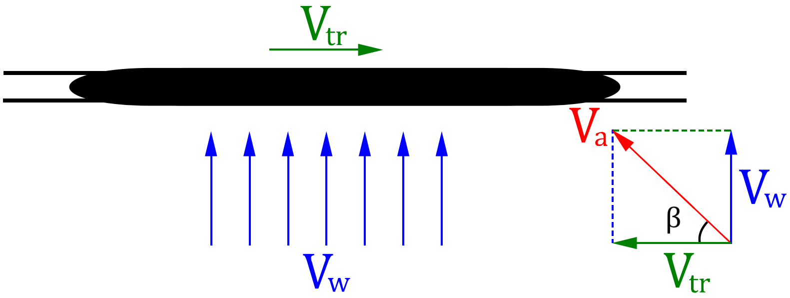

Figure 30 – Schematic representation of velocity vectors for a crosswind condition modeled for the study of the effects of a moving model. Where V_w is the wind velocity, V_{tr} the train velocity, V_a the relative velocity and β the yaw angle.

As the simulations are steady, the motion of the train was modeled with a moving reference frame. A translational frame was applied for the rail-cars and a translational and rotational frame applied for each wheel. Both train and the infinite STBR are repositioned, with a 10 h clearance ahead of the model and 25 h aft the model, where h is the model height. This domain is referred as Domain D, and is shown in Figure 31. The changes in the model did not affect the cells number, retaining the same size as Domain C.

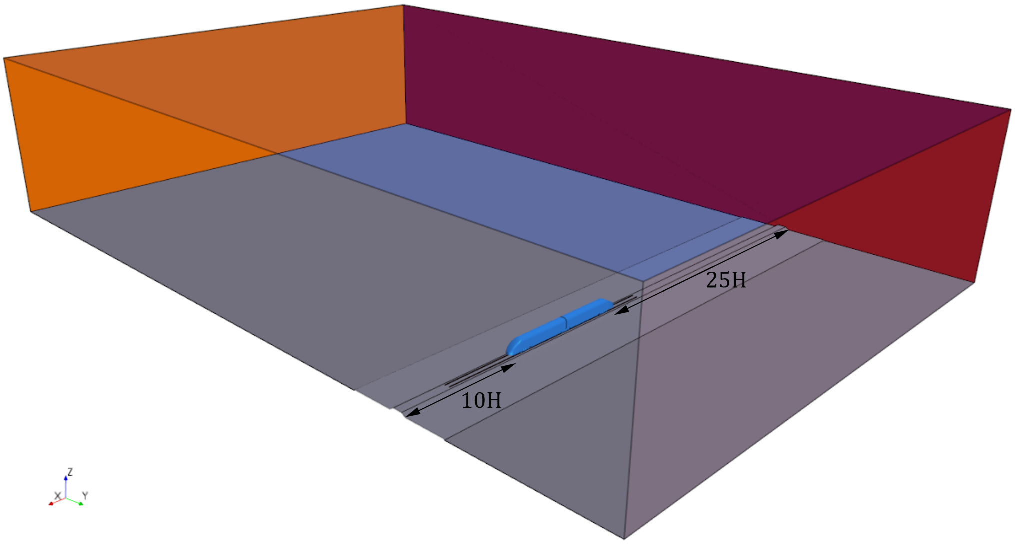

Figure 31 – Computational domain for moving model analysis ($c.f.$ Domain D). The train positioned to have a 10 h clearance ahead and 25 h aft the model.

To analyze the flow behavior in a different Reynolds number, the model was scaled up to its real size. The relative wind velocity was kept at 90 m/s, resulting in a Reynolds number of $1.75 \cdot 10^7$. The full-scale domain is referred as Domain E. The dimensionless wall-distance y+ was kept below 3 by increasing the number of prism layers to 15 on the train surface. The characteristics of Domain D and E are presented in Table 7.

Domain	**Dimensions (H x W x L)**	**Prism Layer Thickness**	**Prism Layer Number**	**Cells x10^6**
Domain D	0.9 H x 3.0 W x 1.0 L	0.8 mm	12	180
Domain E	0.9 H x 3.0 W x 1.0 L	20.0 mm	15	190

Table 7 – Characteristics of the domains for the study of the moving model influence in crosswind analysis (H = 2.4 m, W = 2.4 m, L = 10.8 m).

The boundary conditions for Domain D and E are presented in Table 8.

Surface	**Boundary Condition**	**Value**
$1/25^{th}$ EC250	Moving Frame	$V_r \cdot cos(\beta)$
STBR	Wall	No-slip
Splitter Plate	Wall	No-slip
Roof	Symmetry	-
Floor	Wall	No-slip
Left Side	Tangential Velocity-inlet	$V_r \cdot sin(\beta)$
Right Side	Tangential Velocity-inlet	$V_r \cdot sin(\beta)$
Inlet	Velocity-inlet	$V_r \cdot sin(\beta)$
Outlet	Pressure-outlet	0 Pa

Table 8 – Boundary conditions applied in Domain D for the analysis of moving model effects. $V_r = 90$ m/s.

2.2.4 Air Intake & Exhaust Influence

To study the influence of the air intake and exhaust of the train Domain E' was used, which has the same characteristics as Domain E, except for the inlets and outlets of the train which are modeled (Figure 32).

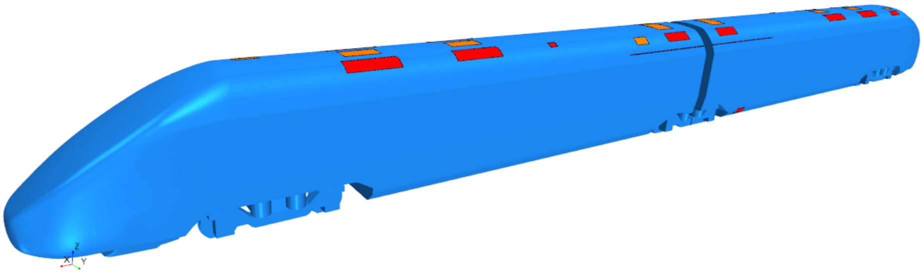

Figure 32 – Modeling of the air intake and exhaust of the full-scale EC250 high-speed train. Intake inlets identified in red, exhaust outlets in orange.

In total, 10 air intake inlets and 5 exhaust outlets were modeled for the leading car, and 11 inlets and 5 outlets for the trailing car. Each intake inlet and exhaust outlet can be identified in Figure 33, for the leading and trailing cars. For each one of them the mass flow rate and temperature were set to the operational values of Stadler EC250, as presented in Table 9.

Location	**Position**	**Boundary**	**Mass Flow Rate [kg/s]**	**Temperature [K]**
Leading Car	1	Mass Flow Inlet	−0.92	300.00
	2	Mass Flow Outlet	+0.92	320.35
	3	Mass Flow Inlet	−0.72	300.00
	4	Mass Flow Outlet	+1.44	403.85
	5	Mass Flow Inlet	−0.72	300.00
	6	Mass Flow Inlet	−0.72	300.00
	7	Mass Flow Outlet	+1.44	403.85
	8	Mass Flow Inlet	−0.72	300.00
	9	Mass Flow Outlet	+1.44	403.85
	10	Mass Flow Inlet	−0.18	300.00
	11	Mass Flow Outlet	+0.49	303.15
	12	Mass Flow Inlet	−0.18	300.00
	13	Mass Flow Inlet	−2.00	300.00
	14	Mass Flow Outlet	+4.01	320.65
	15	Mass Flow Inlet	−2.00	300.00
Trailing Car	16	Mass Flow Inlet	−2.00	300.00
	17	Mass Flow Outlet	+4.01	320.65
	18	Mass Flow Inlet	−2.00	300.00
	19	Mass Flow Inlet	−0.18	300.00
	20	Mass Flow Outlet	+0.49	303.15
	21	Mass Flow Inlet	−0.18	300.00
	22	Mass Flow Inlet	−0.21	300.00
	23	Mass Flow Inlet	−0.72	300.00
	24	Mass Flow Outlet	+1.44	403.85
	25	Mass Flow Inlet	−0.72	300.00
	26	Mass Flow Inlet	−0.72	300.00
	27	Mass Flow Outlet	+1.44	403.85
	28	Mass Flow Inlet	−0.72	300.00
	29	Mass Flow Outlet	+0.92	320.35
	30	Mass Flow Inlet	−0.92	300.00
	31	Mass Flow Inlet	−0.67	300.00

Table 9 – Operational characteristics for the intake inlets and exhaust outlets of the full-scale Stadler EC250 high-speed train, the locations of each boundary is presented in Figure 33.

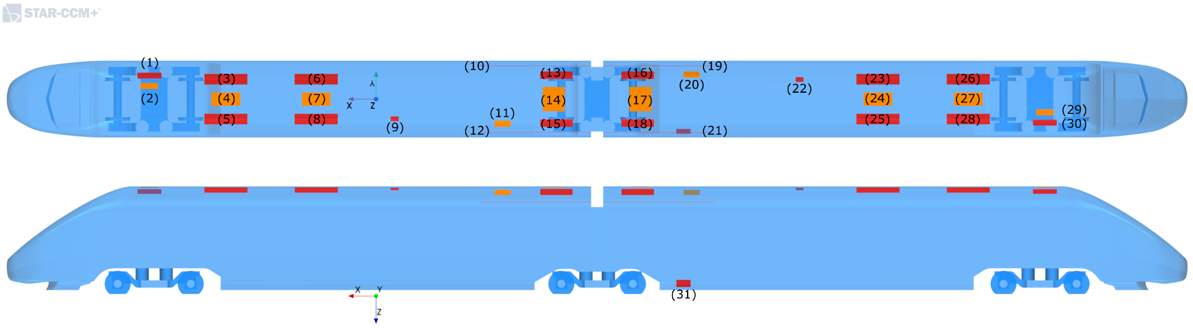

Figure 33 – Indication of the air intake inlets (red) and exhaust outlets (orange) position in the full-scale EC250 high-speed train.

2.3 Summary

A total of eight domains were generated. Domain A and B were used to validate the simulation results. For the validation six turbulence models were tested on five meshes. Domain B, B' and B" were used to study the effects of the wind tunnel size, C the STBR geometry, D and E the moving model and E' the air intake and exhaust on the flow behavior. Table 10 summarizes the information concerning each computational domain and its respective study phase.

Domain	**Phase**	**Dimensions (H x W x L)**	**Mesh**	**Cells x10^6**
Domain A	Validation	1.0 H x 1.0 W x 1.0 L	I II III	100 150 160
Domain B	Validation	0.9 H x 1.0 W x 1.0 L	III IV V	130 140 160
Domain B'	Wind tunnel size	0.9 H x 3.0 W x 1.0 L	V	165
Domain B"	Wind tunnel size	0.9 H x 5.0 W x 1.0 L	V	170
Domain C	STBR configuration	0.9 H x 3.0 W x 1.0 L	V	180
Domain D	Moving model	0.9 H x 3.0 W x 1.0 L	V	180
Domain E*	Moving model	0.9 H x 3.0 W x 1.0 L	V	190
Domain E'*	Air intake & exhaust	0.9 H x 3.0 W x 1.0 L	V	190

Table 10 – Characteristics of the computational domains used in this research (H = 2.4 m, W = 2.4 m, L = 10.8 m). The domains indicated by "*" are in full-scale.

3 Results

Like Chapter 2, this chapter is divided in two sections. Section 3.1 presents the validation results while Section 3.2 analyzes the influence of the different parameters.

3.1 Validation

The validation results are presented in the following sections. The analysis of the computational mesh is presented in Section 3.1.1 and the study of the turbulence models in Section 3.1.2. To reduce the length of this thesis, most of the results presented are for a yaw angle $\beta = 45°$, but the choices of mesh configuration and turbulence model were based on the results from $\beta = 5°$ to $50°$.

3.1.1 Mesh Analysis

The results accuracy depends on the mesh quality. Five meshes with an increasing number of cells were tested during the validation phase. The mesh parameters are given in Table 3 and 4. The side force C^*_{fy}, lift C^*_{fz}, rolling moment C^*_{Mx} and lee-rail moment $C^*_{Mx,\mathrm{lee}}$ coefficients for Mesh I to III, Domain A, with the SST turbulence model are displayed in Figure 34, where the results tend to overestimate the wind tunnel results.

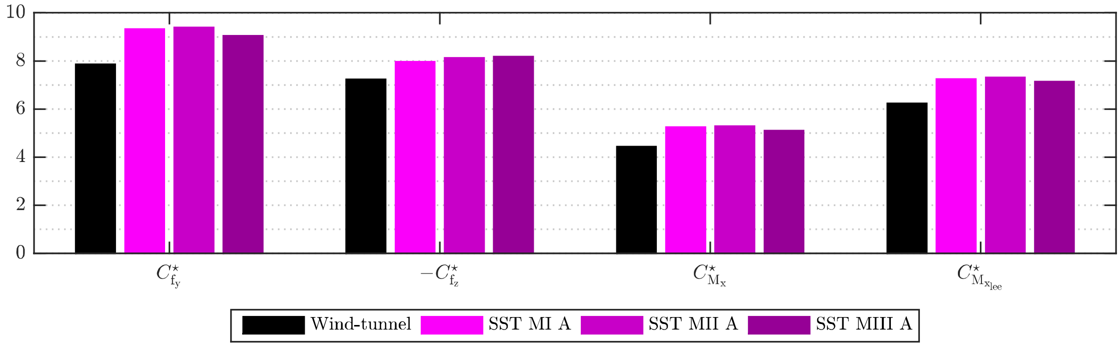

Figure 34 – Comparison of the simulation results for the SST model with respect to wind tunnel, yaw angle $\beta = 45°$. Mesh I to III, Domain A.

The three meshes give similar results, but their influence on the flow field is shown in Figure 35. The flow fields from Mesh I, II and III show strong gradients close to the train, the under-body and lee-side wake regions. Refining the mesh renders a more detailed flow field, as shown by the vorticity fields in Figure 35. The separation occurs at the lee-ward roof corner and a vortex is generated, which at 45° is similar to the slender body flow structure. Although there is a difference in the vorticity intensity in the lee-ward vortex, the vortices position is similar.

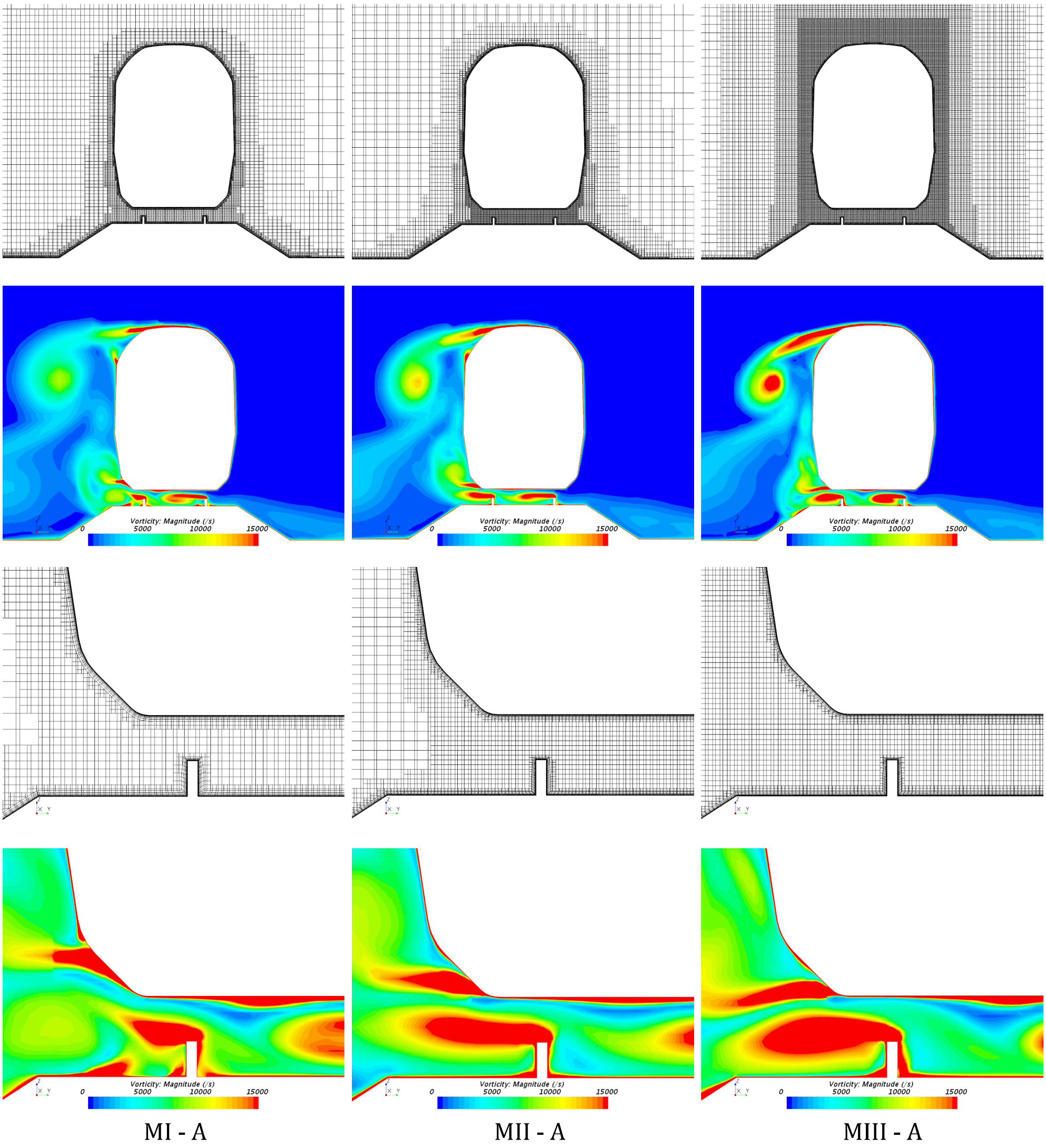

MI - A MII - A MIII - A

Figure 35 – Analysis of the vorticity field for Mesh I, II and III, Domain A. Results obtained with the SST turbulence model. *Plane I*, located 200 *mm* ahead of the measuring coordinate system, or 356 *mm* aft the nose of the leading-car.

Mesh III presents better results compared to Mesh I and II but has longer CPU time. To reduce the CPU time, the use of a symmetry plane in Domain B led to a 20% reduction in the mesh cells while producing a difference of approximately 1% for the aerodynamic coefficients (see Figure 36) in comparison with Domain A. This 20% reduction in cells number reduced the CPU time by 15%.

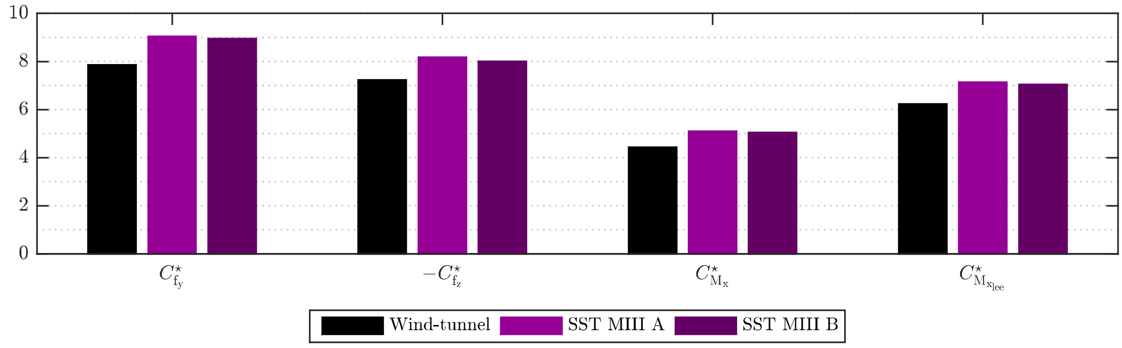

Figure 36 – Comparison of the simulation results for SST model with respect to wind tunnel, yaw angle $\beta = 45°$. Mesh III, Domain A and B.

The vorticity and pressure fields, at Plane I, located 356 *mm* aft the nose of the leading-car, is presented in Figure 37 for Domain A and B. As the flow fields and the aerodynamic coefficients are similar for both Domain A and B, we chose to carry on the simulations with Domain B.

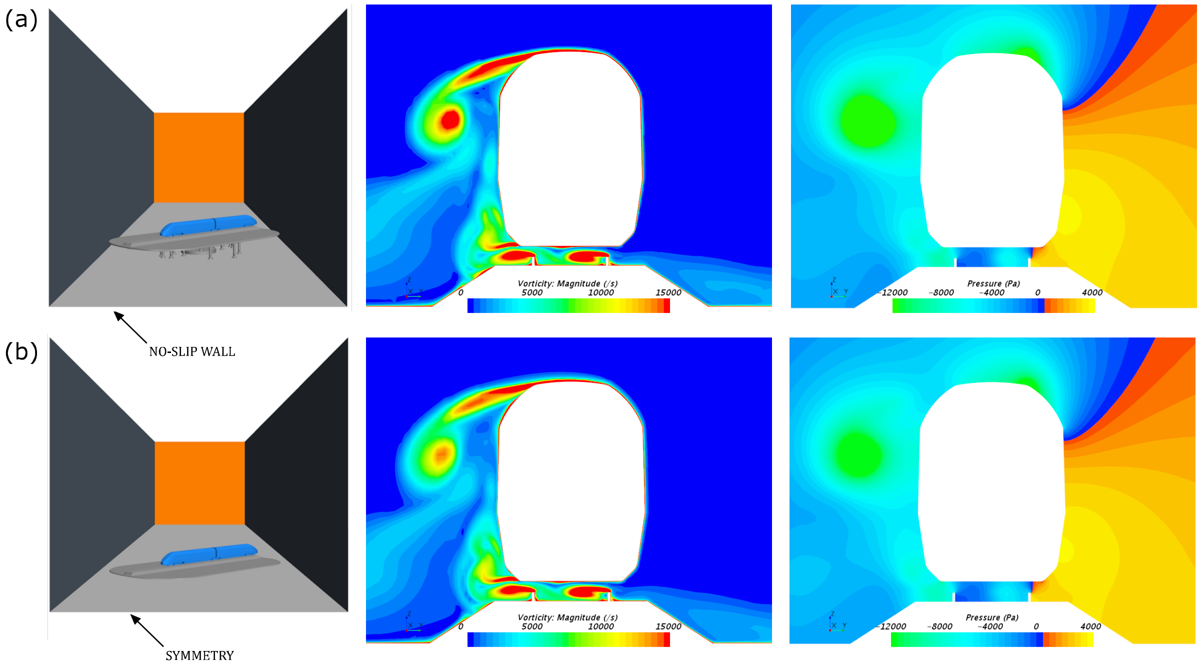

Figure 37 – Analysis of the vorticity and pressure fields for Mesh III, (a) Domain A and (b) Domain B. Results obtained with the SST model. *Plane I*, located 200 *mm* ahead of the measuring coordinate system, or 356 *mm* aft the nose of the leading-car.

Mesh III was further refined for Domain B in the train lee-side (VC2) and under-body regions (VC4), where strong gradients were observed. Mesh IV refined the lee-side region and slightly improved the prediction of the side force and moment coefficients (see Figure 38). Mesh V refined both train lee-side and under-body regions (see Figure 38). The results were produced with the SST $\gamma - \mathrm{Re}_{\theta}$ turbulence model.

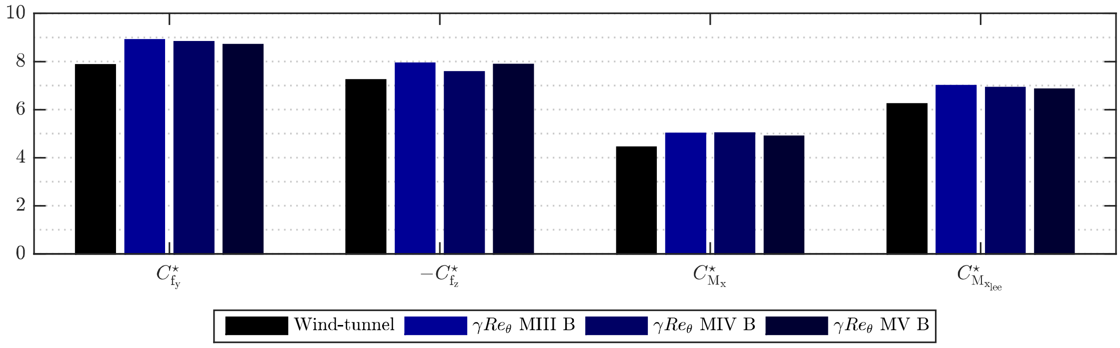

Figure 38 – Comparison of the simulation results for SST $\gamma - \mathrm{Re}_\theta$ model with respect to wind tunnel, yaw angle $\beta = 45°$. Mesh III to V, Domain B.

The best results were achieved with Mesh V, which was the finer mesh. The vorticity and pressure fields for Mesh III to V are illustrated in Figure 39. The pressure and vorticity fields show a similar behavior, where the position of the lee-ward vortex is identical. The side force and rolling moment coefficients are more sensitive to the mesh refinement, the lift coefficient shows only a small difference for a yaw angle $\beta = 45°$.

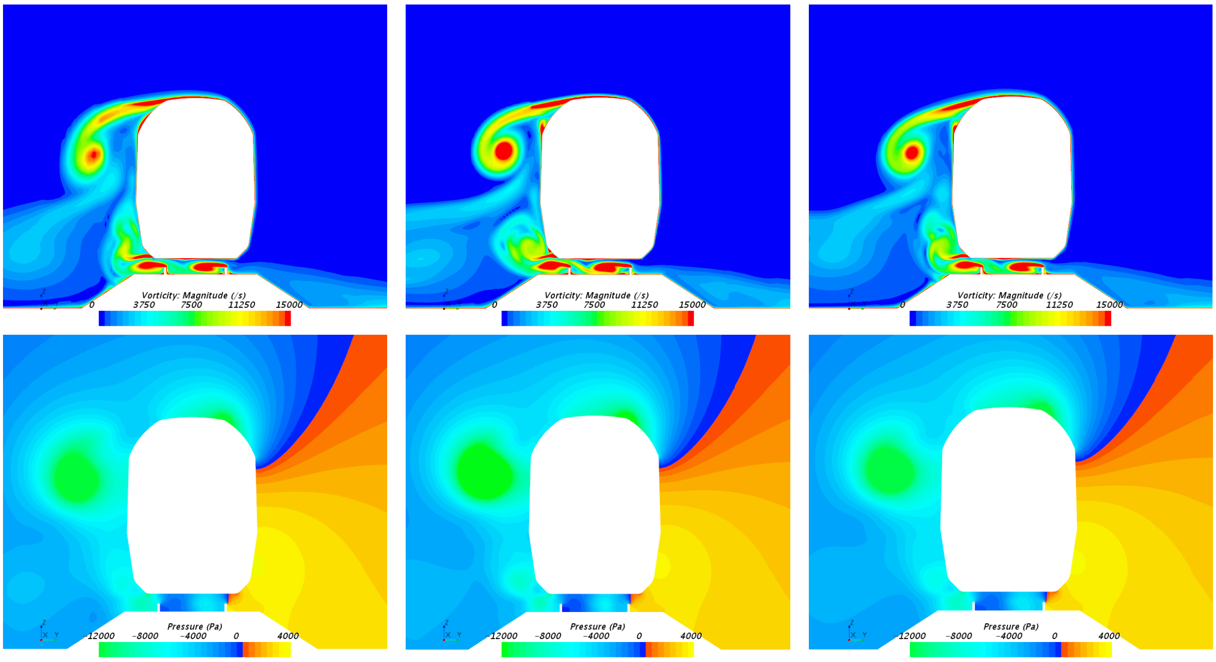

(a) (b) (c)

Figure 39 – Analysis of the vorticity and pressure fields for Mesh III to V, Domain B. Results obtained with the SST $\gamma - \mathrm{Re}_\theta$ model. *Plane I*, located 200 mm ahead of the measuring coordinate system, or 356 mm aft the nose of the leading-car.

The results from Mesh III to V for yaw angles from 25° to 50° are summarized in Figure 40. Although the mesh refinement produces better results, the differences between the results from Mesh III to V are small. The results can be considered mesh independent.

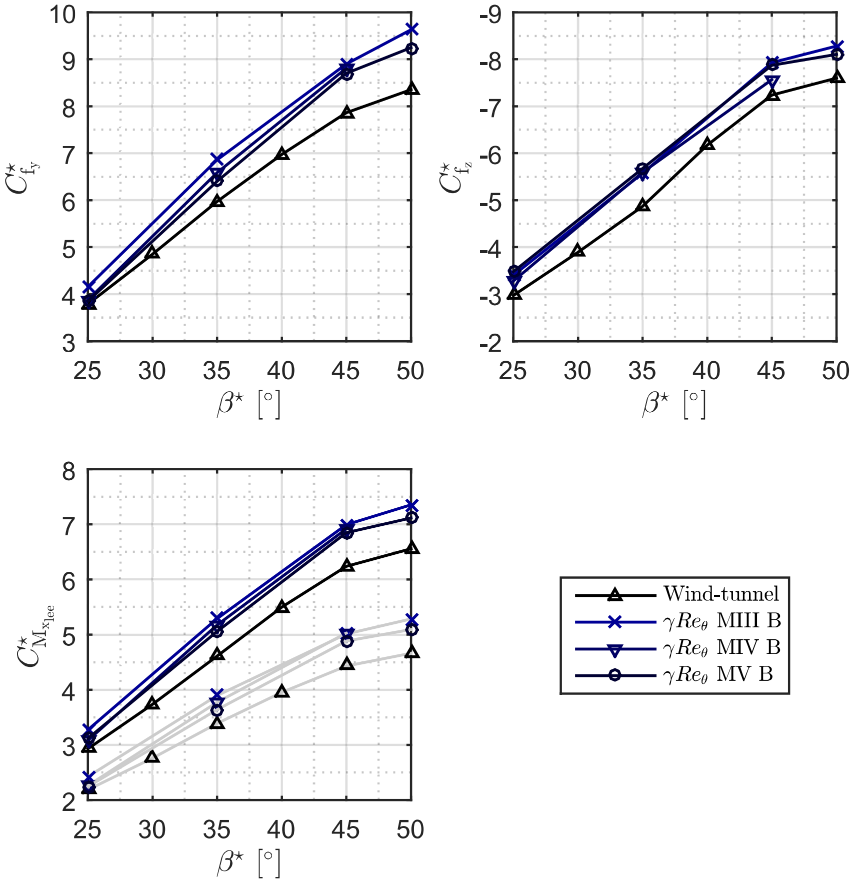

Figure 40 – Analysis of the side force, lift, rolling moment (gray line) and lee-rail moment coefficients for Mesh III to V, Domain B, SST $\gamma - \text{Re}_\theta$ model. Analysis for C_{f_y}, C_{f_z} and $C^*_{M_{x,\text{lee}}}$, $C^*_{M_x}$ in gray.

3.1.2 Turbulence Model Analysis

The results obtained from the different turbulence models are presented in this section. The turbulence model validation was performed on Mesh I (Domain A), III and IV (Domain B).

The Realizable $k - \varepsilon$ and SST turbulence models were tested on Mesh I, Domain A, as seen in Figure 41. There is good agreement for yaw angles from 5° to 25°, however, at higher yaw angles the differences between wind tunnel and simulations increase.

The RSM and SST $\gamma - \text{Re}_\theta$ result in the best predictions over the different $k - \varepsilon$ models as shown in Figure 42 for Mesh III and in 43 for Mesh IV. There are differences for the forces coefficients, as seen in Figure 42 and Figure 43, even if they result in similar moment coefficients. An increase of the side force is followed by a decrease of the lift force coefficient, and vice-versa, resulting in a close rolling and lee-rail moment coefficients for all the models, as also reported by Diedrichs (2008).

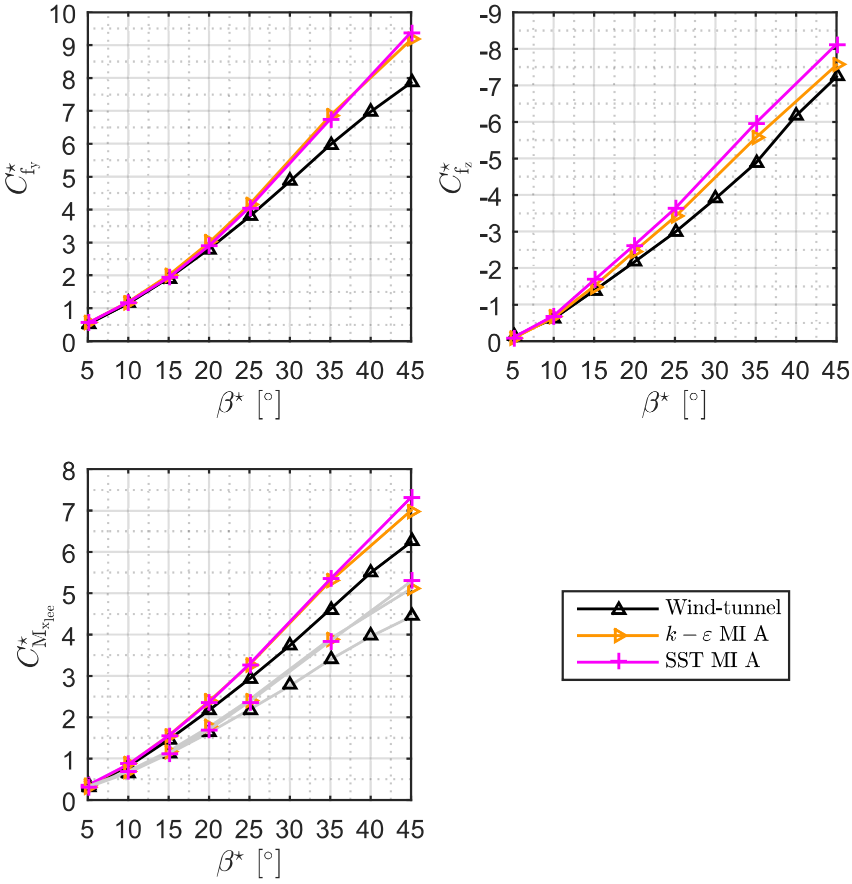

Figure 41 – Comparison of the simulation results for the Realizable $k-\varepsilon$ and SST turbulence models with respect to wind tunnel. Mesh I, Domain A. Analysis for C_{f_y}, C_{f_z} and $C^*_{M_{x,\mathrm{lee}}}$, $C^*_{M_x}$ in gray.

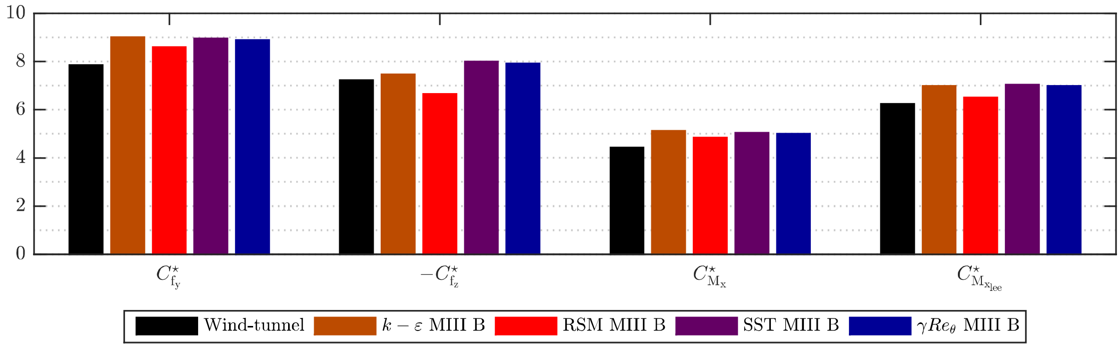

Figure 42 – Comparison of the simulation results for the different turbulence models with respect to wind tunnel, yaw angle $\beta = 45°$. Mesh III, Domain B.

The RSM model predicts well the side force and moment coefficients but underestimates the lift coefficient by a larger extent than the other models. Although the SST $\gamma-\mathrm{Re}_\theta$ model overestimates the aerodynamic coefficients, its deviation is less than the SST and the $k-\varepsilon$ class models. The SST $\gamma-\mathrm{Re}_\theta$ model presents the smallest deviation from the average results of each aerodynamic coefficient, as observed in Figure 42 and Figure 43.

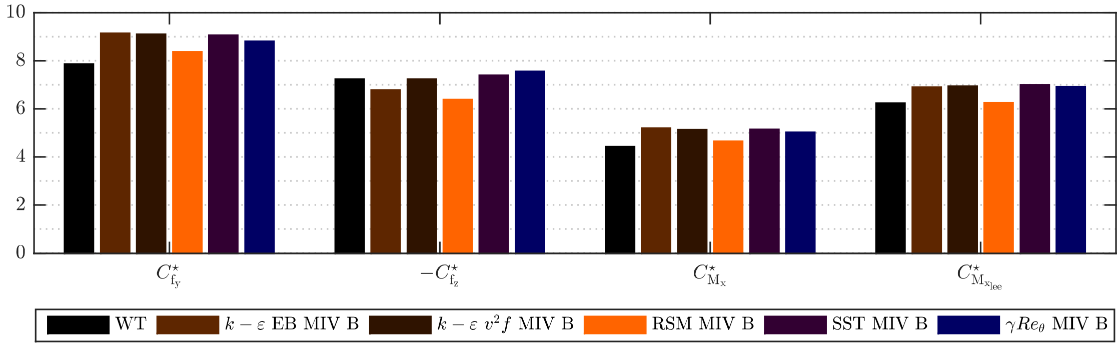

Figure 43 – Comparison of the simulation results for the different turbulence models with respect to wind tunnel, yaw angle $\beta = 45°$. Mesh IV, Domain B.

The difference between the RSM and SST $\gamma - \mathrm{Re}_{\theta}$ turbulence models is shown in Figure 44 by the vorticity and pressure fields at Plane I, located 356 *mm* aft the nose of the leading-car. There are no major differences on the wind-ward side and under-body regions, however, the wake in the lee-ward side is larger and less intense for the RSM model. The RSM pressure distribution is smaller compared to the SST $\gamma - \mathrm{Re}_{\theta}$ model for both lee-ward and roof regions, which leads to a smaller side and lift coefficients.

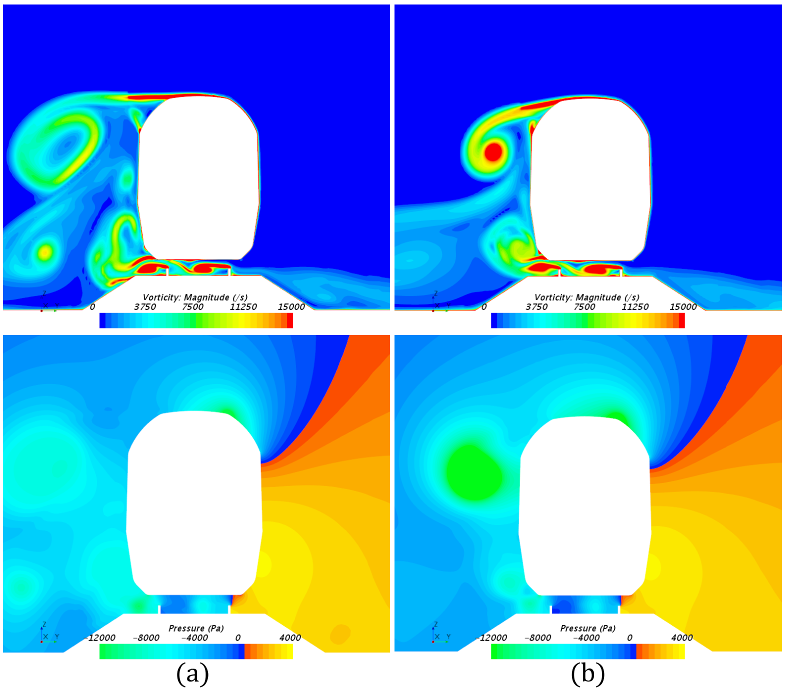

(a) (b)

Figure 44 – Analysis of the vorticity and pressure fields for Mesh IV, Domain B. Results obtained with the (a) RSM and (b) SST $\gamma - \mathrm{Re}_{\theta}$ turbulence models. *Plane I*.

As seen, both the RSM and SST $\gamma - \mathrm{Re}_{\theta}$ turbulence model displayed better overall performances than the other turbulence models. However, the RSM model requires larger

CPU time compared to the SST $\gamma - \mathrm{Re}_\theta$ model as it is a seven-equation model. We chose the SST $\gamma - \mathrm{Re}_\theta$ turbulence model, Mesh V, Domain B to carry on the parametric studies presented in Section 3.2. Figure 45 summarizes the validation results by comparing the SST $\gamma - \mathrm{Re}_\theta$ and the wind tunnel results at all yaw angles.

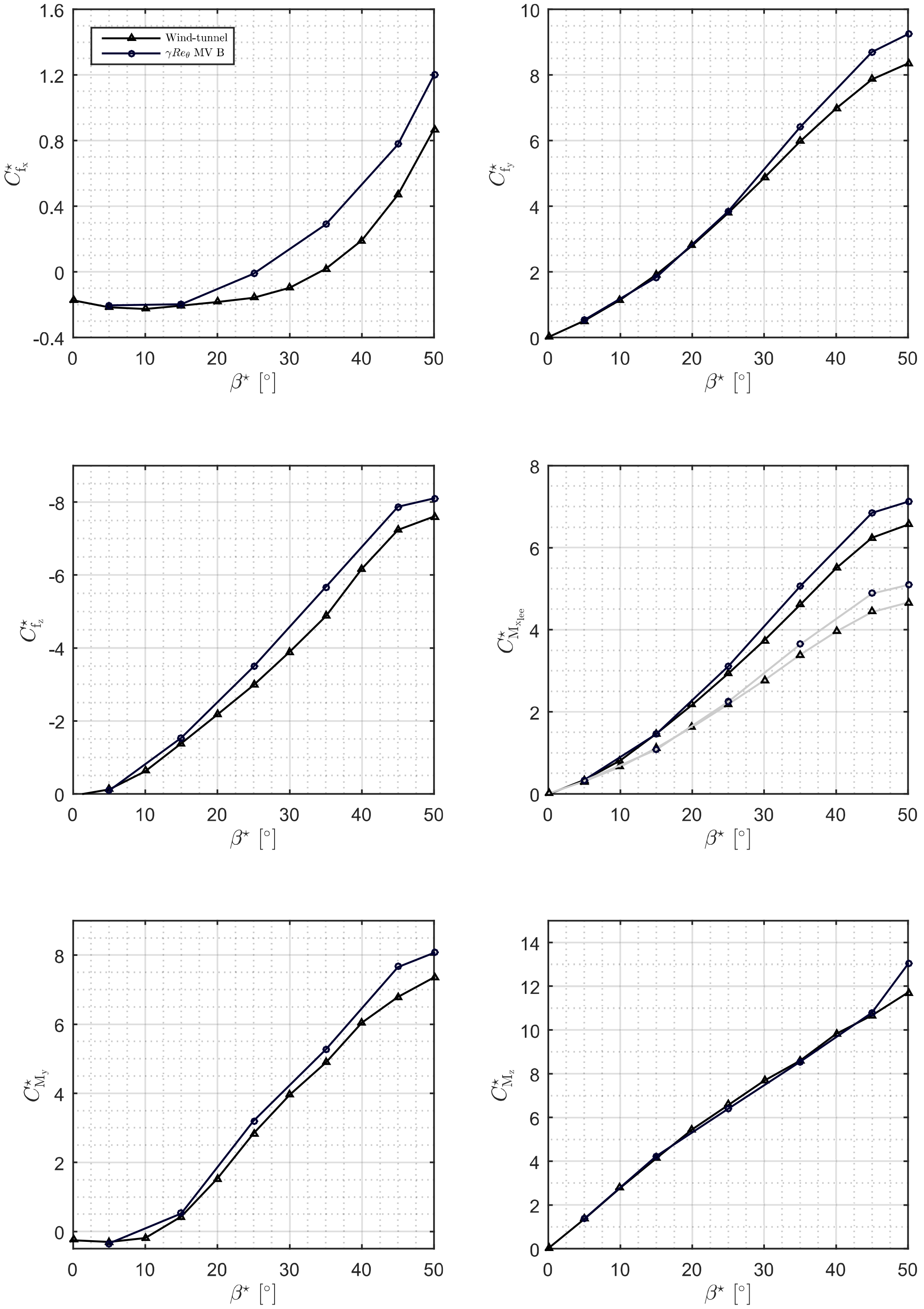

Figure 45 – Validation results for the aerodynamic coefficients from $\beta = 0°$ to $\beta = 50°$, from Mesh V, Domain B for the SST $\gamma - \mathrm{Re}_\theta$ turbulence model.

The comparison between the simulation results with the SST $\gamma - \mathrm{Re}_\theta$ model and the KKK wind tunnel results, obtained with Particle Image Velocimetry (PIV), is given in Figure 46 and Figure 47, comparing the vector field colored with the $\lambda - 2$ criterion for both cases. There is fair agreement between the simulation and wind tunnel analysis, as the position of the wake vortex is similar for both cases. At lower yaw angles (Figure 46) both the vortex position and strength are in agreement between the simulation and the wind tunnel experiments. This is in accordance with what is found for the aerodynamic coefficients for these yaw angles (see Figure 45). However, at higher yaw angles we can see that the simulation renders a stronger vortex (Figure 47), leading to the over-prediction of the aerodynamic coefficients.

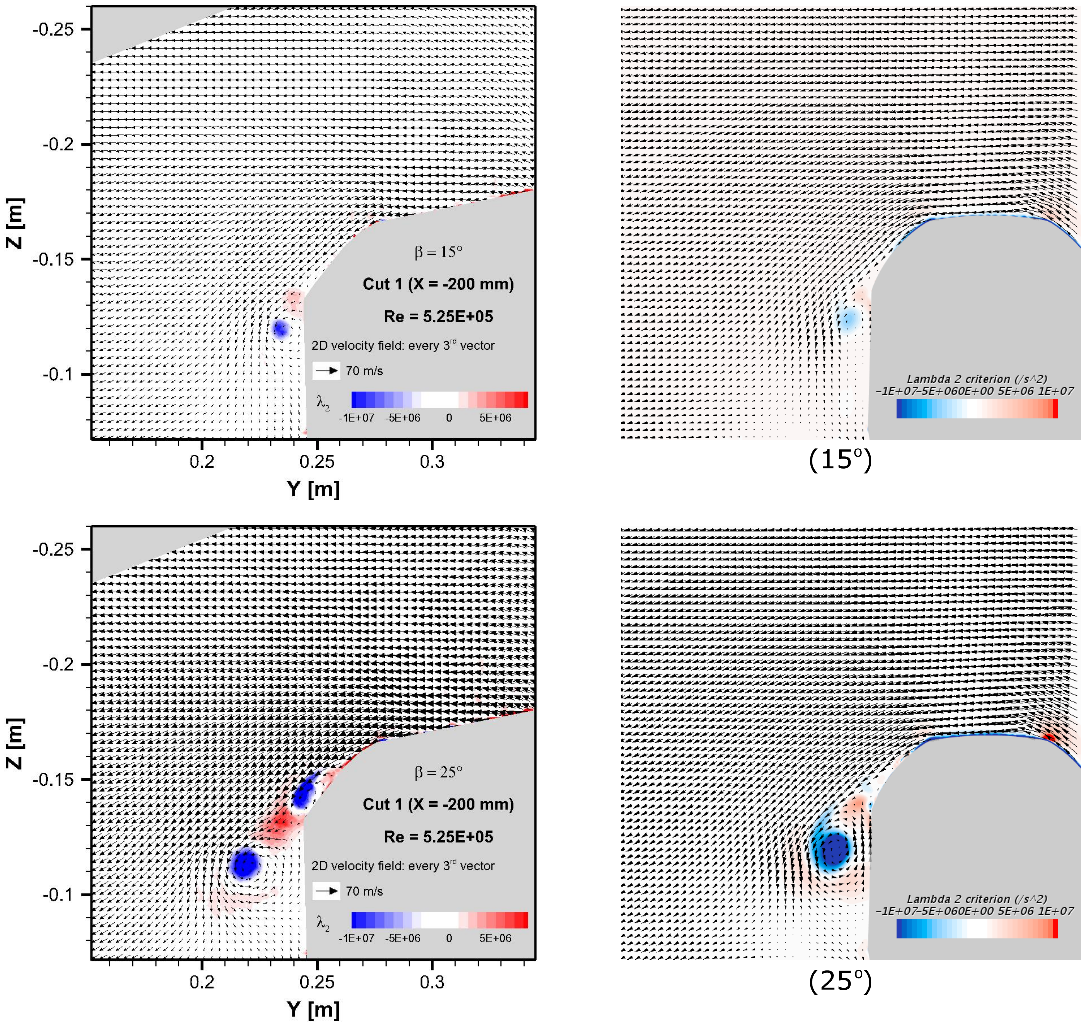

Figure 46 – Comparison between the simulation results from Mesh V, Domain B, SST $\gamma - \mathrm{Re}_\theta$ turbulence model, with respect to the KKK wind tunnel results for yaw angles $\beta = 15°$ and $\beta = 25°$. Vector field colored with the $\lambda - 2$ criterion. Evaluation made for *Plane I*.

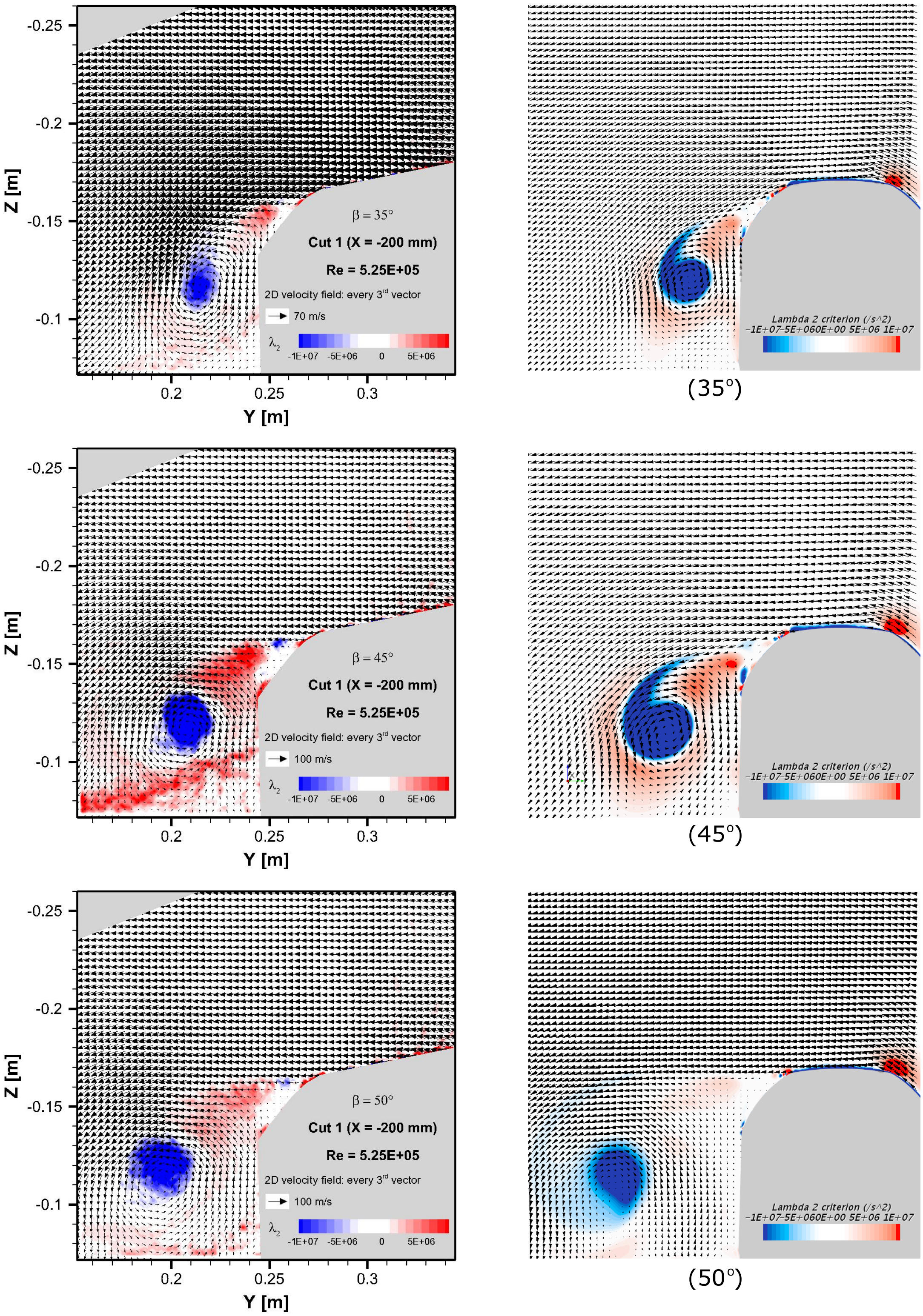

Figure 47 – Comparison between the simulation results from Mesh V, Domain B, SST $\gamma - \mathrm{Re}_\theta$ turbulence model, with respect to the KKK wind tunnel results for yaw angles $\beta = 35°$, $\beta = 45°$ and $\beta = 50°$. Vector field colored with the $\lambda - 2$ criterion at *Plane I*.

3.2 Analysis

This section presents the effects of wind tunnel size, STBR geometry, model motion and the air intake and exhaust systems on the aerodynamic coefficients. Otherwise stated, the SST $\gamma - \mathrm{Re}_\theta$ is the turbulence model chosen for this study with the Mesh V parameters.

3.2.1 Wind tunnel

The analysis of the effects of the wind tunnel size was performed using Domain B' and B", in comparison with Domain B. The EN-14607-6 norm requires that the scaled-model and STBR blockage ratio shall be less than 15% at a yaw angle $\beta = 30°$. For the tests performed at the DLR-KKK, this blockage ratio was approximately 6%. Since Domain B' and B" are 3 and 5 times wider, respectively, this yields a blockage ratio of 2% and 1.2%.

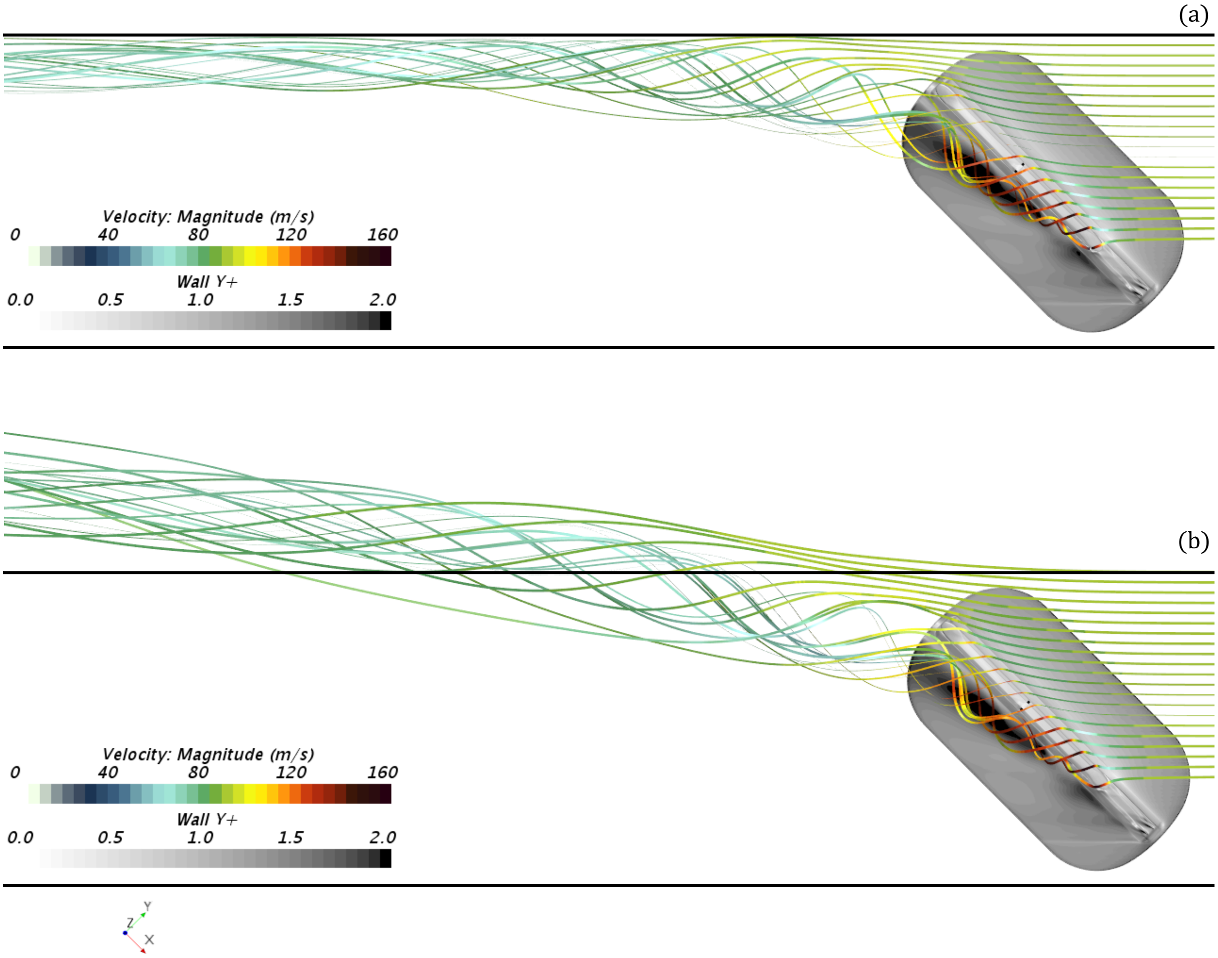

Figure 48 – Comparison of the wake behavior for (a) Domain B and (b) B' with the SST $\gamma - \mathrm{Re}_\theta$ model at $\beta = 45°$. Velocity colored streamlines and wall y+ at model surface. The flow is from right to left. The black horizontal lines retain Domain B width ($1x$).

The influence of the wind tunnel dimensions in the wake is shown in Figure 48 for $\beta = 45°$. As the wake leaves the train, it hits the left-wall due to its proximity in Domain B. In a wider wind tunnel, as Domain B', the wake grows further without being affected by the walls. The flow behavior close to the train's first car is not affected, as illustrated by the velocity streamlines. As displayed in Figure 48 and 49, the streamlines close to the train present the similar velocity and shape for both domains.

Due to the rotational behavior of the wake, after it hits the wall it tends to move upwards, as shown in Figure 49 for $\beta = 55°$. In a wider wind tunnel this effect is not present.

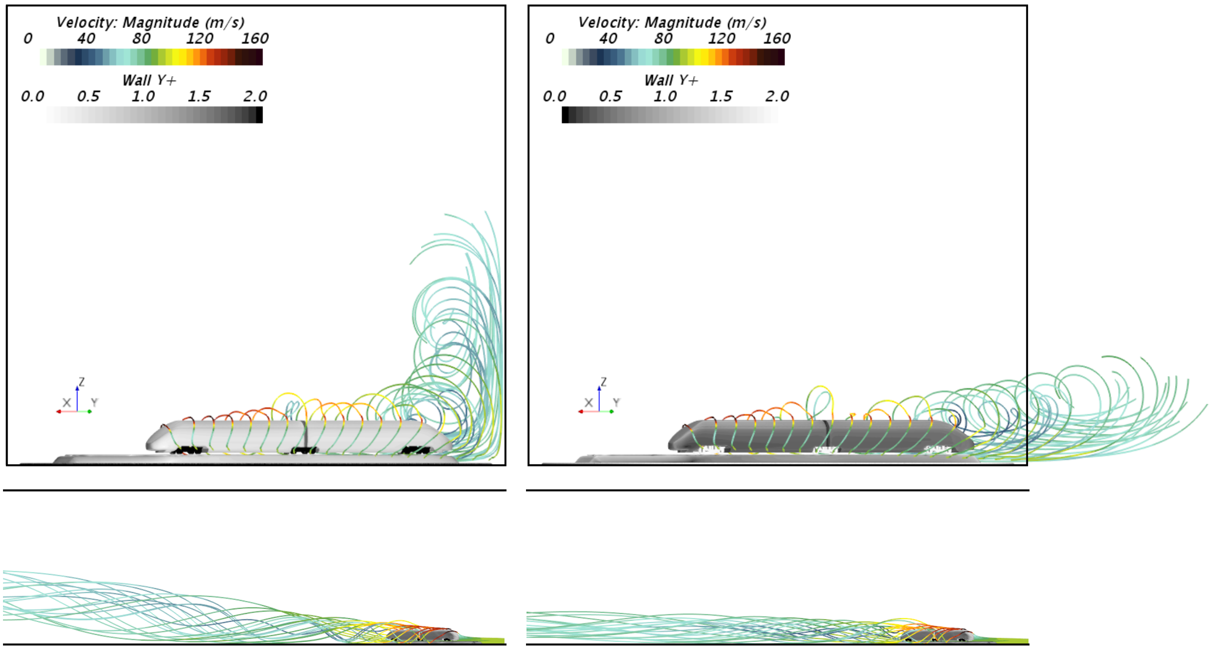

Figure 49 – Comparison of the wake behavior for (left) Domain B and (right) B' with the SST $\gamma - \mathrm{Re}_\theta$ model at $\beta = 55°$. The black box retains Domain B dimensions. The flow is entering the paper plane in the upper images and from right to left in the lower images.

Although the wind tunnel size affects the far wake, the wake region near the train's first-car is almost unaffected. Figure 50 shows that the wake behavior is similar as the pressure coefficient iso-surfaces present the same position and size. It should be noted that the wake generated by the nose detaches the train surface at almost same position that the flow separates at the lee-ward roof corner for both Domain B and B'.

The enlargement of the wind tunnel width slightly reduces the aerodynamic coefficients, as presented in Figure 51 and 52. The aerodynamic coefficients for the wind tunnel size analysis at $\beta = 45°$ are presented in Figure 51. The difference for Domain B' and B" is $\sim 2\%$ with respect to B.

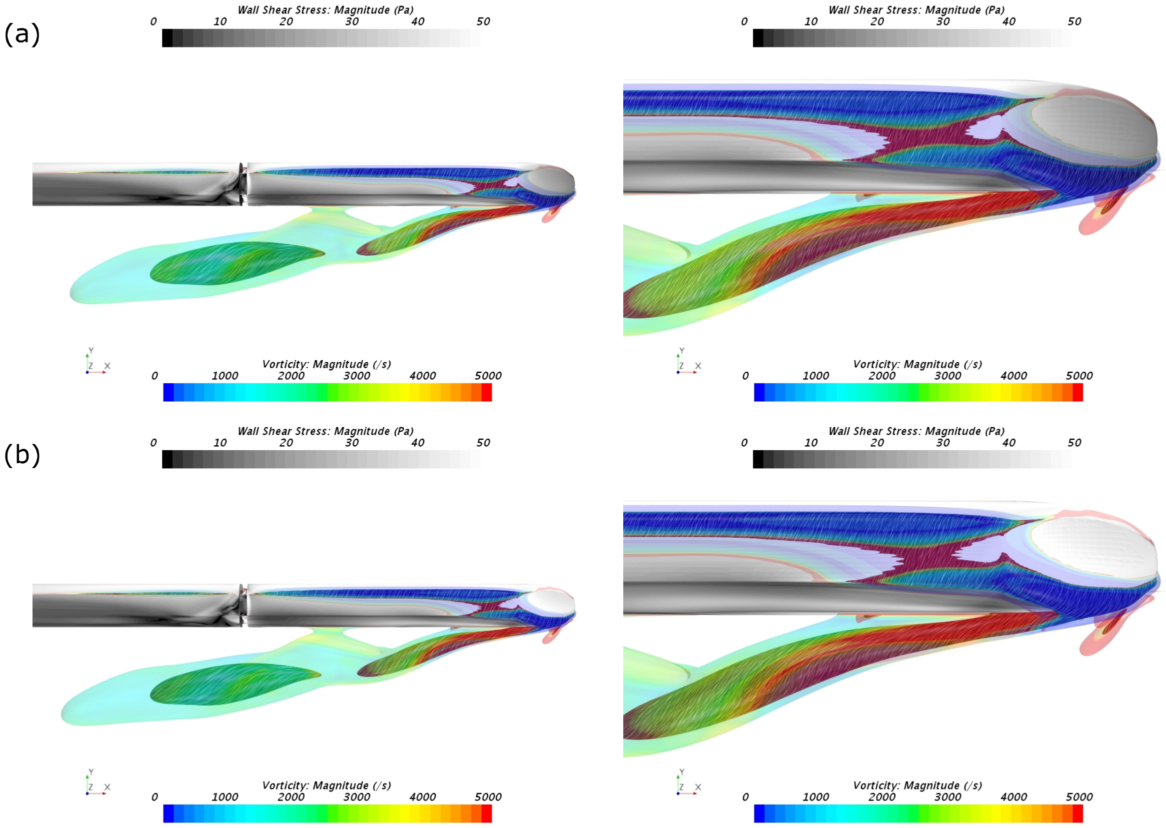

Figure 50 – Comparison of the wake behavior for Domain (a) B and (b) B’ with the SST $\gamma - \mathrm{Re}_\theta$ model at $\beta = 45°$. Vorticity colored iso-surfaces for pressure coefficients $c_p = -1.5$ (transparent) and $c_p = -2.0$ (opaque). Wall shear-stress at model surface.

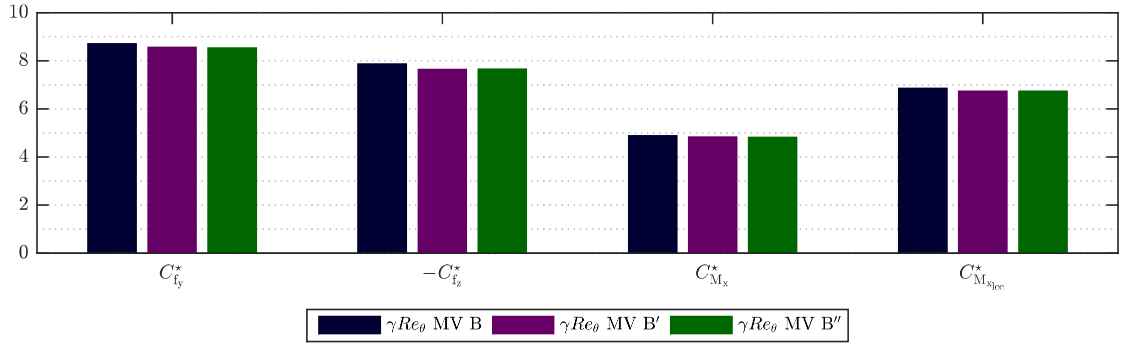

Figure 51 – Comparison of the aerodynamic coefficients for Domain B, B’ and B” at $\beta = 45°$ with the SST $\gamma - \mathrm{Re}_\theta$ turbulence model.

The results for yaw angles from $\beta = 35°$ to $\beta = 55°$ are presented in Figure 52. Increasing the wind tunnel width further than 3 times has no effect on the results. Higher deviations are found for $\beta = 55°$, with a maximum deviation of -5% for C_{f_z}. The general average deviation from the reference case Domain B is -2%, with a maximum average decrease of 4% for C_{f_z}.

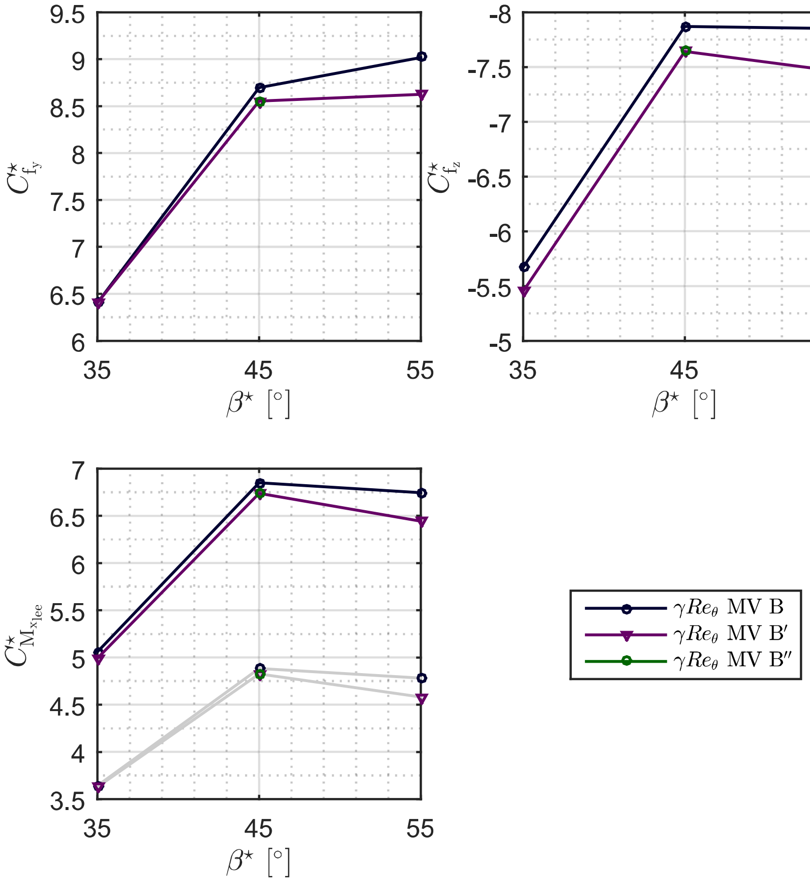

Figure 52 – Analysis of the side force, lift, rolling moment (gray line) and lee-rail moment coefficients for Domain B, B' and B", SST $\gamma - \mathrm{Re}_\theta$ model. Yaw angle $\beta = 35°$ to $\beta = 55°$. Analysis for C_{f_y}, C_{f_z} and $C^*_{M_{x,\mathrm{lee}}}$, $C^*_{M_x}$ in gray.

As no difference was found for Domain B' and B", the dimensions of Domain B' were chosen to carry on the remaining of this study.

3.2.2 STBR Geometry

The ground topography affect the wake in the lee-side of the model, as the STBR geometry also generates a vortex. To study the influence of the STBR, Domain B' and C were compared. While Domain B' keeps the standard STBR geometry, Domain C uses an infinite STBR. Increasing the STBR length avoid the formation of the tip vortex, as illustrated in Figure 53.

The absence of the STBR tip vortex reduces the lift of the model, for $\beta = 35°$ and 45°, while maintains similar values for $\beta = 55°$, as shown in Figure 54. At $\beta = 45°$ the lift C_{f_z} is reduced by $\sim 5\%$, which is the maximum deviation between Domain B' and C. Both side force and rolling moment coefficients, C_{f_y} and $C^*_{M_x}$, have minor changes ($\sim 2\%$) for all angles. The average deviation for the lee-rail moment coefficient $C^*_{M_{x,\mathrm{lee}}}$ is $\sim 2\%$.

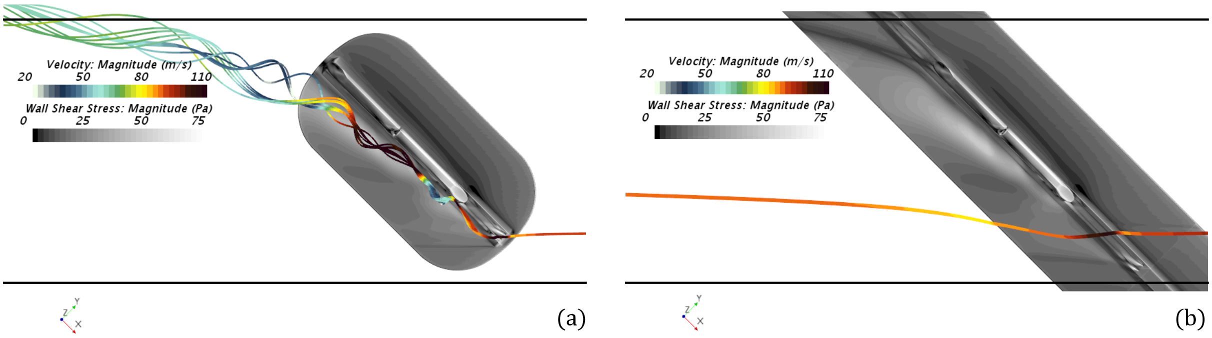

Figure 53 – Analysis of the side force, lift, rolling moment (gray line) and lee-rail moment coefficients for Domain B' and C, SST $\gamma - \mathrm{Re}_\theta$ model. Yaw angle $\beta = 35°$ to $\beta = 55°$. The horizontal lines retain Domain B width ($1x$).

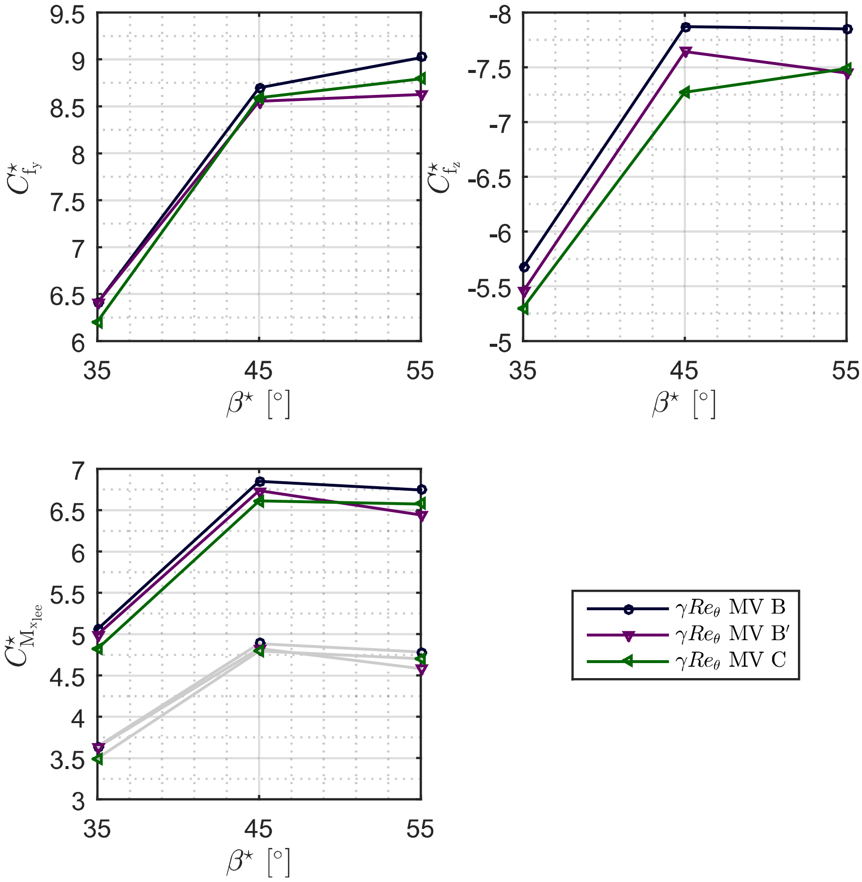

Figure 54 – Analysis of the side force, lift, rolling moment (gray line) and lee-rail moment coefficients for Domain B, B' and C, SST $\gamma - \mathrm{Re}_\theta$ model. Yaw angle $\beta = 35°$ to $\beta = 55°$. Analysis for C_{f_y}, C_{f_z} and $C^*_{M_{x,\mathrm{lee}}}$, $C^*_{M_x}$ in gray.

The comparison of the results between the reference case, Domain B, and Domain C is given in Figure 54. The lift coefficient presents the larger sensitivity comparing the DLR-KKK representation in Domain B and a domain 3 times wider with an infinite STBR, as also seen in the comparison between Domain B' and Domain C. While the side coefficient C_{f_y} presents an average deviation of $\sim 2.5\%$ from the reference case, the lift C_{f_z} has an average decrease of $\sim 6.5\%$. The maximum deviation is $\sim 7.5\%$, found for C_{f_z} at $\beta = 45°$. The higher deviation found for the lift is mainly responsible for the decrease on lee-rail moment coefficient $C^*_{M_{x,\mathrm{lee}}}$, with an average deviation of $\sim 3.5\%$.

The wake behavior is illustrated in Figure 55 with pressure coefficient iso-surfaces of $c_p = -1.5$ and $c_p = -2.0$ colored with the vorticity. The absence of the tip vortex reduces the train wake strength as the nose vortex detaches from the surface in Domain C earlier than in Domain B and B'.

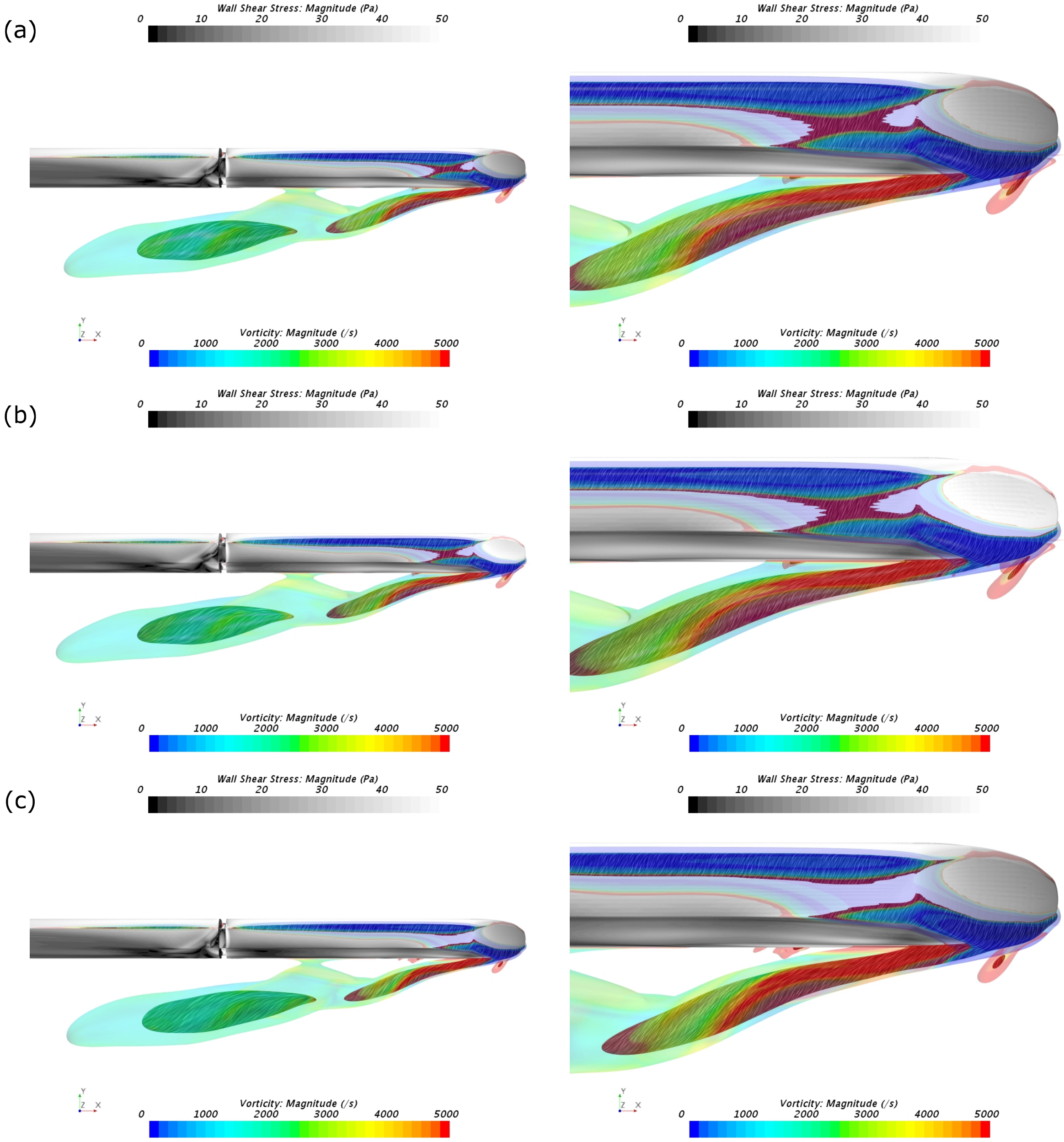

Figure 55 – Comparison of the wake behavior for Domain (a) B, (b) B' and (c) C with the SST $\gamma - \mathrm{Re}_\theta$ model at $\beta = 45°$. Vorticity colored iso-surfaces for pressure coefficients $c_p = -1.5$ (transparent) and $c_p = -2.0$ (opaque). Wall shear-stress at model surface.

The analysis of the STBR topography shows that the lift coefficient is the most sensitive to the STBR tip vortex. However, the use of an infinite STBR did not produce an extensive effect in the side force and moment coefficients. For static tests the use of a standard STBR does not have a major influence for assessing the lee-rail moment, and thus the train stability under crosswind conditions.

3.2.3 Moving Model

Static wind tunnel tests do not account for the interaction between the train and the ground. To study how the motion of the model affect the aerodynamic coefficients, CFD simulations were performed using Domain D (reduced-scale) and E (full-scale). In this analysis the wind direction is kept perpendicular to the train and the model motion is modeled using a moving reference frame (MRF). The wheel rotation was also simulated in the analysis. To ease the comparison with the static model, the relative wind velocity V_a was kept constant. The velocities of train V_{tr} and the wind V_w were adjusted to get the desired yaw angle β.

3.2.3.1 Reduced-scale Model

The comparison of the static and moving reduced-scale model was made between Domain C and D, and is presented in Figure 56. As in the previous analysis, the simulations were made for $\beta = 35°$, $45°$ and $55°$. The average difference between static and moving model is $\sim 2\%$ for both side force and rolling moment coefficients. Similar behavior was found in the experimental analysis from Bocciolone et al. (2008) and Dorigatti et al. (2012, 2015). The lift is higher for the moving model, with an average difference of $\sim 5.5\%$. The largest deviation is $C^*_{f_z} \sim 6.5\%$ at $\beta = 45°$.

The average difference between static (Domain C) and moving model (Domain D), which considers the same domain configuration, for the lee-rail moment coefficient is higher by $\sim 3\%$, showing that the static prediction is not far from a moving scaled-model. This is accordance with the analysis from Baker (1991), where an increase of the lift force is observed while the lee-rail moment coefficient remains similar.

Comparing the results from the reduced-scale moving model simulation and the reference case (Domain B), a similarity is found for the aerodynamic coefficients. The largest difference between the coefficients for Domain B and D is $\sim 3\%$, for both $C^*_{f_y}$ and $C^*_{M_{x,\mathrm{lee}}}$, while the difference for $C^*_{f_z}$ is bellow 2%. In average, Domain B produces aerodynamic coefficients 2% higher than Domain D. The proximity of the results shows that, considering a reduced-scale analysis, the STBR and splitter-plate configuration can lead to a crosswind analysis similar to a reduced-scale moving model, and at a lower cost, considering all the difficulties involved in setting up this kind of testing.

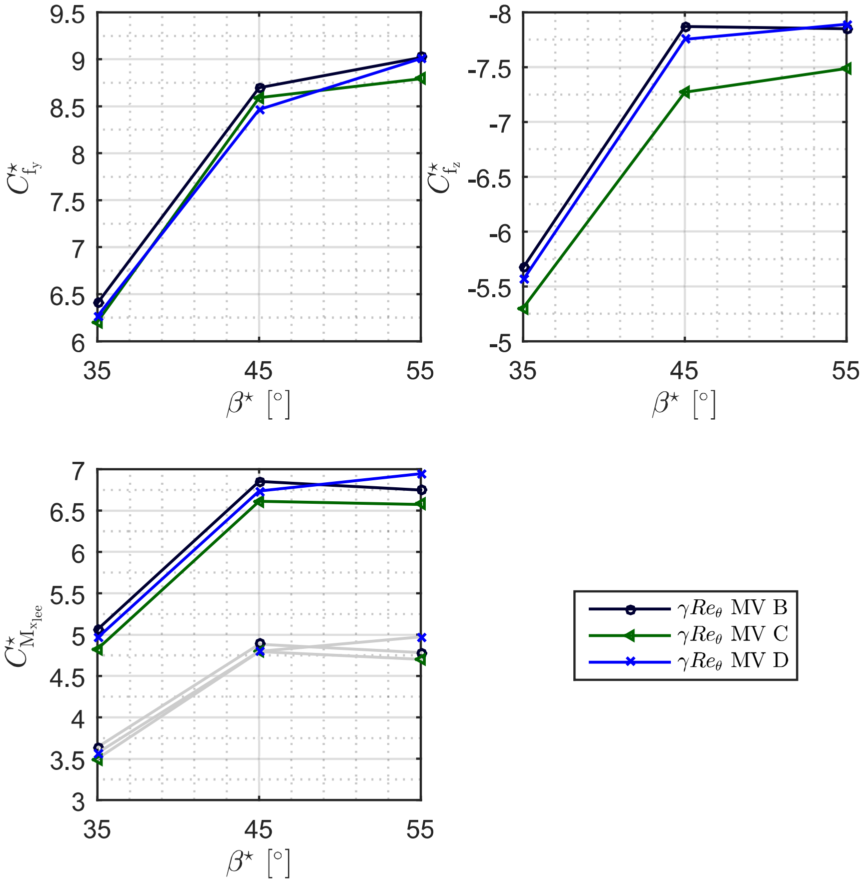

Figure 56 – Analysis of the side force, lift, rolling moment (gray line) and lee-rail moment coefficients for Domain B, C and D, SST $\gamma - \mathrm{Re}_\theta$ model. Yaw angle $\beta = 35°$ to $\beta = 55°$. Analysis for C_{f_y}, C_{f_z} and $C^*_{M_{x,\mathrm{lee}}}$, $C^*_{M_x}$ in gray.

In Figure 57 the velocity colored streamlines in the train reference frame (moving reference frame) for Domain D is presented. The flow behavior is similar to Domain B and B' (see Figure 48). It is important to remark that, as discussed in Section 2.2.3, the model axis is perpendicular to the flow, considering the inertial frame of reference. In Figure 57 we see the flow with respect to the moving reference frame (which follows the train motion), reproducing the relative wind.

The pressure and vorticity fields for Domain C and D are shown in Figure 58, at a yaw angle $\beta = 45°$. The lee-side pressure field is similar for both domains, as also seen for the side force coefficient $C^*_{f_y}$. The pressure distribution on the roof is stronger for Domain D, producing a higher lift force. The vortex core location is similar, as illustrated in the vorticity fields. The wake behavior is illustrated in Figure 59 with pressure coefficient iso-surfaces of $c_p = -1.5$ and $c_p = -2.0$ colored with the vorticity. The iso-surface develops further and it should be noted that the vortex detaches closer to the roof separation in Domain D than in Domain C.

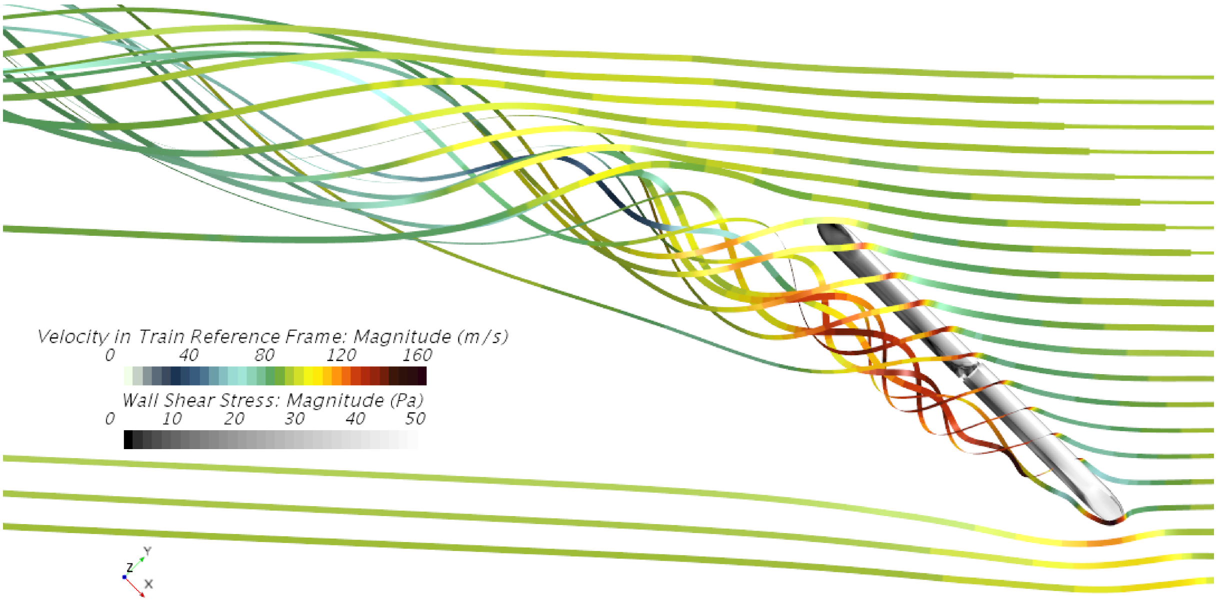

Figure 57 – Velocity colored streamlines in the train reference frame (moving frame) and wall shear stress at model surface for Domain D with the SST $\gamma - \mathrm{Re}_\theta$ model at $\beta = 45°$. The flow is from right to left.

This analysis is also made for Domain B and Domain D. Although the under-body flow is different, as expected due to the interaction between moving model and static STBR, the roof vortex is similar for both cases. The analysis of the pressure coefficient iso-surfaces in the roof, presented in Figure 59, shows same behavior for both cases. Although the wake iso-surface pressure coefficient iso-surfaces of $c_p = -1.5$ develops further for Domain D, its behavior is closer to Domain B than those to C.

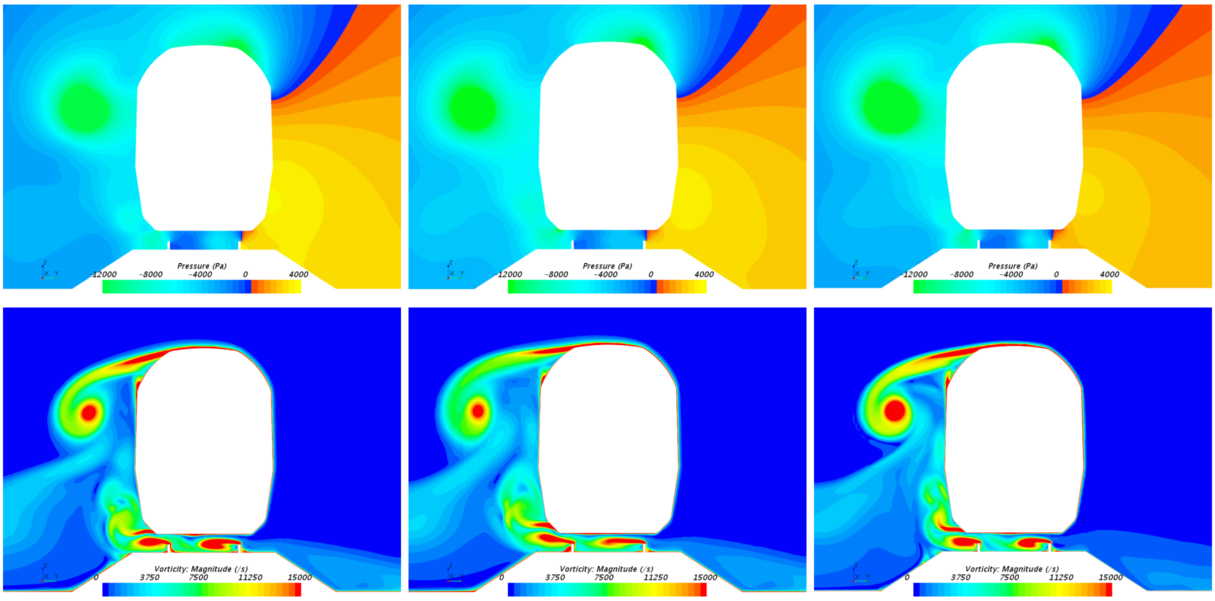

(a) (b) (c)

Figure 58 – Analysis of the vorticity and pressure fields, evaluated at *Plane I*, for Domain (a) B, (b) C and (c) D at yaw angle $\beta = 45°$. The flow is from right.

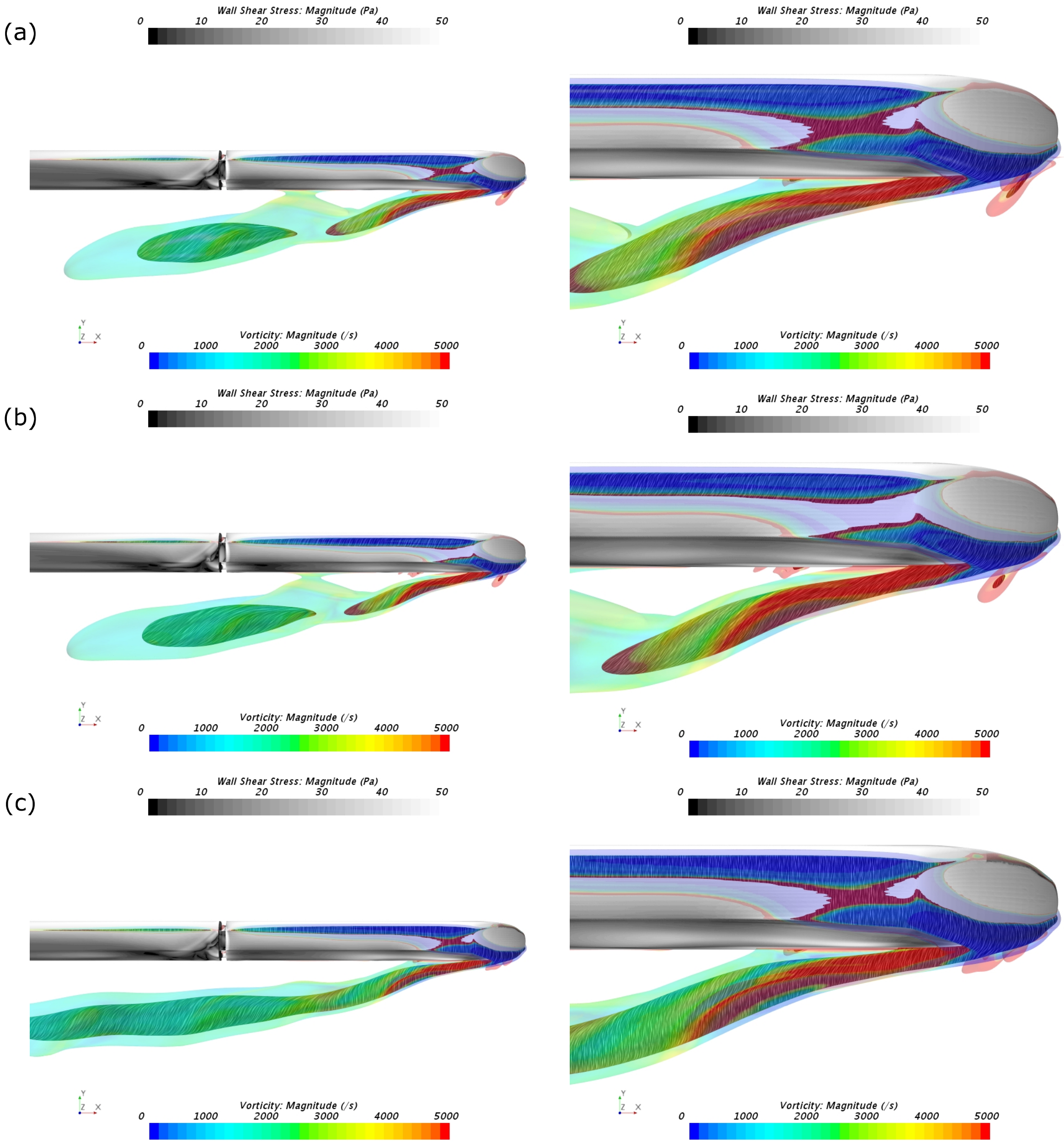

Figure 59 – Comparison of the wake behavior for Domain (a) B, (b) C and (c) D with the SST $\gamma - \mathrm{Re}_\theta$ model at $\beta = 45°$. Vorticity colored iso-surfaces for pressure coefficients $c_p = -1.5$ (transparent) and $c_p = -2.0$ (opaque). Wall shear-stress at model surface.

3.2.3.2 Full-scale Model

The analysis of a full-scale moving model was made in Domain E. The Reynolds number for the full-scale train was $1.75 \cdot 10^7$, 25 times larger than for the reduced-scale model. The comparison of the results from Domain D and Domain E is presented in Figure 60. The full-scale model presents a lower side force but higher lift coefficients, with an average of 10% and 15%, respectively for the range $\beta = 35° - 55°$. The lee-rail moment coefficient is reduced by an average $\sim 5\%$. Although the forces coefficients differences are larger ($avg[C^*_{f_z}] = 15\%$), the lee-rail moment coefficient $C^*_{M_{x,\mathrm{lee}}}$ is similar. This confirms the findings of Baker et al. (2004).

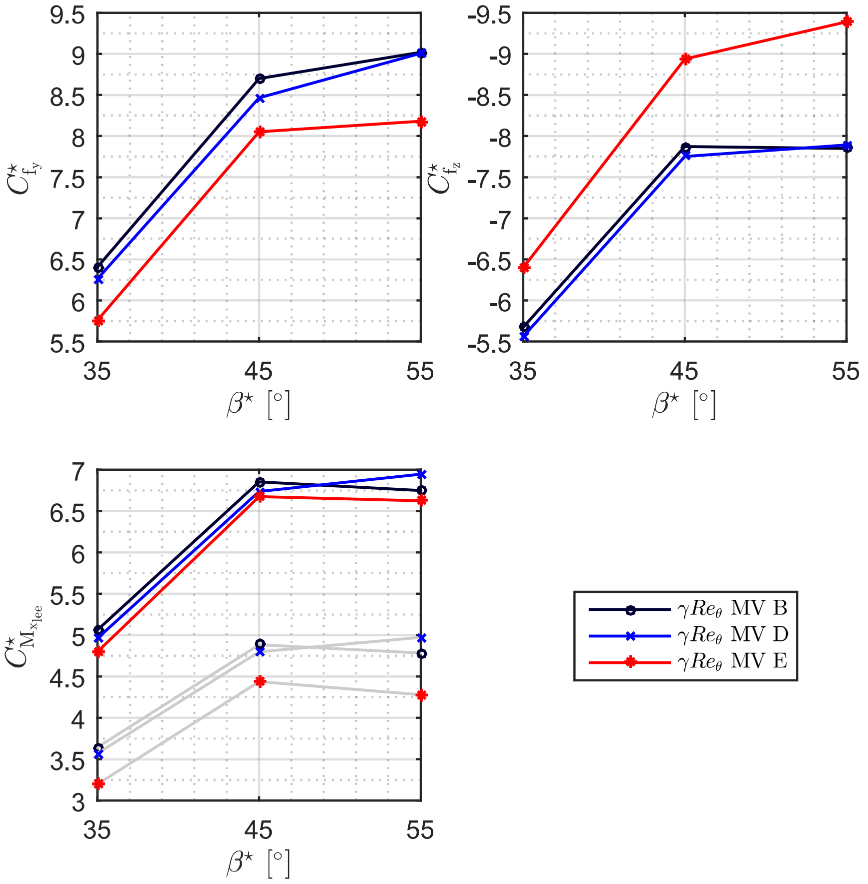

Figure 60 – Analysis of the side force, lift, rolling moment (gray line) and lee-rail moment coefficients for Domain B, D and E, SST $\gamma - \mathrm{Re}_\theta$ model. Yaw angle $\beta = 35°$ to $\beta = 55°$. Analysis for C_{f_y}, C_{f_z} and $C^*_{M_{x,\mathrm{lee}}}$, $C^*_{M_x}$ in gray.

The flow fields and the iso-surfaces of the pressure coefficient colored with the vorticity are presented in Figure 61. As explained by Copley (1987), the Reynolds number plays a significant role in crosswind stability. A higher Reynolds number can lead to a delayed flow detachment in the lee-ward roof corner. As the flow acceleration is higher in the roof region for the higher Reynolds number, the boundary layer has more energy and thus the flow only detach at a later point. This also contributes to a smaller wake, leading to a lower side force coefficient $C^*_{f_y}$. The absolute pressure on the roof of the reduced-scale model is higher than on the full-scale, seen in Figure 61, resulting in a lower lift coefficient $C^*_{f_z}$. The flow moves quicker on the roof of the moving model reducing the absolute pressure. Domain E vorticity intensity is approximately 25 times lower than in Domain D.

Figure 60 also compares the results of the full-scale moving model (Domain E) with the KKK wind tunnel 1:25 static model simulation (Domain B). It should be noted that the $C^*_{M_{x,\mathrm{lee}}}$ values are within 6% of each others for $\beta = 35°$, $45°$ and $55°$, with an average of 5%. This difference is small compared with the difference in the force coefficients, where $C^*_{f_y}$ is lower by an average of $\sim 10\%$ and $C^*_{f_z}$ higher by $\sim 14\%$.

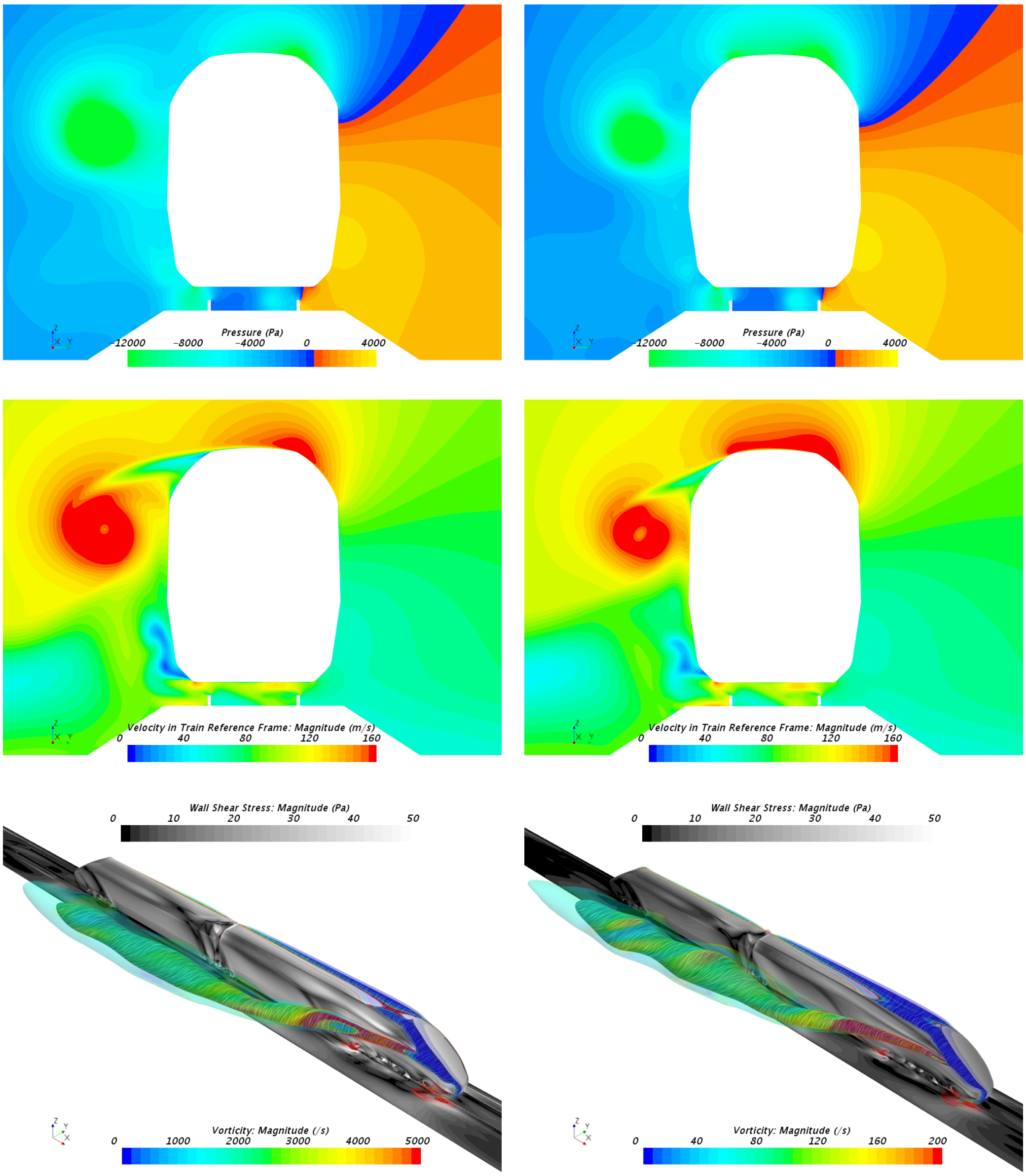

(a) (b)

Figure 61 – Analysis of the vorticity and pressure fields, evaluated at *Plane I*, and the wake behavior for Domain (a) D and (b) E with the SST $\gamma - \mathrm{Re}_\theta$ model at $\beta = 45°$. Vorticity colored iso-surfaces for pressure coefficients -1.5 (transparent) and -2.0 (opaque). Wall shear-stress at model surface.

The velocity fields and wake behavior for Domain B to E are presented in Figure 62. The use of a moving model accelerates the flow compared to static models, as illustrated in the velocity fields for the roof top and wake regions.

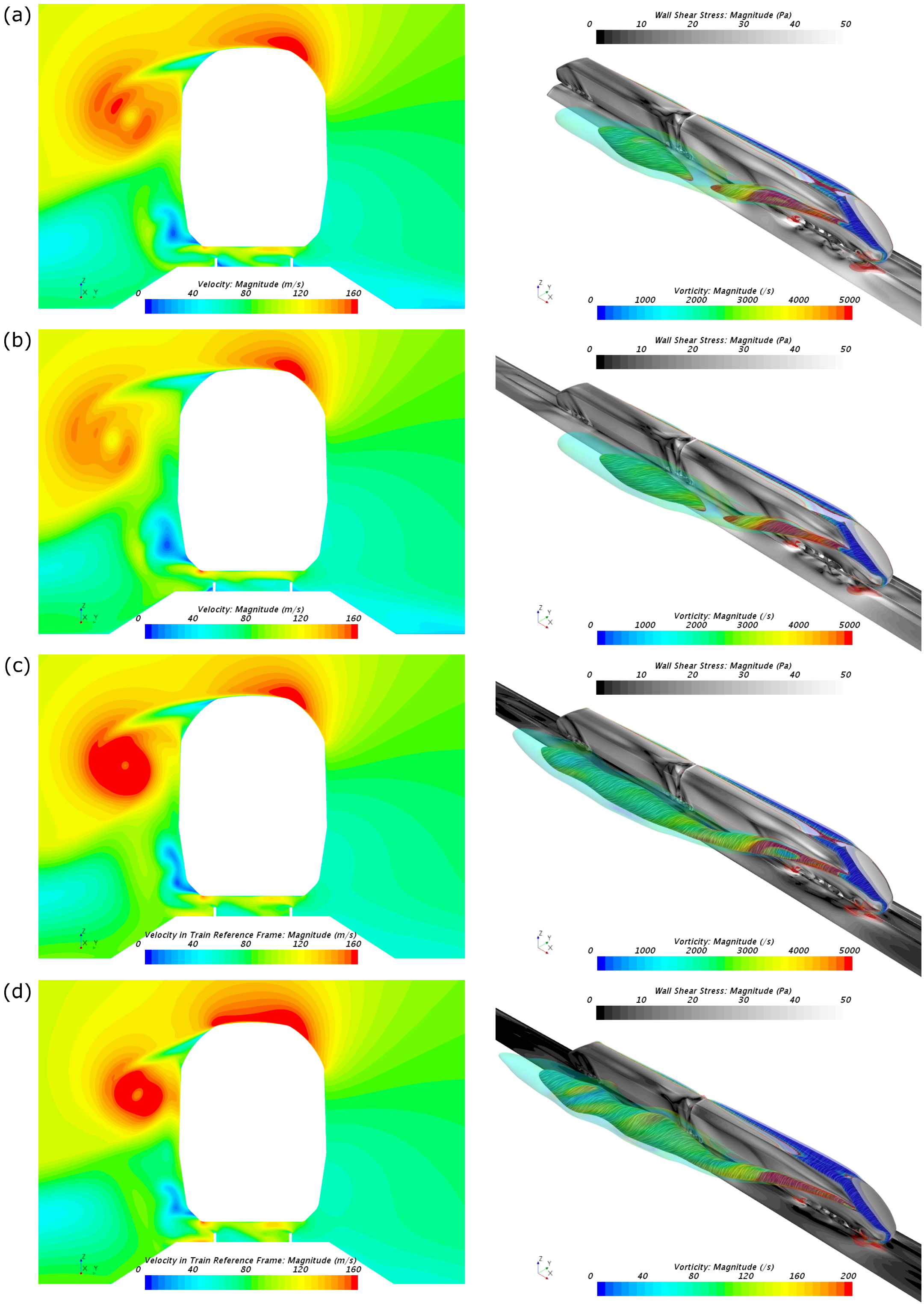

Figure 62 – Analysis of the velocity fields, evaluated at *Plane I*, and the wake behavior for Domain (a) B, (b) C, (c) D, and (d) E with the SST $\gamma - \mathrm{Re}_\theta$ model at $\beta = 45°$. Vorticity colored iso-surfaces for pressure coefficients -1.5 (transparent) and -2.0 (opaque). Wall shear-stress at surface.

3.2.4 Air Intake & Exhaust

The modeling of the air intake and exhaust was made on Domain E'. The inlets and outlets are illustrated in Figure 68 with the pressure coefficient iso-surfaces and velocity streamlines colored with vorticity.

Figure 63 presents the aerodynamic coefficients for Domain E and E'. The air intake and exhaust system of the train affects the flow by increasing the absolute pressure on the lee-side of the train, leading to the increase of the side force ($\sim 15\%$). The outlets cause an increase of the absolute pressure distribution on the train roof, which decrease the lift by $\sim 30\%$. Although the force coefficients differ by a large extent, they balance each other, leading to an increase of the lee-rail moment coefficient $C^{*}_{M_{x,\text{lee}}}$ of $\sim 5\%$.

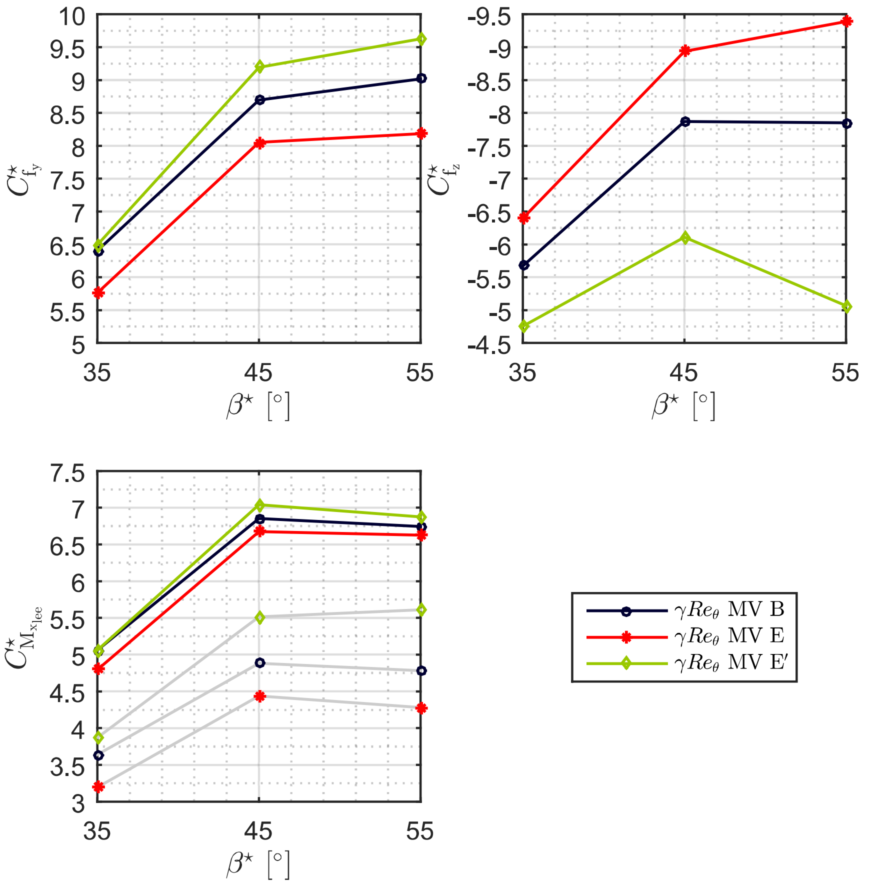

Figure 63 – Comparison of the aerodynamic coefficients for Domain E and E' at $\beta = 45°$ with the SST $\gamma - \mathrm{Re}_{\theta}$ turbulence model. Analysis for C_{f_y}, C_{f_z} and $C^{*}_{M_{x,\text{lee}}}$, $C^{*}_{M_x}$ in gray.

The pressure and velocity fields are displayed in Figure 64. The modeling of the inlets and outlets of the train change the flow behavior, increasing the energy of the wake, as the vorticity in the roof is stronger and sprawled of the train roof lee-ward corner. As seen in Figure 33, the exhaust outlets are located in the middle of the roof, and their interaction with the flow promotes an early detachment of the boundary layer, which enhances the vortex strength, leading to the increase of the side force coefficient. The detachment of the boundary layer also causes an increase of the pressure at the roof top, reducing the lift coefficient. This is also shown in Figure 69 for yaw angles from $\beta = 35° - 55°$.

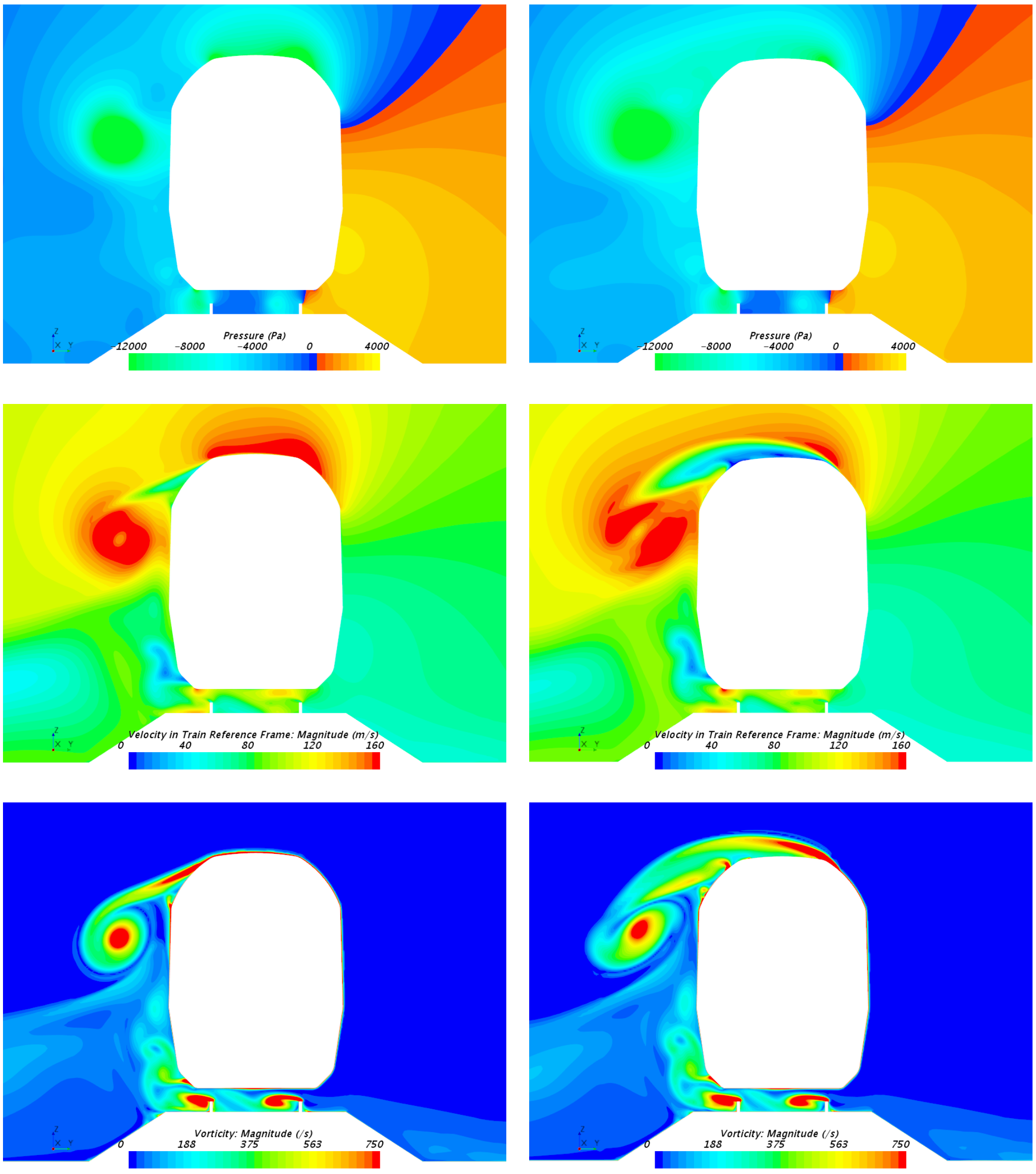

(a) (b)

Figure 64 – Analysis of the pressure, velocity and vorticity fields, evaluated at *Plane I*, for Domain (a) E and (b) E' with the SST $\gamma - \mathrm{Re}_\theta$ model at $\beta = 45°$. The flow is from right. Vorticity colored iso-surfaces for pressure coefficients -1.5 (transparent) and -2.0 (opaque). Wall shear-stress at surface.

The inlets and outlets located at the train's roof lead to detach the flow close to the wind-ward corner. This massive flow separation leads to a drastic decrease on local the velocity, increasing the roof pressure, which reduces the lift by a large extent, as seen in

Figure 63. The early flow separation also contributes to generate a larger wake, which leads to increase the side force. It is seen that this flow behavior produces a lee-rail moment coefficient $C^*_{M_{x,\text{lee}}}$ that, although similar to the prior case (Domain E), is still higher by $\sim 5\%$. Hence, we see that the intake and exhaust systems affect the train crosswind stability, as it can increase the lee-rail rolling moment, which can lead to train overturning in critical side wind conditions.

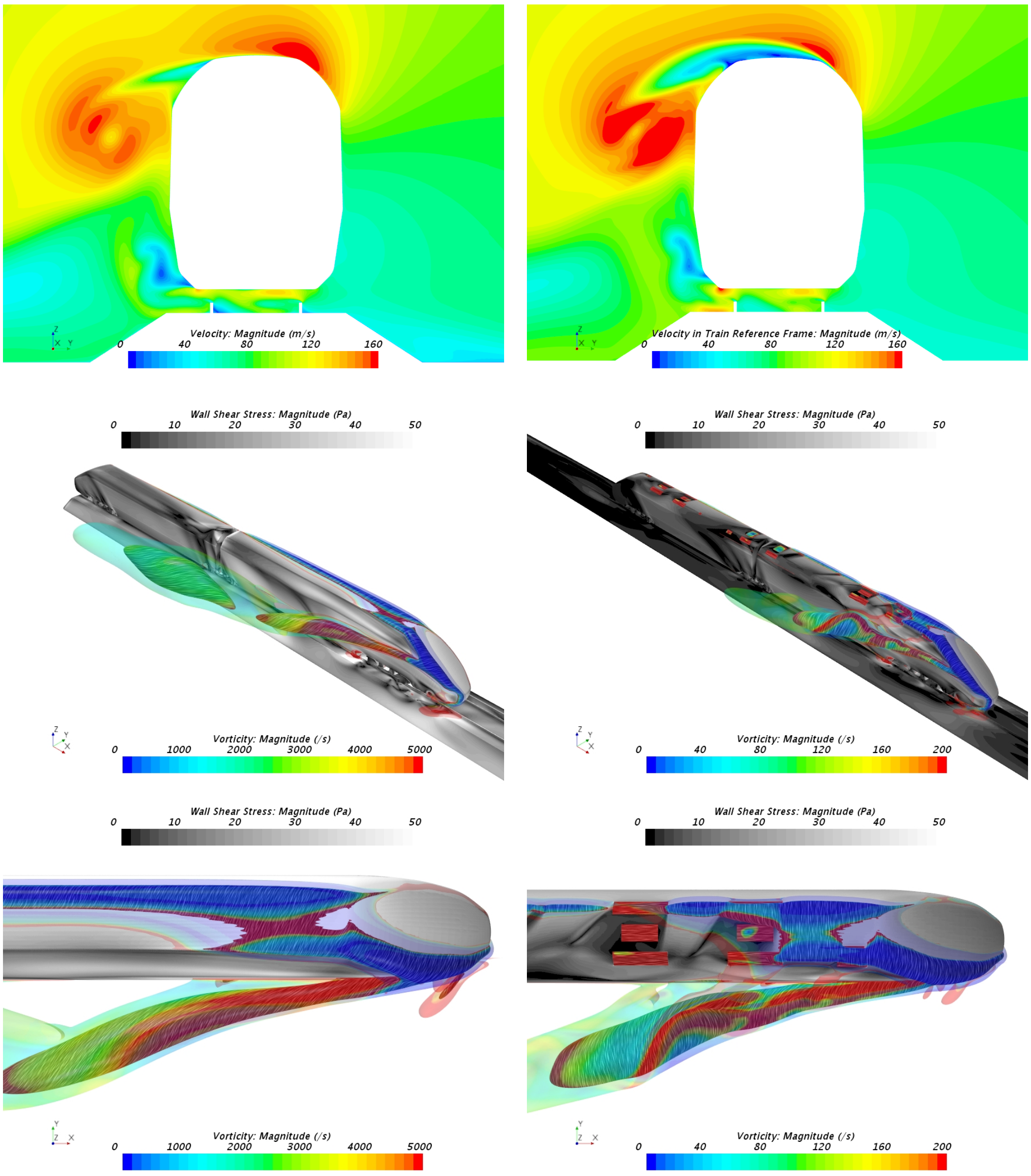

(a) (b)

Figure 65 – Analysis of the velocity fields, evaluated at *Plane I*, and the wake behavior for Domain (a) B and (b) E' with the SST $\gamma - \text{Re}_\theta$ model at $\beta = 45°$. The flow is from right. Vorticity colored iso-surfaces for pressure coefficients -1.5 (transparent) and -2.0 (opaque). Wall shear-stress at surface.

The comparison of the results between the full-scale moving train with inlets and outlets (Domain E') and the static scaled-model (Domain B) is presented in Figure 63. The reduced-scale model presents a lower side force coefficient with average deviation of $\sim 4\%$ and higher lift coefficient with an average deviation of 25%. The lee-rail moment coefficient is $\sim 3\%$ less than for the full-scale with inlets and outlets. The velocity fields and and wake behavior for Domain B and E' are presented in Figure 65.

As the lee-rail moment coefficient is critical to the train stability, even with the change caused by modeling the air intake and exhaust systems, the difference between the simulations for the static reduced-scaled model (Domain B) and full-scale train (Domain E') is small. This reassures the reliability of using standard wind tunnel tests to assess high-speed trains crosswind stability.

4 Conclusions

The aim of this research work was to increase the safety of high-speed trains in crosswind conditions by comparing the aerodynamic loads on a full scale moving train, with its intakes and exhausts, and a wind tunnel static 1:25 scale model.

Today, the European Norms EN-14607-6: *Requirements and test procedures for cross wind assessment*, requires that trains with a maximum speed between 200 and 360 km/h, to be tested in wind tunnels. The wind tunnel tests are carried out with static models positioned on a splitter plate to guaranty a reproducible homogeneous laminar flow. The train model is mounted directly over the splitter plate, on a 6-m high embankment or, as for this work, on a standardized Single Track Ballast and Rail (STBR) configuration. The splitter plate rotates within the wind tunnel to simulate different wind directions while the forces and moments acting on the 2 or 3-car model are recorded by 6-axis balances. Only the aerodynamic loads of the 1st and 2nd car are measured as they are the ones presenting the highest risk. The aerodynamic loads are then transferred to a Multi-Body Simulation (MBS) as boundary conditions to assess the stability of the train.

Wind tunnel tests do not represent the real conditions in which high-speed trains travel. The wind tunnel model neither simulates the relative motion of the train with the ground, nor the correct dangerous wind velocity, nor the different intakes and exhausts systems of a real high-speed train. The main objective of this study was to assess the limitations of static wind tunnel tests to obtain the train real aerodynamic coefficients.

Stadler EC250 high-speed train was used as the reference train during this study. Different configurations were tested at DLR Crosswind Simulation Facility (SWG) in Göttingen before one was homologated at DLR-KKK Cryogenic wind tunnel in Cologne in 2015. The experimental results of the leading car of the 2-car model served as reference values in this study.

Computational Fluid Dynamics (CFD) was used to study the influence of the wind tunnel setup on the aerodynamic coefficients. Before studying the influence of the setup on the results, our CFD software, STAR-CCM+ version 11.02, was validated on the original DLR-KKK wind tunnel geometry. All steady-state turbulence models were tested, to very few exceptions, on 5 different meshes for yaw angles ranging from 5° to 55°. Even if transient Delayed Detached Eddy Simulations (DDES) showed better potential than steady-state ones for yaw angle above 30°, this study restricted itself to RANS simulations for time and resources reasons. The Reynold Stress Model (RSM) and the Shear Stress Transport (SST) with the $\gamma - \mathrm{Re}_\theta$ transition model gave the overall best results for our finer mesh (Mesh V). The SST $\gamma - \mathrm{Re}_\theta$ was chosen over the RSM for two reasons: 1) it does not under-estimate C_{f_z} and 2) it converged faster.

An horizontal symmetry plane passing through the middle of the splitter plate was created to avoid solving the flow around the stands. This symmetry plane reduced the number of mesh cells by 20% and the CPU time by 15% without changing the value of the aerodynamic coefficients (<1%). When optimizing the design of a train to be wind tunnel tested, the use of a symmetry plane is a excellent way to cut down the cycle time.

The wind tunnel walls curve the far wake of the model as show in Figure 48. We showed that enlarging the tunnel width by 3 is enough to avoid this phenomena (see Figure 48), but also that the aerodynamic coefficients are not affected by this extension. The near wake does not change with the extension of the tunnel width and the pressure on the model surface stays the same, producing the same forces and moments.

The typical STBR mounted on the DLR splitter plate has finite dimensions. As for the train head, a vortex is generated at the tip of the finite STBR. The STBR tip vortex affects the flow on the lee-side of the model that increases the lift coefficient by $\sim 5\%$ compared with an infinitely long STBR (at $\beta = 45°$). The length of the STBR, its two extremities and the position of the model on it can change the aerodynamic coefficient measured. This represents a risk in the evaluation of the train safety and should be obviated.

A moving reference frame was used to simulate the relative motion between the model and the ground. The model was kept at 90° in the tunnel. The yaw angle was achieved by changing the wind velocity and the reference frame velocity while the relative wind amplitude was kept constant. Even if the resulting flow fields, side and lift coefficients (C_{f_y}, C_{f_z}) show large difference compared to an infinitely long STBR (+5% at $\beta = 55°$, +7% at $\beta = 45°$) with a static model, the rolling moment coefficient around the leeward rail increases only by 3%. Compared to the static model with standardized STBR the lee-rail moment is reduced by 2%.

The Reynolds numbers achieved in the DLR-KKK wind tunnel are ~25 times smaller than the full scale ones. To evaluate the effects of the Reynolds number, the EC250 model was blown up back to its real dimensions and was kept in a MRF. It should be noted that for this simulation, the Mesh V parameters were modified to keep capturing correctly the boundary layer. The lift coefficient C_{f_z} increases by 15% while the side force coefficient C_{f_y} decreased by 10% (at $\varphi = 45°$). Again it should be noted that the rolling moment coefficient around the leeward rail only decreases by 5%.

During wind tunnel tests, the multiple intakes of fresh air and exhausts of hot air are not reproduced. A full scale 2-car moving EC250 was simulated with all the inlets and outlets found on the 2 end cars modeled as vents. The flow field on the roof is very different than the one without the vents resulting in very different lift and side force coefficients.

Surprisingly the rolling moment coefficient around the leeward rail only decreases by 3%.

The analysis of the different parameters shows that, although the lift coefficient C_{f_z} and side force coefficient C_{f_y} present larger differences between a full-scale moving train and a static wind tunnel model, the lee-rail moment coefficients $C^*_{M_{x,\text{lee}}}$ are within 5% of each others. We can conclude that static wind tunnel tests are reliable on the assessment of high-speed train crosswind stability.

4.1 Future Work

For time and resource reasons, this study was limited to steady-state simulations. Nonetheless some simulations were run as Delay Detached Eddy Simulations (DDES) with the SST $\gamma - \text{Re}_\theta$ turbulence model and show great potential. The SST $\gamma - \text{Re}_\theta$ steady-state results should be compared with the DDES for all yaw angles to see if this trend can be generalized.

The simulation model was validated using the wind tunnel 2-car model. Even if the 2 first cars are known to be the most critical, a full train should be modeled and the results compared with the 2-car configuration used in this study.

The reference STBR ground configuration was preferred over the True Flat Ground (TFG) and 6-m high embankment as the upcoming EN-14607-6 norm will drop the last two. Nonetheless, the real overturning risk can only be defined by taking into account the surrounding terrain traveled through by the train. To assess the real overturning risk more realistic terrain topography should be studied.

Last but not least, the aerodynamic coefficients are currently measured in laminar condition and the wind gusts are modeled in the MBS by a Chinese hat, while real trains travel in the lower part of the Atmospheric Boundary Layer (ABL). The influence of the ABL wind on the aerodynamics load of a high-speed train should be studied to ensure that the methodology used today is neither unsafe, nor over-constrained.

Bibliography

Baker, C. Train aerodynamic forces and moments from moving model experiments. *Journal of Wind Engineering and Industrial Aerodynamics*, v. 24, n. 3, p. 227–251, 1986. ISSN 01676105. https://dx.doi.org/10.1016/0167-6105(86)90024-3

Baker, C. Ground vehicles in high cross winds, part I: steady aerodynamic forces. *Journal of Fluids and Structures*, v. 5, n. 1, p. 69–90, 1991. ISSN 10958622. https://dx.doi.org/10.1016/0889-9746(91)80012-3

Baker, C. et al. Measurements of the cross wind forces on trains. *Journal of Wind Engineering and Industrial Aerodynamics*, v. 92, p. 547–563, 2004. ISSN 01676105. https://dx.doi.org/10.1016/j.jweia.2004.03.002

Baker, C. The flow around high-speed trains. *Journal of Wind Engineering and Industrial Aerodynamics*, v. 98, p. 277–298, 2010. ISSN 01676105. https://dx.doi.org/10.1016/j.jweia.2009.11.002

Billard, F.; Laurence, D. A robust $\kappa - \varepsilon - v^2/\kappa$ elliptic blending turbulence model with improved predictions in near-wall, separated and buoyant flows. *International Journal of Heat and Fluid Flow*, v. 44, p. 1–25, 2011. https://dx.doi.org/10.1016/j.ijheatfluidflow.2011.11.003

Bocciolone, M. et al. Crosswind action on rail vehicles: Wind tunnel experimental analyses. *Journal of Wind Engineering and Industrial Aerodynamics*, v. 96, p. 584–610, 2008. ISSN 01676105. https://dx.doi.org/10.1016/j.jweia.2008.02.030

Carrarini, A. Reliability based analysis of the crosswind stability of railway vehicles. *Journal of Wind Engineering and Industrial Aerodynamics*, v. 95, n. 7, p. 493–509, 2007. ISSN 01676105. https://dx.doi.org/10.1016/j.jweia.2006.10.001

CD-ADAPCO. *Spotlight on... Turbulence.* Melville, 2015. 42 p.

CD-ADAPCO. *STAR-CCM+ User Guide, Version 11.02.009-R8.* Melville, 2016.

Chiu, T.; Squire, L. An experimental study of the flow over a train in a crosswind at large yaw angles up to 90°. *Journal of Wind Engineering and Industrial Aerodynamics*, v. 45, p. 47–74, 1992. ISSN 01676105. https://dx.doi.org/10.1016/0167-6105(92)90005-U

Chiu, T. Prediction of the aerodynamic loads on a railway train in a cross-wind at large yaw angles using an integrated two- and three-dimensional source/vortex panel method. *Journal of Wind Engineering and Industrial Aerodynamics*, v. 57, p. 19–39, 1995. ISSN 01676105. https://dx.doi.org/10.1016/0167-6105(94)00099-Y

Copley, J. The Three-Dimensional Flow around Railway Trains. *Journal of Wind Engineering and Industrial Aerodynamics*, v. 26, p. 21–52, 1987. ISSN 01676105. https://dx.doi.org/10.1016/0167-6105(87)90034-1

Davis, P. L.; Rinehimer, A. T.; Uddin, M. A comparison of RANS-based turbulence modeling for flow over a wall-mounted square cylinder. In: *20th Annual Conference of the CFD Society of Canada.* Canmore: [s.n.], 2012. p. 8.

Deliancourt, F. *Etude de l'aérodynamique des trains en situation de vents traversiers: impact de la présence d'appendices*. 184 p. Tese (Autre) — ISAE-ENSMA École Nationale Supérieure de Mécanique et D'Aérotechnique - Poitiers, 2015.

Diedrichs, B. et al. Crosswind stability of a high-speed train on a high embankment. In: *Proc. IMechE, Part F: J. Rail and Rapid Transit*, v. 221, n. 2, p. 205–225, 2007. https://dx.doi.org/10.1243/0954409JRRT126

Diedrichs, B. Aerodynamic calculations of crosswind stability of a high-speed train using control volumes of arbitrary polyhedral shape. In: *BBAA VI International Colloquium on: Bluff Bodies Aerodynamics & Applications*. Milano: [s.n.], 2008. p. 20–24.

Dorigatti, F. et al. Evaluation of crosswind effects on rail vehicles through moving model experiments. In: *BBAA VII International Colloquium on: Bluff Bodies Aerodynamics & Applications*. Shanghai: [s.n.], 2012. p. 1480–1489.

Dorigatti, F. et al. Crosswind effects on the stability of a model passenger train - A comparison of static and moving experiments. *Journal of Wind Engineering and Industrial Aerodynamics*, v. 138, p. 36–51, 2015. ISSN 01676105. https://dx.doi.org/10.1016/j.jweia.2014.11.009

EN-14607-6. Requirements and test procedures for cross wind assessment. European Standards, 2010.

International Union of Railways (UIC). High Speed Rail: Fast Track to Sustainable Mobility. 2015. ISBN 978-2-7461-1887-4.

Jones, L.; Launder, B. The prediction of laminarization with a two-equation model of turbulence. *International Journal of Heat and Mass Transfer*, v. 15, n. 2, p. 301–314, 1972. ISSN 0017-9310. https://dx.doi.org/10.1016/0017-9310(72)90076-2

Launder, B.; Reece, G. J.; Rodi, W. Progress in the development of a Reynolds-Stress turbulent closure. *Journal of Fluid Mechanics*, v. 68, n. 3, p. 537–566, 1975. ISSN 0022-1120. https://dx.doi.org/10.1017/S0022112075001814

Mair, W. A.; Stewart, A. J. The flow past yawed slender bodies, with and without ground effects. *Journal of Wind Engineering and Industrial Aerodynamics*, v. 18, n. 3, p. 301–328, 1985. ISSN 01676105. https://dx.doi.org/10.1016/0167-6105(85)90088-1

Menter, F. R. Zonal Two Equation Kappa-Omega Turbulence Models for Aerodynamic Flows. In: *24th AIAA Fluid Dynamics Conference*. Orlando, FL: AIAA, 1993. p. 22. https://dx.doi.org/10.2514/6.1993-2906

Menter, F. R. et al. A Correlation-based Transition Model Using Local Variables: Part I – Model Formulation. In: *Proceedings of the ASME Turbo Expo, Power for Land Sea and Air*. Vienna: ASME, 2004. p. 57–67. ISBN 0-7918-4169-3. https://dx.doi.org/10.1115/1.2184352

Peters, J.-L. How to Reduce the Cross Wind Sensitivity of Trains. In: *The Aerodynamics of Heavy Vehicles: Trucks, Buses, and Trains*. 19. ed. Berlin, Heidelberg: Springer Berlin Heidelberg, 2004. cap. 40, p. 453–467. ISBN 978-3-540-44419-0. https://doi.org/10.1007/978-3-540-44419-0_40

Proppe, C.; Wetzel, C. Overturning Probability of Railway Vehicle under Wind Gust Loads. In: *Proceedings of the IUTAM Symposium on Dynamics and Control of Nonlinear Systems with Uncertainty.* Nanjing: Springer, 2007. p. 23–32. ISSN 18753507. https://doi.org/10.1007/978-1-4020-6332-9_3

Reynolds, O. On the Dynamical Theory of Incompressible Viscous Fluids and the Determination of the Criterion. *Philosophical Transactions of the Royal Society of London A: Mathematical, Physical and Engineering Sciences*, The Royal Society, v. 186, p. 123–164, 1895. ISSN 0264-3820. https://dx.doi.org/10.1098/rsta.1895.0004

Robinson, C.; Baker, C. The Effect of Atmospheric Turbulence on Trains. *Journal of Wind Engineering and Industrial Aerodynamics*, v. 34, p. 251–272, 1990. https://doi.org/10.1016/0167-6105(90)90155-6

Schetz, J. Aerodynamics of High-Speed Trains. *Annual Review of Fluid Mechanics*, Elsevier, v. 33, p. 371–414, 2001. ISSN 00664189. https://dx.doi.org/10.1146/annurev.fluid.33.1.371

Schober, M. et al. Wind tunnel investigation of an ICE 3 endcar on three standard ground scenarios. *Journal of Wind Engineering and Industrial Aerodynamics*, Elsevier, v. 98, n. 6-7, p. 345–352, 2010. ISSN 01676105. https://dx.doi.org/10.1016/j.jweia.2009.12.004

Shih, T.-H. et al. A new k-epsilon eddy viscosity model for high reynolds number turbulent flows. *Computers & Fluids*, v. 24, n. 3, p. 227–238, 1995. ISSN 00457930. https://dx.doi.org/10.1016/0045-7930(94)00032-T

Spalart, P.; Allmaras, S. A one-equation turbulence model for aerodynamic flows. In: *30th Aerospace Sciences Meeting and Exhibit.* Reno: American Institute of Aeronautics and Astronautics, 1992. (Aerospace Sciences Meetings). https://dx.doi.org/10.2514/6.1992-439

Sturmarchiv Schweiz. *Rotorwind Wasserauen - 19 Januar 2007.* 2007. Available in: https://www.sturmarchiv.ch/index.php/20070119_02_Rotorwind_Wasserauen. Accessed in: 17.05.2016.

The Japan Times. *Typhoon death toll hits eight.* Tokyo: Japan, 2006. Available in: https://www.japantimes.co.jp/news/2006/09/18/national/typhoon-death-toll-hits-eight/#.VzNSK4R96Xo. Accessed in: 17.05.2016.

Thompson, K. J.; Morrison, D. F. The spacing, position and strength of vortices in the wake of slender cylindrical bodies at large incidence. In: *Journal of Fluid Mechanics*, v. 50, p. 751–783, 1992. ISSN 0022-1120. https://dx.doi.org/10.1017/S0022112071002878

TSI-HS-RST. Technical specification for Interoperability relating to the Rolling Stock sub-system of the trans-European high-speed rail system. (2008/232/CE), 2008.

Wilcox, D. C. *Turbulence Modeling for CFD.* 3. ed. [S.l.]: DCW Industries, 2006. 515 p. ISBN 9781928729082. https://dx.doi.org/0963605151

Xinhua News Agency. *Strong wind derails train, killing 4.* 2007. Available in: https://www.china.org.cn/english/China/200975.htm. Accessed in: 18.05.2016.

Appendix

APPENDIX A – Setup for Mesh V and the γRe_θ Transition Model

This appendix provides the necessary information to reproduce Mesh V and implement the $\gamma - \mathrm{Re}_\theta$ transition model in the commercial solver STAR-CCM+.

A.1 Instructions for Mesh V

To generate Mesh V four different coordinate systems are necessary: the Global coordinate system, the top-of-rail (TOR) coordinate system, the Train coordinate system (EN-14607-6) and the Wind tunnel coordinate system. The first three ones are fixed while the last one rotates to give the yaw angle β. The aerodynamic coefficients are measured with respect to the Train coordinate system. The coordinates of each system are given in Table 11.

Coordinate System	**Reference System**	**Origin [x, y, z] m**
Global	-	$[0.00, 0.00, 0.00]$
TOR	Global	$[0.00, 0.00, 0.05]$
Train	TOR	$[0.08, 0.00, 0.00]$
Wind tunnel	TOR	$[0.00, 0.00, 0.00]$

Table 11 – Coordinate systems applied for Mesh V.

The wind tunnel domain is generated in the Wind tunnel coordinate system. As the coordinate system is rotated to achieve the desired yaw angle β, so does the domain. The volume controls are generated in the Train coordinate system. These parts are created as block shape parts inside the STAR-CCM+ geometry environment and the information concerning each one is given in Table 12.

The mesh used both Trimmed Cell and Prism Layer meshers, and the parameters used to generate Mesh V are presented in the following tables. Table 13 presents the default mesh controls while Table 14 and 15 present the custom surface and volume controls applied, respectively.

Part	**Reference System**	**Corner 1 [m]**	**Corner 2 [m]**
Wind tunnel DLR-KKK	Wind tunnel	$[-80.000, -1.200, -0.245]$	$[+2.700, +1.200, +2.160]$
Wind tunnel Symmetry	Wind tunnel	$[-80.000, -1.200, -0.050]$	$[+2.700, +1.200, +2.160]$
VC1	Train	$[-2.580, +0.800, -0.300]$	$[+1.170, -0.250, +0.050]$
VC2	Train	$[-1.380, +0.300, +0.050]$	$[+0.570, -0.120, -0.210]$
VC3	Train	$[-1.235, -0.065, -0.185]$	$[+0.575, +0.120, +0.050]$
VC4	Train	$[-1.185, -0.060, -0.010]$	$[+1.025, +0.060, +0.010]$

Table 12 – Wind tunnel domain and volume controls with respective coordinate systems.

Mesh Control	**Value**
Base Size	70.4 mm
Target Surface Size	100%
Minimum Surface Size	0.390625%
Surface Growth Rate	1.3
Maximum Core/Prism Transition Ratio	2.0
Volume Growth Rate	Slow
Surface Growth Rate	Medium
Max Cell Size	200%

Table 13 – Default mesh controls. The items with percentage are relative to the Mesh Base Size.

Surface Control	**Target Surface Size**	**Minimum Surface Size**	**Prism Layers**	**P.L. Thickness**
Wind tunnel	100.0%	-	4	100.0%
Train	1.5625%	0.78125%	12	0.8 mm
Bogies	0.78125%	0.390625%	4	0.4 mm
STBR	1.5625%	0.78125%	10	0.8 mm
Splitter Plate	25.0%	6.25%	10	1.2 mm

Table 14 – Custom surface controls. The items with percentage are relative to the Mesh Base Size. The Prism Layer Stretching was set to 1.5 for all surfaces and the Trimmer Surface Growth Rate set to slow.

A.2 Instructions for the γRe_θ Transition Model

To apply the $\gamma - \mathrm{Re}_\theta$ transition model in the SST turbulence model simulations it is necessary to define the location of the free-stream edge. The user has to create a User Field Function that defines the free-stream, and the function must have a value of 1 in the free-stream region and 0 inside the boundary layer.

In our calculations the prism layer mesh was created to cover the boundary layer region. A User Field Function was generated yielding a value of 1 outside the prism layer and 0 inside the prism layer. The designed field function is given in Equation A.1.

$$abs(\$PrismLayerCells - 1) \tag{A.1}$$

With this function it is estimated that the boundary layer is everywhere inside the prism layer. This User Field Function must then be assigned to Freestream Edge in the properties of the Gamma ReTheta transition model, inside the desired Continua properties.

Volume Control	**Target Surface Size**
VC1	12.5%
VC2	3.125%
VC3	1.5625%
VC4	0.78125%
Wind tunnel	100.0%

Table 15 – Custom volume controls. The items with percentage are relative to the Mesh Base Size.

APPENDIX B – Additional Illustrations

This appendix provides some illustrations that may be useful to better understand the flow at different yaw angles β. These illustrations are presented in Figure 66 to 70.

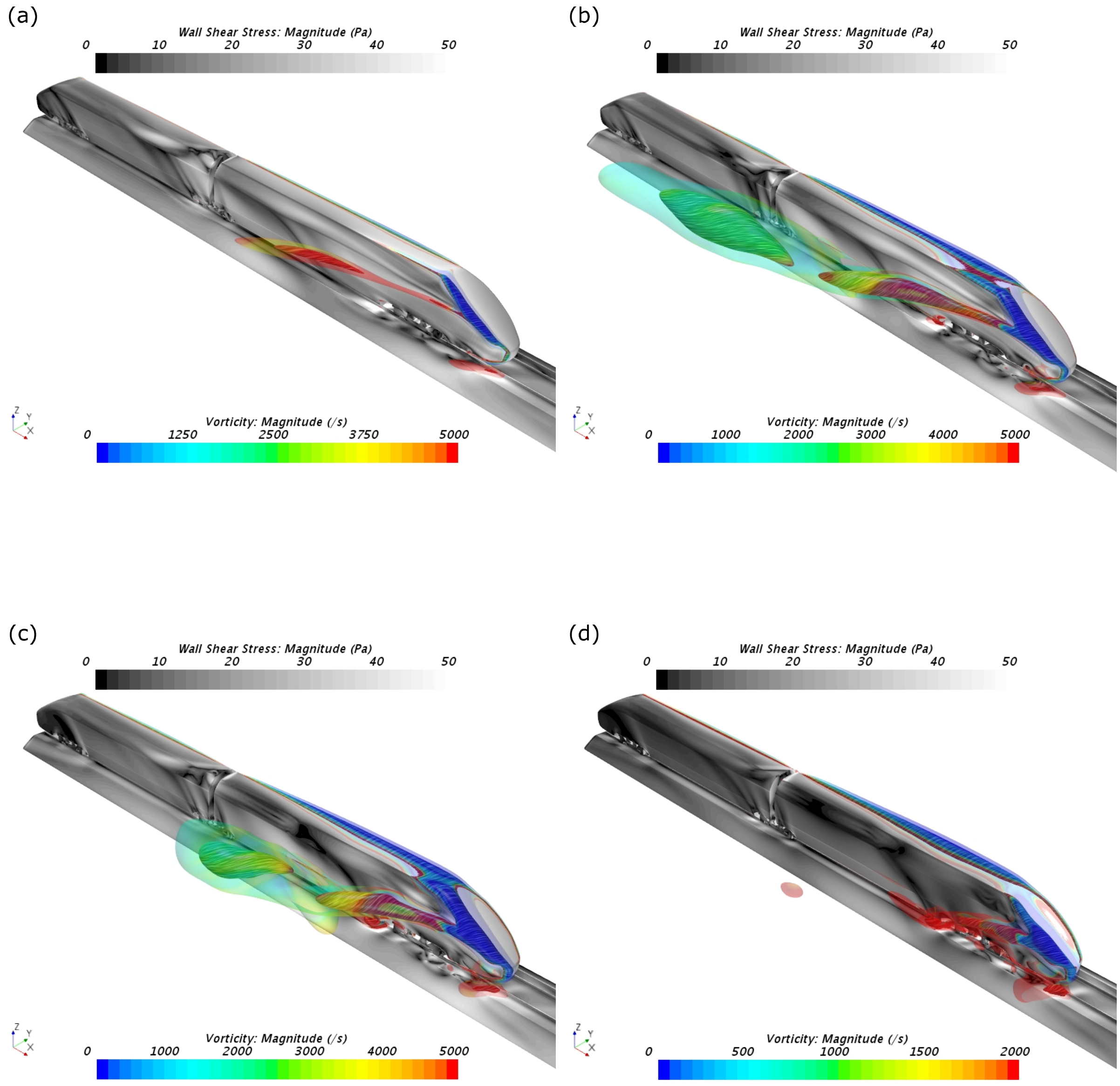

Figure 66 – Evolution of the wake behavior at high yaw angles for Mesh V, Domain B with the SST $\gamma - Re_\theta$ model. Vorticity colored iso-surfaces for pressure coefficients $c_p = -1.5$ (transparent) and $c_p = -2.0$ (opaque). Wall shear-stress at model surface. (a) 35°, (b) 45°, (c) 50° and (d) 55°.

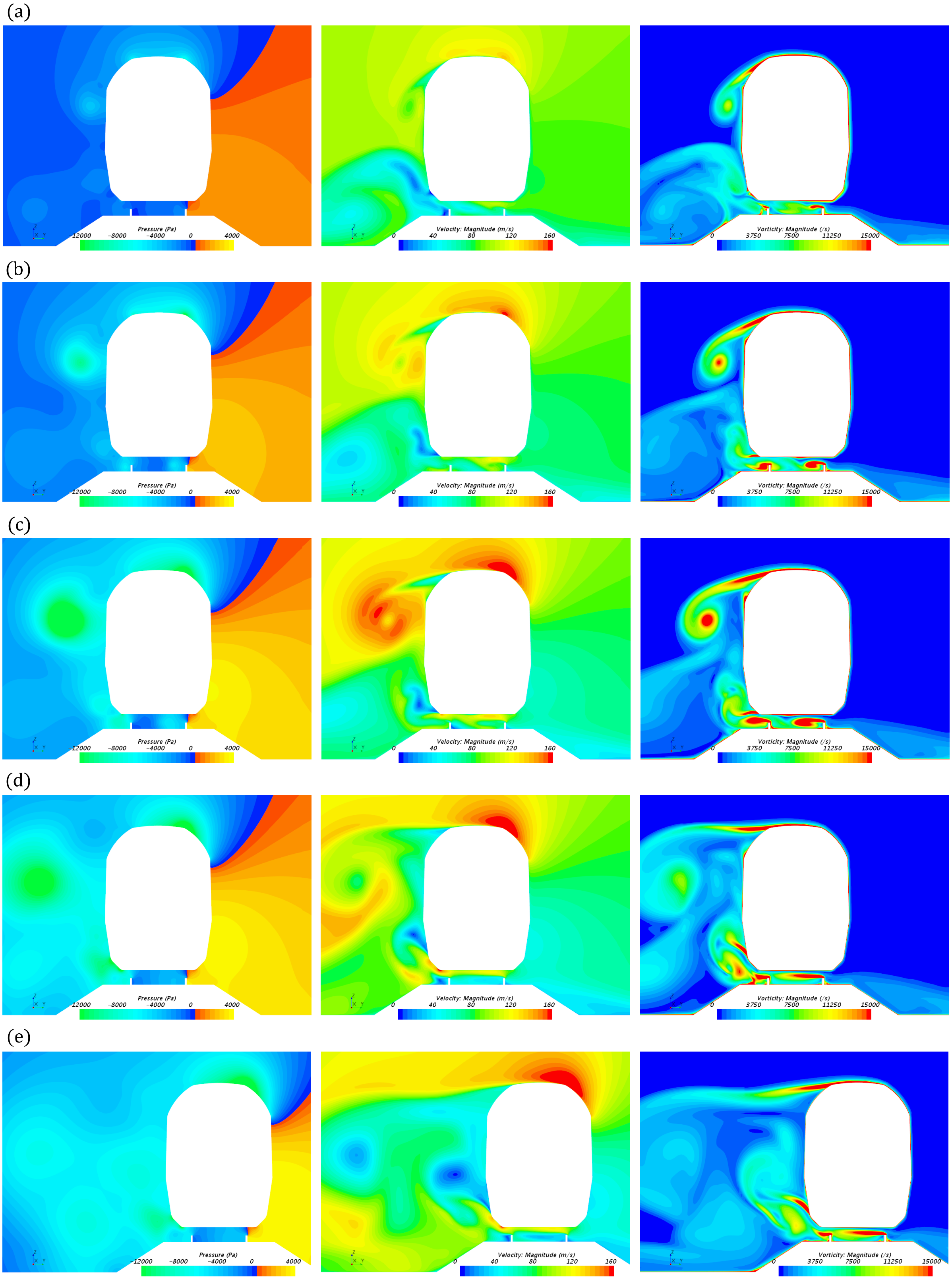

Figure 67 – Analysis of the pressure, velocity and vorticity fields, evaluated at *Plane I*, for Mesh V, Domain B for different yaw angles. Results obtained with the SST turbulence model. (a) 25°, (b) 35°, (c) 45°, (d) 50° and (e) 55°.

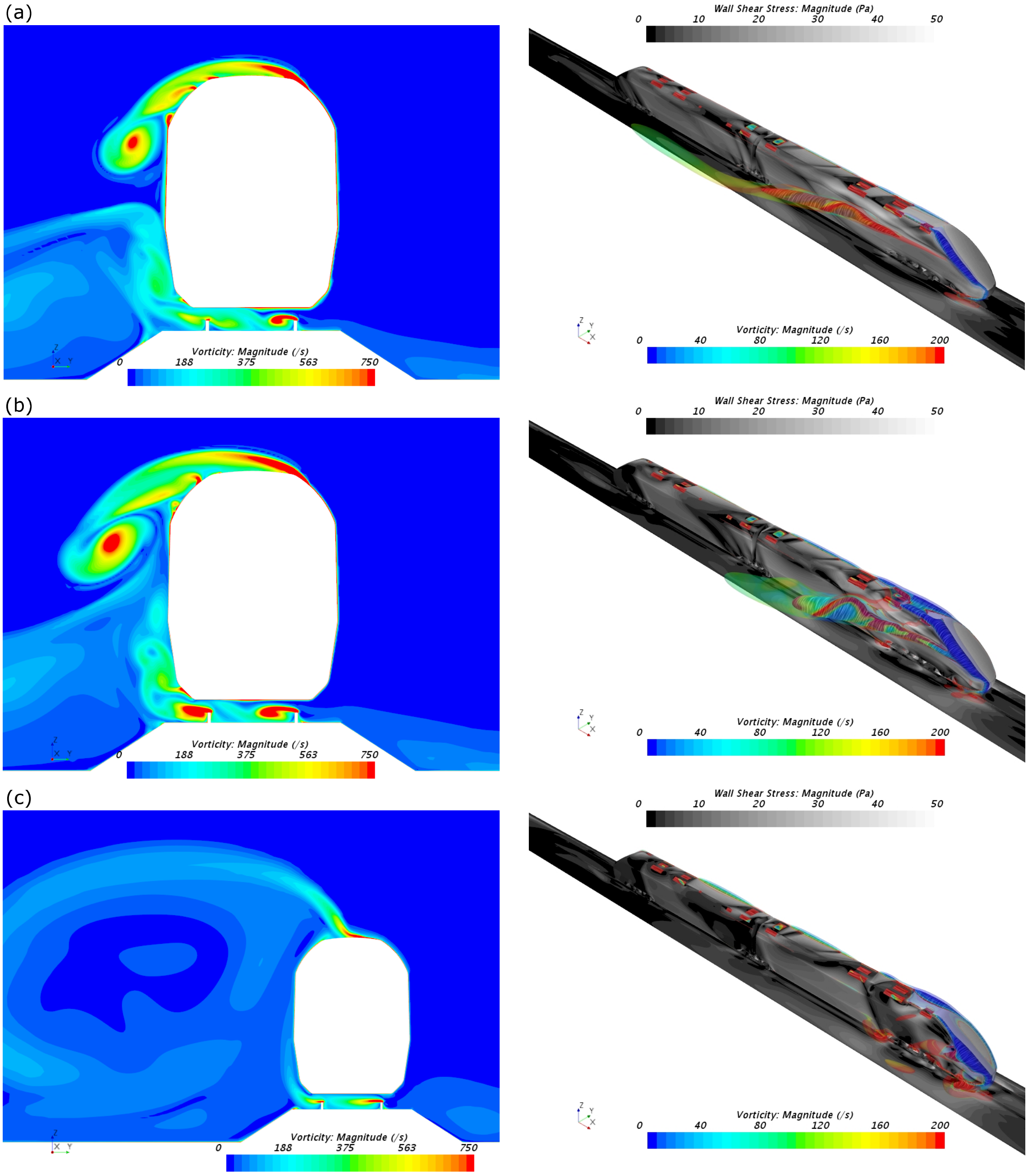

Figure 68 – Analysis of the vorticity fields, evaluated at *Plane I*, and evolution of the wake behavior for Mesh V, Domain E' with the SST $\gamma - \mathrm{Re}_\theta$ model. Vorticity colored iso-surfaces for pressure coefficients $c_p = -1.5$ (transparent) and $c_p = -2.0$ (opaque). Wall shear-stress at model surface. (a) 35°, (b) 45°, (c) 55°.

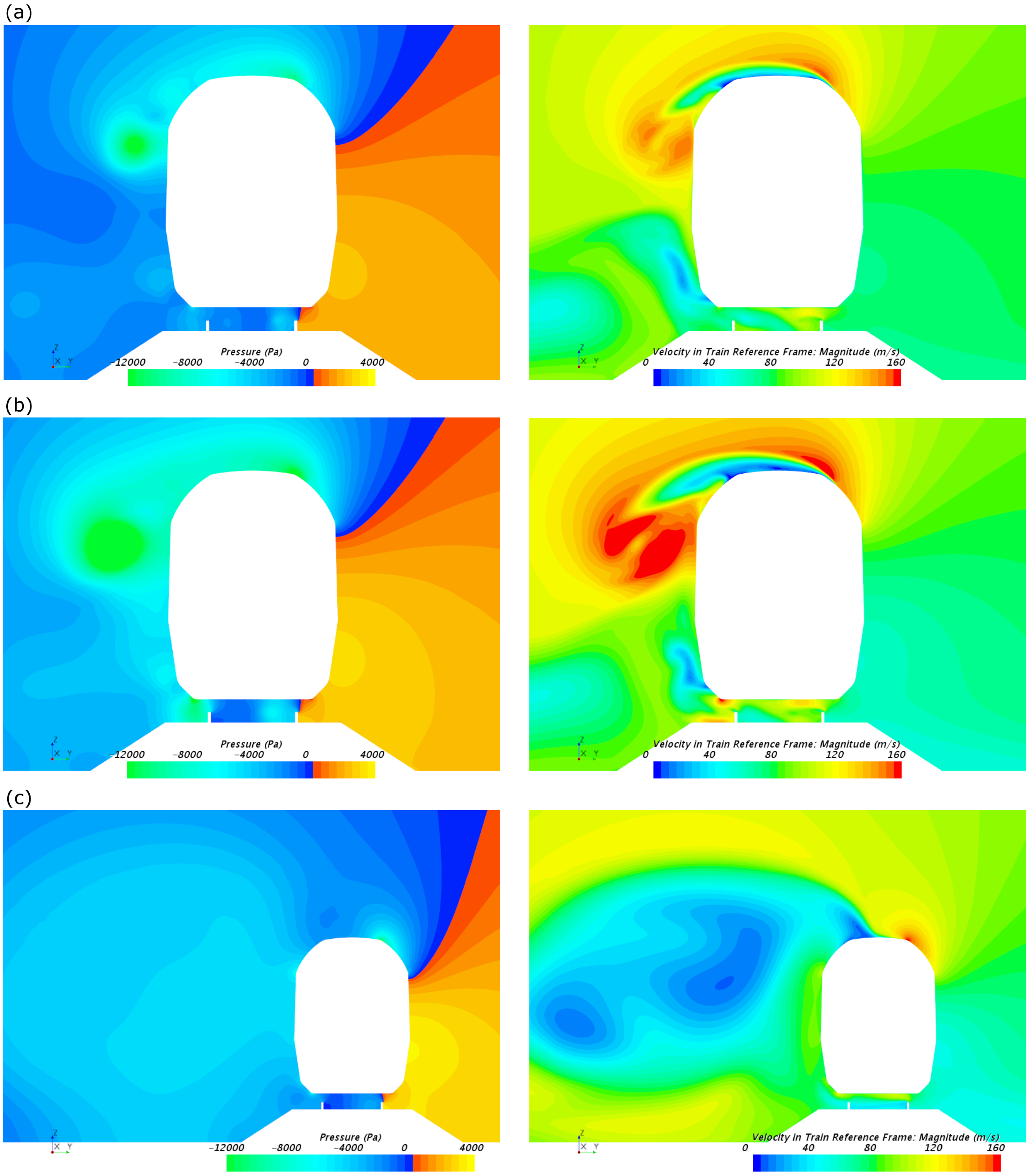

Figure 69 – Analysis of the pressure and velocity fields, evaluated at *Plane I*, for Mesh V, Domain E' for different yaw angles. The influence of the inlets and outlets in the flow is presented. Results obtained with the SST turbulence model. (a) 35°, (b) 45°, (c) 55°.

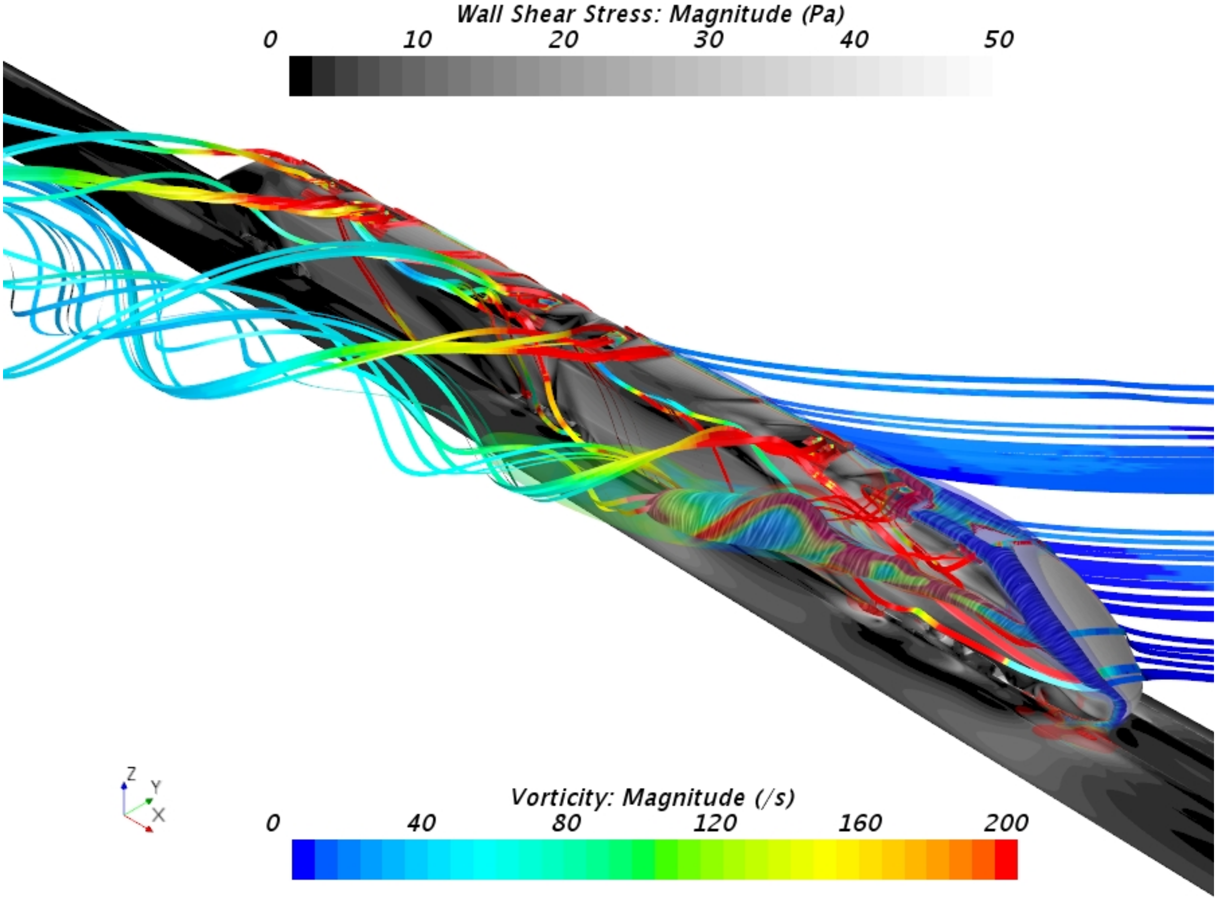

Figure 70 – Visualization of the wake behavior and the streamlines from the exhaust outlets and to the air-intake inlets. Vorticity colored streamlines and iso-surfaces for pressure coefficients $c_p = -1.5$ (transparent) and $c_p = -2.0$ (opaque). Analysis at yaw angle $\beta = 45°$.